HIGH-RESOLUTION CHEMOSTRATIGRAPHY OF THE MANCOS SHALE

Mapping the chemostratigraphy of the Upper Cretaceous Mancos Shale, New Mexico, USA, using high-resolution XRF core scanning techniques.

By Jeremy J. Gabriel B.Sc.(Hons), M.Sc

A Thesis Submitted to the School of Graduate Studies in Partial Fulfilment of the Requirements for the Degree of Doctor of Philosophy

McMaster University DOCTOR OF PHILOSOPHY (2022) Hamilton, Ontario

(Earth Sciences)

TITLE: Mapping the chemostratigraphy of the Upper Cretaceous Mancos Shale, New Mexico, USA, using high-resolution XRF core scanning techniques.

AUTHOR: Jeremy J. Gabriel

SUPERVISOR: Dr. Eduard G. Reinhardt

NUMBER OF PAGES: xx, 146

Lay Abstract

Elemental data were collected at high-resolution sampling (0.5 mm) from sedimentary rock core to determine environmental changes and shoreline trajectories during the Upper Cretaceous. Chemofacies, which group the intervals based on their elemental signature, were developed using a statistical clustering algorithm to investigate the character and variability of several depositional environments with respect to their proximity to shoreline and relative water depth. Chemostratigraphy, which maps the elemental variations through the core, was used to show shoreline advance and retreat due to relative changes in sea level, which could be correlated with previous studies. This is the first time in which these high-resolution shoreline trajectories could be established in marine mudstones that are typically visually homogeneous.

Abstract

High-resolution (500 μm) elemental data were collected from marine sedimentary rocks of the Upper Cretaceous Western Interior Seaway of North America using an Itrax μXRF core scanner in order to create detailed chemofacies and chemostratigraphic profiles to aid in the construction of sequence-stratigraphic frameworks in mudstone successions. Chemofacies were created for several depositional environments associated with siliciclastic shorelines such as fluvial channels, delta front, prodelta, mudbelt, and sediment-starved shelf using an unsupervised, hierarchical clustering algorithm known as a Self-Organising Map, which is topologically invariant so the clusters could be further grouped into superclusters to investigate variability within the depositional environments at a number of scales. Chemostratigraphic mapping was done on a 94-metre long section of Mancos Shale from a single well. The high-resolution data showed marine transgressive-regressive cycles at several orders that could be correlated to shoreline trajectories established in near-shore facies. Both the point of maximum regression, which indicates the initial flooding during a relative sea-level rise, and maximum transgression (i.e., the maximum flooding surface), could be accurately identified indicating that a complete cycle was recorded at each order. The data between the two represents a correlative conformity, which can provide palaeoenvironmental information that is not retained in near-shore facies. This research proves that marine mudstones retain a more complete record than near-shore sandstones and that they contain a wealth of palaeoenvironmental information. The high-resolution sampling of a μXRF core scanner is the only method that can fully map the chemostratigraphy of these mudstones, which are often visually homogeneous. By applying these techniques to other mudstone cores from the Western Interior Seaway or another Upper Cretaceous epeiric sea, high-resolution sequence-stratigraphic frameworks can be developed that can be used to reconstruct palaeoclimates at local to global scales.

Acknowledgements

First, I would like to thank my supervisor, Dr. Eduard Reinhardt, for his guidance and mentorship throughout my entire academic career. Dr. Reinhardt took a chance on me as an undergraduate student and brought me to Israel as a field assistant and since then I have literally travelled the world for both academic and professional purposes as a result of being his student. I am forever grateful for the experiences I have had with him and will hope to provide the same guidance to my own future students.

Next, I would like to thank Dr. Janok Bhattacharya, my pseudo co-supervisor, who also took a chance on me and gave me the opportunity to work with his Quantitative Sedimentology Lab on a new technique for analysing the ancient sediments that his lab studies. He always made himself available for meetings when I had questions about the new concepts I was learning and looking back on it, I should have spent even more time having meetings and discussions with him. I am sure I will go back to him many times throughout my future career to ask for his help and opinions.

I would also like to thank Dr. Antonio Paez for providing invaluable assistance with my R code and the clustering algorithm that proved to be a major component of my data analysis. I'm not sure I would have been able to produce the interpretations that I did without this analysis and I will certainly continue to develop this technique in my future research.

To my friends and colleagues at McMaster, particularly Nick Riddick, Sean Leipe, and Sian Ford, I could not have made it through this without your conversation, laughter, and support during all the ups and downs of grad school.

Finally, my family. There are no words to express how fortunate I consider myself to have the kind of never-ending love and support that you have all given me through the roller coaster ride which has been my life since I started down this path in geology.

This work was generously funded by an NSERC CRD Grant (CRDPJ-499420-2016) to JP Bhattacharya, jointly sponsored by BP and by the Susan Cunningham Research Chair in Geology at McMaster University, and through an Ontario Graduate Scholarship to JJ Gabriel.

Contents

List of Figures

List of Tables

Declaration of Academic Achievement

The research design of this thesis was developed by me, Jeremy Gabriel, with the assistance of my supervisor, Dr. Eduard Reinhardt, and committee member, Dr. Janok Bhattacharya. I conducted all of the data collection and analysis for the rock core from the Itrax μXRF core scanner here at the McMaster University Core Scanning facility. In addition to Drs Reinhardt and Bhattacharya, I also received assistance from Dr. Antonio Paez with respect to the statistical analysis and clustering to develop the chemofacies. Finally, I used data collected by Xueke Chang, who described the lithology of the sample used in Chapter 2 as part of an undergraduate thesis under the supervision of Dr. Bhattacharya, Cristina Genovese, who described the lithology of the Mancos core as part of a M.Sc. thesis under the supervision of Dr. Bhattacharya, and Majed Turkistani, who prepared and analysed the samples from the Caineville outcrop and produced the stratigraphic log in Chapter 3 as part of a Ph.D. thesis under the supervision of Dr. Reinhardt.

All the writing, figures, and tables in this thesis were produced by me, with edits and comments provided by Drs Reinhardt, Bhattacharya, and Paez.

Chapter 1.

Introduction

Epicontinental, or epeiric, seas have frequently occupied extensive areas of the continents during periods of sea-level highstand and a large portion of sedimentary research has been conducted on their associated deposits (Algeo et al., 2004; Bhattacharya and Tye, 2004; Algeo et al., 2007; Macquaker et al., 2010; Olde et al., 2015; Baioumy and Lehmann, 2017; Beil et al., 2018; Lin et al., 2019). The relative flatness and shallow depths (likely < 200 m) of these seas resulted in the deposition of thin, but laterally extensive, sedimentary sequences that can be correlated over areas at least an order of magnitude greater than modern continental shelf deposits (1000s of km compared to several 10s to 100s; Schieber, 2016). Furthermore, since these sea-level highstands are associated with 'greenhouse' periods, the sedimentary deposits can provide valuable information about how the climate system operates during such conditions, thus providing a better understanding of the impact of modern climate change. In addition to providing a valuable climate record, the sediments of these epeiric seas often host vast hydrocarbon reservoirs and so their study is of economic importance as well. During the Upper Cretaceous, much of North America was flooded by the Western Interior Seaway (WIS), a 3000-km long, 1500-km wide epeiric sea, which connected the Boreal Ocean in the north (proto-Arctic Ocean) to the Tethys

Ocean (proto-Atlantic/Gulf of Mexico) in the south (Miall et al., 2008, ; Figure 1.1). The WIS occupied a retroarc foreland basin that formed as a result of crustal flexure and loading from the subduction of the ancient Farallon Plate beneath the western margin of the North American Plate. Sediments eroded from the uplifting Sevier Orogenic Belt were fluvially transported to the western shore of the WIS where the coarser sand fraction was deposited in a series of deltaic complexes, such as the Ferron, Gallup, and Point Lookout systems, while the finer-grained silt and clay fraction was deposited deeper in the basin as a wide mudbelt spanning storm-weather wave base (SWB). Further orogenic activity during the Laramide event (late Upper Cretaceous – early Palaeogene) divided the WIS into a series of sub-basins (e.g., Uinta, Piceance, and San Juan), which helped to preserve the marine strata.

Figure 1.1: A reconstruction of the Western Interior Seaway during the mid-Coniacian (from Colorado Plateau Geosystems; www.deeptimemaps.com)

Sequence Stratigraphy

Basin reconstructions are generally done using sequence stratigraphy, which groups near-shore and distal sediments into a 'conformable succession' known as a sequence that is bounded on top and bottom by regional unconformities (van Wagoner et al., 1990; Bhattacharya, 2011). The earliest sequences established for the North American interior were continental in scale, 100s of metres thick, and were bounded by unconformities that could be mapped over 1000s of kilometres (Sloss, 1963). However, within these large sequences, which are now generally considered to be 'supersequences' (Catuneanu, 2019), less extensive unconformities were often present indicating that these sequences were built of higher-order cycles. The development of seismic-stratigraphic techniques in the late 1970s was able to significantly divide the original Sloss (1963) supersequences into smaller sequences and led to the concept of eustasy being the driving force in the formation of sequences (Vail et al., 1977). Further research using higher-resolution techniques such as well-logs and bed-scale lithologic mapping of core and outcrops led to the division of these sequences into smaller stratal units such as systems tracts and parasequences that were bounded by chronostratigraphically-significant marine flooding surfaces (van Wagoner et al., 1990). Recently, bed- to lamina-scale lithologic studies on well-preserved outcrops of the WIS have created detailed sequence-stratigraphic frameworks that demonstrate shoreline trajectory changes at metre-scale occurring at Milankovitch frequencies (100 ka, 46 ka, 20 ka; Zhu et al., 2012; Lin et al., 2019). At each scale, all the way down to local sedimentologic cycles operating over decades or centuries at sub-metre to centimetre-scale, the 'conformable succession' can be divided into a series of higher-order depositional cycles representing higher-frequency, and perhaps more localised, sea-level fluctuations (Catuneanu, 2019). The upper limit on the order is controlled by the sampling resolution and the sedimentation rate. While these higher-resolution lithologic analyses of outcrop work well in sandier facies, the high weathering potential of mudstone facies, those with grain size less than 63 μm, causes them to be poorly preserved and exposed in outcrop and thus they are comparatively understudied in the literature (Dypvik and Harris, 2001; Schieber et al., 2007; Bhattacharya and MacEachern, 2009; Taylor and Macquaker, 2014). However, fine-grained sediments and rocks (mudstone) comprise roughly two-thirds of the global sedimentary record (Boggs Jr. and Boggs, 2009; Macquaker et al., 2010; Lazar et al., 2015) and successions of these rocks often contain a more complete record than their coarser-grained counterparts, which are subject to significant periods of erosion or non-deposition (Bhattacharya et al., 2019). Furthermore, recent research of clay-sized sediment in flume experiments (e.g., Schieber et al., 2007, 2013) has shown these grains to be susceptible to flocculation at certain suspended-sediment concentrations and energy regimes, settling out of the water column in a wide range of environments and thus can provide valuable information regarding palaeoclimates, water energy and chemistry conditions, and sediment provenance (Pietras and Spiegel, 2018). Therefore, including them in sequence-stratigraphic frameworks is crucial to fully reconstructing the evolution of a basin.

The sequence stratigraphy of mudstones has been difficult to establish for several reasons. In addition to the poor preservation potential in outcrop (as mentioned above), the subtle textural and structural changes in even coarser-grained mudstones (medium to coarse silt; 15-63 μm) make them difficult to characterise with traditional techniques. Well-log data that measure the natural gamma radioactivity (NGR), which is a function of the presence of elements such as K and Th that are generally enriched in fine-grained sediments, and the deep and shallow resistivity of the sediments, which is mainly a function of grain size but can also be impacted by diagenetic alteration such as carbonate cementation, are the most common since they do not require the collection of physical material (i.e., cores). However, the limited number of proxies and lower-resolution sampling (0.5-1 m) make distinguishing mudstones or accurately identifying key surfaces difficult, which can lead to ambiguous correlations between boreholes (Pearce et al., 1999; Turner et al., 2016). This has led to the development of basin cross sections with large, mainly undifferentiated mudstone successions that span millions of years (e.g., Nummedal and Molenaar, 1995; Molenaar et al., 2001; Ridgley et al., 2013). Even where rock core has been collected, lithologic analysis of these sediments is difficult to do at a macroscale and often require petrographic thin sections, X-ray diffraction analysis, or even electron microscopy to accurate log them (Boggs Jr. and Boggs, 2009; Plint, 2014; Taylor and Macquaker, 2014; Birgenheier et al., 2017; Yoon et al., 2019).

Mudstone Chemostratigraphy and Chemofacies

Despite the apparent visual and physical homogeneity, several studies have demonstrated that there is a significant level of variability in elemental abundances through these muddy successions (e.g., Algeo et al., 2004; Lash and Blood, 2014; Olde et al., 2015; El-Attar and Pranter, 2016; Beil et al., 2018; Profe et al., 2018). Chemostratigraphy, which maps the downcore variations of elemental concentrations in sedimentary rock, can greatly enhance the interpretation of depositional environments due to the number of proxies that are available, which is on the order of dozens to hundreds when elements and ratios (e.g., Zr/Rb, Sr/Ca, Ca/Ti) are used (Craigie, 2018). Traditional methods for analysing elemental concentrations, such as inductively-coupled plasma optic emission spectrometry (ICP-OES) or mass spectrometry (ICP-MS), are able to provide highly accurate data, down to the ppm or ppb for some major elements, however they require the collection and pre-treatment (e.g., digestion or fusion) of subsamples with enough material (milligrams to grams) to be properly analysed. In fine-grained sediments with lower sedimentation rates, each subsample may homogenise several millimetre-scale laminae that were each deposited in separate events, thus aliasing the palaeoclimate signal. When combined with the lower overall sampling resolution, on the order of one sample per 0.5-1 metre (Craigie, 2018), these traditional methods lack the spatial resolution to detect significant higher-frequency fluctuations. For example, Olde et al. (2015) examined a 405-m core of hemipelagic sediments from the Upper Cretaceous Bohemian Basin (Czech Republic) and were able to identify major marine trangressions at 0.4-1 Ma cycles but the lower sampling resolution (2-m intervals equating to ~22 ka) means that higher-order cycles at 100 ka frequency or less are not reliably detectable and therefore correlating them with high-resolution sequence-stratigraphic frameworks of proximal environments (e.g., Zhu et al., 2012; Lin et al., 2019) is difficult.

Recent advances in core scanners using energy-dispersive X-ray fluorescence (ED-

XRF), herein referred to as μXRF, has allowed for the collection of ultra high-resolution elemental intensity data at sampling intervals as low as 100μm. These scanners, such as the Itrax Core Scanner (Cox Systems, Mölndal, Sweden), can analyse entire split sediment and sedimentary rock cores with minimal preparation (i.e., no subsampling or pre-treatments) in a single automated run, which can be completed at a fraction of the cost and time of traditional techniques. The core, up to 1.8 metres long, is placed onto a stage that moves at set increments past an X-ray generator (Figure 1.2), exposing the core to high-energy (up to 3kW) X-rays that cause the excitation and ejection of inner-shell electrons from the elements that are present. As outer-shell electrons drop

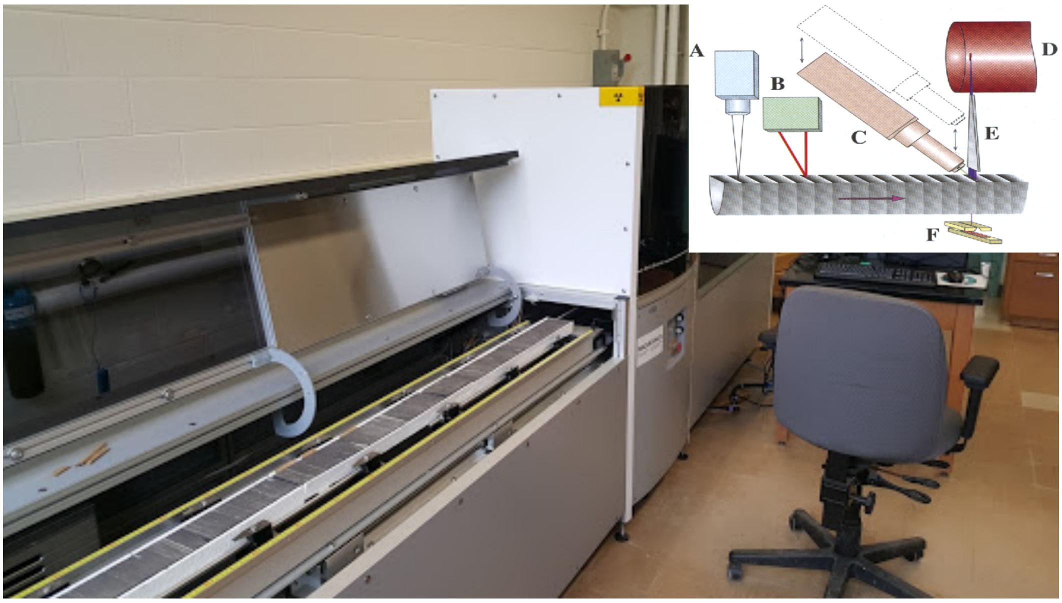

Figure 1.2: The Itrax μXRF core scanner with core loaded on the stage. The core is moved incrementally through the housing containing the (A) optical camera, (B) laser triangulation, (C) XRF detector, (D) 3kW X-ray generator, (E) X-ray waveguide, and (F) radiograph camera.

to fill in the space, they emit a photon with a characteristic energy that is counted by the X-ray detector; raw Itrax data are presented as total counts (cts) of a photon at a distinct energy level.

The raw data are calibrated against the X-ray detector settings and a suite of elements to convert them into elemental intensities, also presented in cts, providing meaningful abundance data on elements between aluminium (Al; Z=13) to uranium (U; Z=92). In addition to the vertical sampling interval, the user can also change the X-ray energy and the duration of exposure that the sample is subjected to so the total counts are not only a function of the abundance of each element, but also the time of exposure; heavier elements will have better detection with higher-energy X-rays and longer exposure times. The elemental intensity data do not have the same level of accuracy as ICP-OES/MS (i.e., ppm or ppb) but previous research by Weltje et al. (2015), Gregory et al. (2019), and Cerdà-Domènech et al. (2020), proves that the data have exceptional precision (reproducibility) over multiple scans (see subsection 2.3.1) and show moderate to strong correlations to absolute concentrations obtained with ICP-OES/MS, particularly when the down-core trends are compared (see subsection 2.3.3). In addition to elemental data, the Itrax obtains an optical image (RGB) and X-radiograph (greyscale density) allowing the elemental data to be directly compared to the core image. Colour data such as luminosity (L*), redness (a*), and yellowness (b*) have been used by previous researchers to establish limestone-marlstone couplets that are the result of Milankovitch cyclicity (Li et al., 2019; Ma and Li, 2020), so these additional colour data obtained from the Itrax may be useful for establishing astrochronological cycles.

While studies conducted using ED-XRF elemental data originally focused on unconsolidated marine and lacustrine sediment cores (see Croudace et al., 2006 and Croudace and Rothwell, 2015 for comprehensive reviews), more studies are focusing on sedimentary rock successions, particularly mudstone (e.g., Rowe et al., 2012; Ma et al., 2014; Turner et al., 2016; Birgenheier et al., 2017; Beil et al., 2018; Pietras and Spiegel, 2018). Beil et al. (2018) conducted a 1-cm resolution study on a continuous 325-metre long core of Cretaceous (Albian-Turonian) pelagic mudstone using an ED-XRF core scanner to identify transgressive surfaces based on terrigenous input, grain size, clay composition, and bottom-water oxygenation. The transgressive surface, which is commonly coarser-grained due to winnowing, was characterised by a peak in the Zr/Rb log-ratio (grain-size) and an associated low in the log-ratio of terrestrial, which they represented with the sum of the siliciclastic elements Al, Fe, K, Si, and Ti, to marine, Ca, indicators. They also showed a correlation between weathering intensity, indicated by the log-ratio of K/Al, and bottom-water oxygenation, indicated by the log-ratio of Mn/S. During periods of decreased weathering (i.e., drier; high K/Al) there was increased oxygen depletion (low Mn/S) as a result of lower energy and mixing at the sediment-water interface (Beil et al., 2018). Turner et al. (2016) also established systems tracts based on 'chemostratigraphic flooding surfaces' in ED-XRF data, using a portable handheld unit directly on an exposed outcrop. Retrogradational and progradational successions were defined by upward decreasing and increasing values in terrigenous elements, respectively, and the chemostratigraphic flooding surface was placed where the retrogradational trend switched to progradational (i.e., the maximum flooding surface).

Materials and Methods

This research focuses on the Mancos Shale, a muddy marine deposit that formed in the WIS during the Upper Cretaceous (Cenomanian - mid-Campanian). The early Upper Cretaceous (Cenomanian-late Turonian; 97-91 Ma) was by far the warmest period in the past 115 Ma, with tropical sea-surface temperatures estimated at $> 35°$C and even mid-latitude intermediate water temperatures as high as 20°C in the southern hemisphere (Friedrich et al., 2012). After 91 Ma, the opening of the Equatorial Atlantic Gateway (EAG) between Africa and South America increased longitudinal oceanic circulation allowing for colder polar waters to move into the proto-North Atlantic and global temperatures started to decrease, a trend that has continued to the present (Friedrich et al., 2012).

The first part of this research analyses a short (28.5 cm) section of the Blue Gate Member of the Mancos Shale collected from the Uinta Basin, Utah, by Schlumberger/TerraTek, though the exact location is not known for proprietary reasons (chapter 2). This highly interbedded (~240 laminae) section of mudstone to very-fine sandstone was deposited on a storm-wave-dominant shelf with fluvial input, as indicated by the presence of terrestrial organic macerals in petrographic thin section (Grigg, 2016). This section was first scanned multiple times at 0.2- and 0.5-mm sampling intervals (1426 and 571 observations, respectively) with an Itrax core scanner to determine the level of precision (reproducibility) of the data (subsection 2.3.1). Several subsequent analyses were conducted on this interval including lithology, whole rock geochemistry (ICP-OES/MS), and petrology that were compared against the μXRF elemental data to fully understand the relationship between the absolute elemental and mineral concentrations and the Itrax elemental intensities. Fifteen samples of ~0.2 g each were collected from individual lamina (2-3 mm wide) for ICP-OES/MS analysis and three large petrographic thin sections (5x7 cm) were made from the opposing face. The results from this analysis will guide the interpretation of the μXRF data collected from the second part of this research, where ICP-OES/MS and petrographic data were not obtainable.

The second part of this research uses a 94-metre long succession of Mancos Shale, in 5 continuous but separated intervals, which was collected from the San Juan Basin in Rio Arriba County, New Mexico by Schlumberger/ TerraTek (Well ID: San Juan 28-6 148M; 36.6425°N, -107.4506°W) and archived at the New Mexico Bureau of Geology and Mineral Resources in Socorro, New Mexico. The slabbed (archival) half of the core was loaned to McMaster University for non-destructive elemental analysis using an Itrax μXRF core scanner. The first goal with this succession will be to define the geochemical signature for distal depositional environments, such as the mudbelt and sediment-starved shelf, and establish their chemofacies by comparing them to the signature of sediments collected from outcrop in known proximal environments, such as fluvial, delta front, prodelta areas (chapter 3). The chemofacies will be established using a hierarchical clustering algorithm known as a Self-Organising Map (SOM), to define each sample interval according to its total elemental makeup. While the general geochemical makeup of sedimentary rocks from these environments has been described previously (e.g., Hart, 2016; Birgenheier et al., 2017), the volume of data collected from an Itrax core scanner will provide significantly more information regarding not only the variation in average values between environments but also the spread and variance of the data within each environment. These robust chemofacies will provide for more accurate, less ambiguous correlations of mudstones across a basin.

After establishing the chemofacies of the different depositional environments, the entire 94-metre succession will be analysed, providing a high-resolution chemostratigraphic *mapping* of the sediments. The entire section will be clustered using the SOM to establish the chemofacies and the chemostratigraphic trends of several elemental proxies will be analysed in order to identify marine transgressive-regressive (T-R) cycles at several orders. Depending on the order, these cycles can be correlated to near-shore frameworks in the San Juan Basin (5^{th}-order and above) as well as with lower-resolution chemostratigraphy studies using ICP-OES from other basins (4^{th}-order and below). This research will look to provide the first geochemical signature of depositional surfaces and cycles, such as the distal correlative conformity that is associated with near-shore unconformities. The correlative conformity is an important phase to identify as it records palaeoenvironmental information that may be lost in near-shore environments due to periods of non-deposition or erosion. This research will also look to provide the first example of sub-Milankovitch cyclicity in fine-grained muddy successions. Overall, these results will be crucial to incorporating mudstones into high-resolution sequence-stratigraphic frameworks, which will allow for a better understanding of how the climate operates in a greenhouse world.

As this work has been completed as a 'sandwich' thesis, each Chapter aside from the Introduction and Conclusion has been prepared as a stand-alone study for publication in a peer-reviewed journal. Therefore, there is some overlap in the information presented in each Chapter that pertains to background geology and methodology. However, each Chapter presents new independent results and discussions and Chapters 3 and 4 build upon the knowledge gained from the previous chapter(s). All three chapters have multiple authors who assisted in data collection or editing in some way but the main body of work, including all writing, figures, and tables, was produced by myself, Jeremy Gabriel.

Chapter 2.

Application of μXRF analysis on the Upper Cretaceous Mancos Shale: A comparison with ICP-OES/MS

This chapter was published in Marine and Petroleum Geology as Gabriel JJ, Reinhardt EG, Chang X, Bhattacharya JP (2022). Application of μXRF analysis on the Upper Cretaceous Mancos Shale: A comparison with ICP-OES/MS. Marine and Petroleum Geology 140, https://doi.org/10.1016/j.marpetgeo.2022.105662

2.1 Introduction

Fine-grained siliciclastic rocks (< 63 μm) comprise approximately half to two-thirds of the global sedimentary record (Boggs Jr. and Boggs, 2009; Dypvik and Harris, 2001) and although traditionally they have been viewed as indicating deposition from suspension settling in low-energy environments, recent research (e.g., Bhattacharya and MacEachern, 2009; Plint et al., 2012; Plint, 2014; Schieber, 2016; Macquaker et al., 2010; Wilson and Schieber, 2014) has shown that mud can also be deposited in hemipelagic environments that are subject to significant wave, tidal, and bottom-current energy, and thus often contain similar bedforms to those found in shallower environments (e.g., ripples, cross-lamination, grading). However, the textural and lithological changes in these sediments can be subtle and may not be visible in slabbed rock core without petrographic analysis, making the study of mudstones significantly more complex than sandstones (Dypvik and Harris, 2001).

Chemostratigraphy of fine-grained rock and sediment cores based on elemental and isotopic composition has been used to effectively show changes in precipitation patterns (e.g., Zarriess and Mackensen, 2010; Haug et al., 2003), provenance and sediment transport processes (e.g., Ben-Awuah et al., 2017; Chen et al., 2013), and bottom-water redox conditions (e.g., Baioumy and Lehmann, 2017; Algeo and Rowe, 2012) in both modern and ancient systems; a search of the literature showed over 1500 publications relating to chemostratigraphy or chemofacies since 2000 (Web of Science, Clarivate Analytics). Two common techniques for elemental and isotopic analysis are inductively-coupled plasma optical emission spectrometry/mass spectrometry (ICP-OES/MS), and wavelength-dispersive X-ray fluorescence (WD-XRF), which can detect 55 and 42 elements, respectively, with an analytical precision as low as parts per million or billion (ppm/ppb). This provides at least 42 highly accurate variables for use in chemostratigraphic correlations and when elemental ratios (e.g., Ti/Al, Zr/Rb, Ca/Fe) are used, the number of variables can exceed 250 (Craigie, 2018). However, these methods are destructive and can be very intensive in terms of time (subsampling, sample preparation, pre-treatment) and cost, so down-core sampling resolution is often on the order of 1 sample per metre. Subsamples are collected, ground, and homogenised into roughly 1-2g of fine (< 10 μm) powder, which is then liquefied, for ICP-OES/MS analysis (Craigie, 2018), or fused and pressed into a lithium-borate pellet, for WD-XRF analysis (Gregory et al., 2019; Weltje and Tjallingii, 2008). The pre-treatment method chosen (e.g., acid digestion, alkali fusion) can result in different detection limits and accuracy of certain elements so the desired variables should be considered prior to analysis. One centimetre sampling and analysis of a metre-long core could take a couple weeks (Croudace et al., 2006) and cost thousands of dollars, and since the methods are destructive, replicate analyses would require the collection of more material, which may have a different elemental composition due to vertical and lateral heterogeneities.

Recently (~20 years), technological advancement of core scanners using energy-dispersive XRF (ED-XRF), such as the Itrax Core Scanner (Cox Systems, Sweden), has allowed for a much higher sampling resolution (100 μm) from marine and lacustrine sediment cores (Löwemark et al., 2019; Rothwell and Croudace, 2015a; Rothwell and Rack, 2006); herein, this method is referred to as μXRF. These core scanners allow for rapid and non-destructive analysis of elemental composition from Al (Z=13) to U (Z=92) by recording the spectrum of energy intensities, in keV, from emitted photons. Energy-dispersive XRF does not have the elemental precision of WD-XRF but it can rapidly collect data on more variables simultaneously than WD-XRF, which requires a diffraction crystal that is tuned to permit transmission of a specific wavelength (element) of interest. The core requires minimal preparation, aside from ensuring a flat, even surface and there are no pre-treatments necessary since the sample or split core is placed into the core scanner whole for analysis (Löwemark et al., 2019). The Itrax is equipped with a 3 kW X-ray generating tube, typically of either Cr or Mo, and can be operated up to 60 kV and 50 mA, although 30 kV and 30 mA is suitable for detecting most elements (Croudace et al., 2006); other user-defined options include measurement interval and exposure time (from 1 sec to 1 min). Split cores up to 1.8 m in length can be analysed in a single, automated scan, which could be completed in less than 2 hours (1.8 m at 1 cm interval and 30 second exposure time) and provide hundreds to thousands of sampling intervals. As the data acquired by μXRF core scanners are in total counts of emitted photons, the final result will not only be a function of the presence and abundance of the various elements within the core, but also a function of the exposure time and power of the incident beam. Furthermore, since a discrete sample is not homogenised prior to analysis, the interval can be heterogeneous in terms of grain size, pore space, organic matter, and water content (so-called *matrix effects*; Tjallingii et al., 2007; Croudace et al., 2006). These matrix effects can lead to increased scattering, which can influence the final spectra, with the effects being more pronounced with lighter elements that eject lower energy photons (Tjallingii et al., 2007). However, several studies have shown that calibration of elemental intensities obtained from ED-XRF to absolute concentrations is possible through statistical analysis and comparison to values obtained using ICP-OES/MS and WD-XRF (e.g., Arenas-Islas et al., 2019; Gregory et al., 2019; Al Maliki et al., 2017; Rowe et al., 2012; Weltje et al., 2015; Weltje and Tjallingii, 2008). Weltje et al. (2015) showed that the most accurate method was a multivariate log-ratio calibration (MLC), in which the ratios of elemental intensities measured from μXRF are compared with concentrations measured using ICP-OES/MS. While this method provides more accurate estimates of absolute element concentrations from their measured intensities, it does increase time and cost of the analysis (Gregory et al., 2019). A univariate log-ratio calibration (ULC), which relates "relative" element concentration (W) to the elemental intensity (I), does not require calibration against data from other methods and can be used to adequately describe the system through the linear relationship:

$$ln\left(\frac{W_{ij}}{W_{iD}}\right) = \alpha_{jD} ln\left(\frac{I_{ij}}{I_{iD}}\right) + \beta_{jD} \tag{2.1}$$

where j and D represent the two different elements being measured at interval i and α_{jD} and β_{jD} account for the matrix effect and detection efficiency, respectively. It is considered a relative concentration since all the elements measured are constrained to unity, despite the fact that not every element (i.e $Z < 13$ and $Z > 92$) can be detected. Gregory et al. (2019) found that normalizing elements to the X-ray scatter ratio (incoherent:coherent) produced statistically significant results and this divisor is often used in palaeoenvironmental studies to account for water content (e.g., Boyle et al., 2015) and organic matter (e.g., Brown et al., 2007).

Micro-XRF core scanners have been used extensively in research on soft sediment cores (see Croudace and Rothwell, 2015 Rothwell, 2006 for a comprehensive review) but more recently they have also been applied to coal seams (Ward et al., 2018; Kelloway et al., 2014), speleothems (Scroxton et al., 2018), tephras (Peti et al., 2019), and glass samples (Ernst et al., 2014). Their use on rock cores, however, is lacking (e.g., Beil et al., 2018; Ma et al., 2014). Micro-XRF is an optimal method for chemofacies analysis of rock cores because the cut surface of the core is smooth and flat and the matrix effects are minimised, especially with fine-grained rocks like siltstone and shale.

This study focuses on a short section (28.5 cm; herein referred to as the 'Cheese Slab') of the Blue Gate Formation of the Mancos Shale, a muddy shelf deposit from the Upper Cretaceous Western Interior Seaway of North America. The Cheese Slab was collected from a proprietary quarry in the Uinta Basin, Utah, by TerraTek/Schlumberger and provided to McMaster University by the New Mexico Institute of Mining and Technology. The goal of this study is to examine trends in the μXRF-derived elemental intensities and how they correspond to the mineral and elemental composition based on petrographic and ICP-OES/MS analysis, respectively. The μXRF data will also be compared to the macro- and microscale lithology to demonstrate how it can be used to identify and refine lithofacies for eventual application to longer successions of Mancos Shale. Finally, this study will demonstrate the potential of μXRF-derived chemofacies to identify characteristics such as provenance (marine vs. terrestrial), flooding surfaces, and geomechanical properties that are important to the exploration and extraction of hydrocarbons.

2.1.1 Geologic Background

The Mancos Shale was deposited into the Western Interior Seaway (WIS) of North America, which covered the central part of the continent during the Upper Cretaceous (Cenomanian - mid-Campanian; Figure 2.1). Subduction of the ancient Farallon Plate during westward migration of the North American tectonic plate caused building and uplift of the Sevier orogeny on the western margin of the North American plate resulting in the formation of an asymmetric foreland basin (Armstrong, 1968; Lowery et al., 2018; El-Attar and Pranter, 2016; Miall et al., 2008). Several marine transgressions occurred in the WIS throughout the Cretaceous, but a transgression during the Cenomanian and Turonian brought sea level to almost 300 m higher than present (Haq and Huber, 2017; Miall et al., 2008; McDonough and Cross, 1991). At this time, the WIS spanned it's maximum extent, connecting the northern Boreal (Arctic) Ocean with the southern Tethys (Gulf of Mexico). During this highstand several deltaic complexes, such as the Ferron, Frontier, and Gallup, were deposited into the WIS, as sediments were eroded from the nearby Sevier orogenic belt and transported eastward (Armstrong, 1968; Lin et al., 2019; Bhattacharya and MacEachern, 2009), and the Mancos Shale represents the distal extent of those complexes. During the Laramide orogeny of the late Upper Cretaceous and early Palaeogene, the WIS was segmented into several sub-basins such as the Uinta (Utah), Piceance (central-western Colorado), and the San Juan and Zuni (north-western New Mexico), which preserved the Upper Cretaceous marine sequences (Hawkins et al., 2016; Broadhead, 2015; Ridgley et al., 2013). Due to the exceptional outcrop exposure and preservation, these fluvio-deltaic complexes have been extensively studied in terms of their facies architecture and sequence stratigraphy (e.g., Lin et al., 2019; Li and Schieber, 2018; Eldrett et al., 2015; Wu et al., 2015; Ahmed et al., 2014;

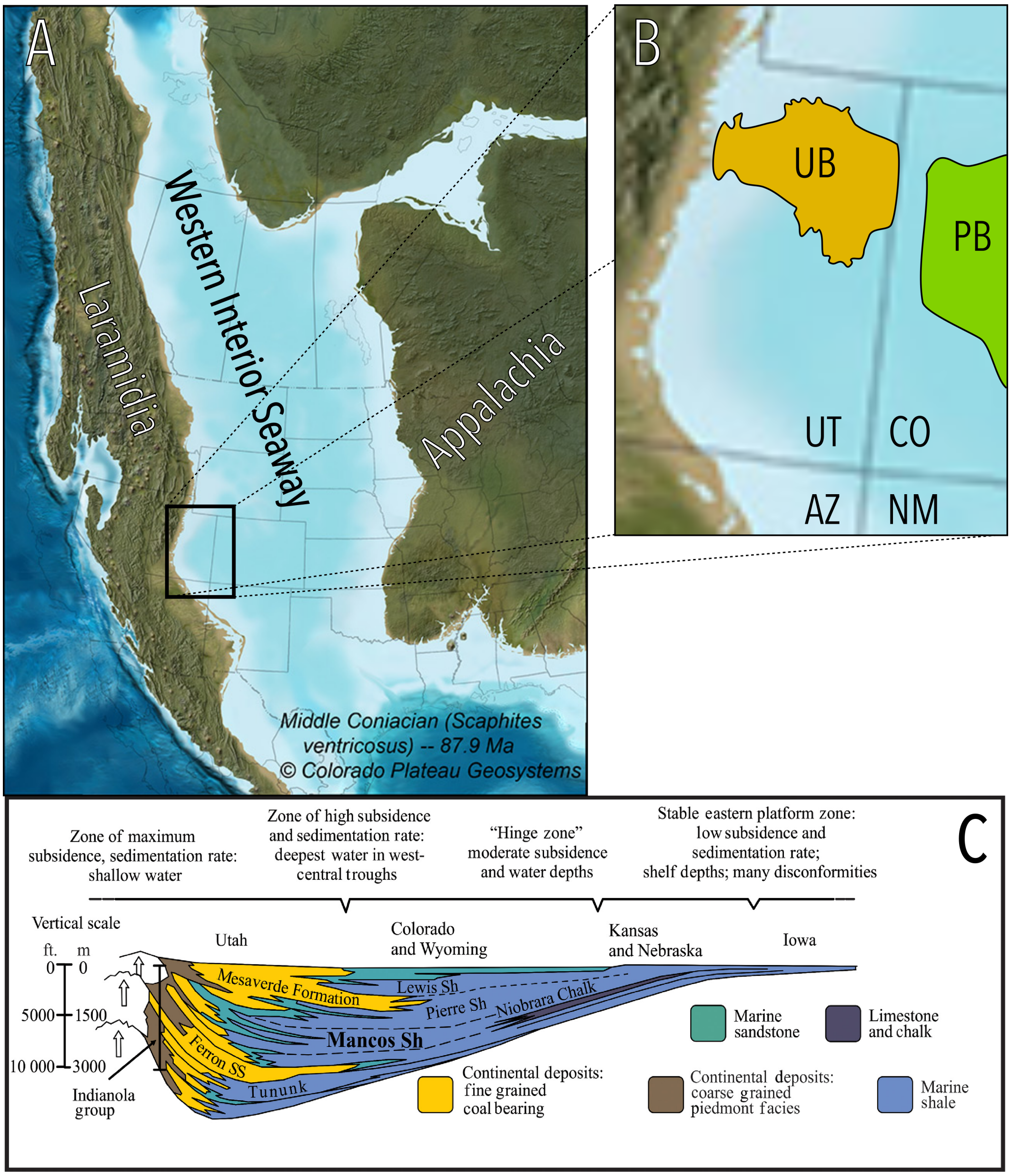

Figure 2.1: A) Reconstruction of North America during the Upper Cretaceous (mid-Coniacian, ~87.9 Ma; basemap from Colorado Plateau Geosystems www.deeptimemaps.com). B) Close up of the Uinta Basin (UB, location from Birgenheier et al., 2017) and Piceance Basin (PB, location from Hawkins et al., 2016); the two basins are separated by the Douglas Arch. C) Generalized west-east transect of the Uinta basin from Birgenheier et al. (2017) (originally in Armstrong, 1968).

Li and Bhattacharya, 2013; Zhu et al., 2012) with other studies looking into isotope chemostratigraphy (e.g., Joo and Sageman, 2014), microfossil assemblages (e.g., Turkistani et al., 2022; Lowery et al., 2018) and palynology (e.g., Akyuz et al., 2016). The combined results of these studies indicate that the early-mid Upper Cretaceous climate of the southern WIS was an ever-wet, sub-tropical to tropical environment.

In the Uinta basin, the Mancos Shale is over 1200 m thick with a high detrital quartz and clay content relative to carbonate sediment (Birgenheier et al., 2017). It is separated into two members that span the mid-Turonian to late-Campanian (∼92-79 Ma): the lower Tununk shale, which unconformably overlies the paralic Dakota Formation, and the upper, more extensive Blue Gate shale; the two units are separated by an organic-rich heterolith called the Juana Lopez Member (Molenaar and Cobban, 1991). Fine-grained sediment deposition in more distal marine environments (distal prodelta and mudbelt) has been a common focus of research in recent years (e.g., Bhattacharya and MacEachern, 2009; Plint et al., 2012; Plint, 2014; Schieber, 2016; Macquaker et al., 2010; Wilson and Schieber, 2014), as mudstones typically contain a more continuous record than near-shore deposits, which are more prone to periods of erosion and gaps in deposition (Bhattacharya et al., 2019). Birgenheier et al. (2017) developed a detailed record of the lower Blue Gate member based on lithology, stratigraphy and geochemistry, obtained using a handheld ED-XRF unit at 0.3-0.9 m intervals. They characterised ten facies based on grain size, mineralogic composition, and sedimentary structures, such as lamination and ripple style, that were deposited in three different marine settings: prodelta, mudbelt, and sediment-starved shelf (Figure 2.2). The prodelta, which is closest to the shoreline, contains interlaminated siltstone to very fine sandstone, with a medium to high detrital quartz content, and is dominated by river-fed hyperpycnal flow. The hyperpycnites observed were characterised by normal grading and basal scour (i.e. asymmetrical), with evidence of dewatering due to a high rate of sediment input. Moving further into the basin, the mudbelt spans storm-wave base and was divided into six facies. The upper two facies were interpreted to have been deposited above storm-wave base, due to the very high detrital quartz content and intense reworking from storm waves and bioturbation. The other four facies of the mudbelt were deposited below storm-wave base and typically showed the distal expressions of wave-enhanced sediment gravity flows (WESGFs; Macquaker et al., 2010) that were initiated above storm-wave base but flowed downslope. These facies had increasing preservation of lamination and ripples, higher clay content (mainly illite and kaolinite), and low to moderate bioturbation (BI = 2–3), although in some areas it was higher (BI = 5) (Birgenheier et al., 2017). Finally, the sediment-starved shelf contained moderate to high clay and calcite content (values not seen in the other facies) and showed only faint laminations and low bioturbation levels due to suboxic conditions. This area was mainly influenced by shelfal currents in the proximal shelf and suspension settling more distally (Birgenheier et al., 2017).

Generally, the three processes responsible for moving and depositing muddy sediments across epicontinental seas are: river-fed *hypo*pycnal plumes; river-fed *hyper*pycnal flows; and submarine ignitive gravity flows, which can be aided by wave or bottom currents (Schieber, 2016). Hypopycnal plumes typically come from large, continent-scale rivers (e.g. Mississippi, Amazon), which do not often have the sediment concentration to become hyperpycnal, and can travel long distances (100s km) from the river mouth by longshore currents. Hyperpycnal flows are more commonly associated with small, 'dirty' rivers, which were common on the western shore of the WIS. These 'dirty' rivers were susceptible to periods of intense flooding and sediment overload that produced sufficiently dense plumes that would sink and move along the seabed. Typically, a hyperpycnite will display a symmetrical grain size profile, with a basal inversely-graded unit overlain by a normally-graded unit as a result of changing flow velocities as the flood waxes and wanes. However, erosion of sediments during maximum flow or subsequent wave and current reworking may lead to asymmetric deposits (Schieber, 2016). Hyperpycnal flows require bottom slopes of $> 0.7°$ to maintain autosuspension and are thus typically confined to within a few tens of kilometres of the river mouth, although the distance can be greater during periods of more intense fluvial weathering and mud generation (Bhattacharya and MacEachern, 2009). In more distal environments, bottom currents and wave action act together to suspend fine-grained sediments in a fluid mud, which can move down slopes with lower gradients ($\sim$0.03°) and tends to form normally graded thin beds with sharp, basal contacts. These deposits can be resuspended and moved several times and therefore can reach 100s km from the shoreline. All three of these mechanisms can produce a similar succession in the rock record, thus differentiating between them based on lithology and sedimentary structures can be difficult (Schieber, 2016).

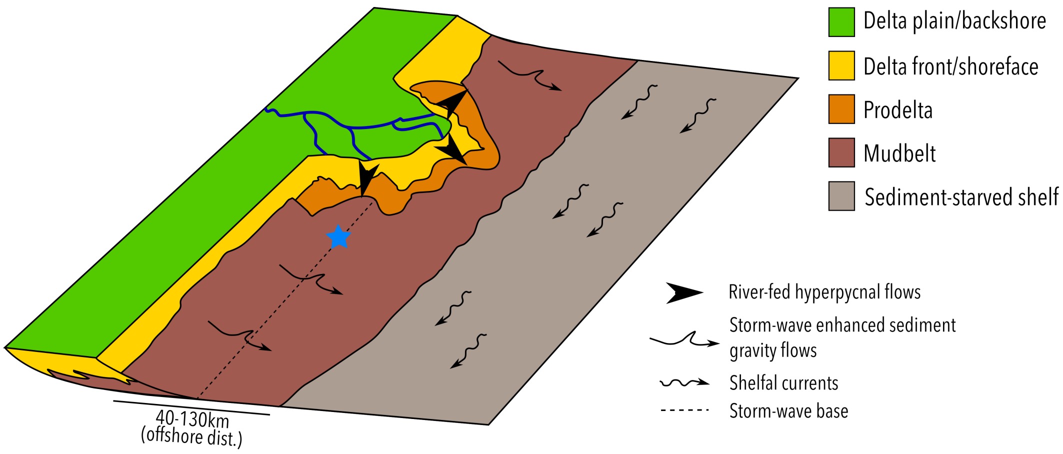

Figure 2.2: Depositional environments and their relationship to shoreline and deltaic tributaries. Adapted from Bhattacharya (2010). Blue star demarcates approximate core location (see subsection 2.3.4 and subsection 2.4.2).

2.2 Methods

The *Cheese Slab* is a highly interbedded very fine sandstone to mudstone sequence with approximately 240 individual laminae (Figure 2.3); grain sizes were estimated by microscope analysis of thin sections. Since accurate determination of grain size (i.e., silt vs. clay) in the darker, finer-grained lamina was not possible, herein we use the term *mudstone* to distinguish these from the lighter, coarser-grained sandstone laminae. A 6 cm wide and 2 cm thick piece was slabbed using a water-tile saw and adhered to a clear acrylic sheet using double-sided tape to allow for consistent positioning through the various analyses. Prior to being cut, the piece was vacuum-infused with an epoxy to prevent the fine-grained shale from being pulverized; this epoxy can be seen filling in the large fracture at ~130 mm. Lithofacies were established by millimetre-scale analysis of the laminae to measure characteristics such as lamina thickness, relative grain size, presence/preservation of sedimentary structures, and bioturbation.

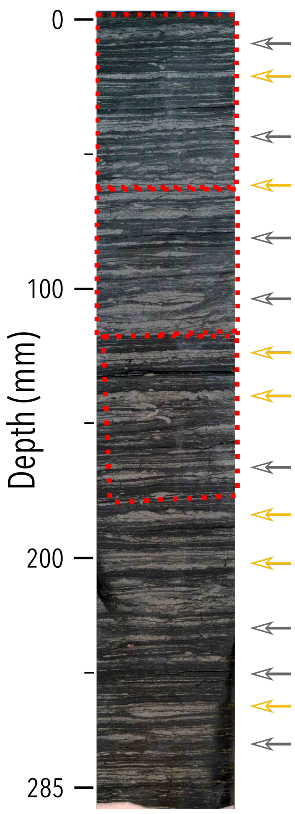

Figure 2.3: The core section showing location of thin sections (dotted red boxes) and ICP-OES/MS samples (grey arrows are from a mudstone interval, yellow from sandstone).

Three large-sized (5x7 cm) thin sections were made by Wagner Petrographic, Utah, USA from the opposing face of the scanned surface for petrographic analysis (A - top, B - middle, C - bottom). The samples were infused with a rose dye to accentuate microfractures and structures, ground to 25 μm, and polished (i.e. no slide cover). Each slide was digitally scanned with an Epson V850 Pro photo slide scanner (48-bit colour, 4800 dpi) in both plane-polarized (PPL) and cross-polarized (XPL) light to see the overall sedimentary structures and then analysed with a Leica petrographic microscope to determine the mineral composition. The remaining material from the thin section production was also analysed with the Itrax (30 kV, 33 mA, 200 μm, 15 sec) to allow for precise alignment of the μXRF data to the structures and mineral

Table 2.1: Itrax run parameters

Run	Tube Parameters				
	kV	mA	Exposure time (sec)	Interval (mm)	Position
1-4	30	33	15	0.5	Centre
5	30	33	15	0.2	Right

content.

2.2.1 Itrax μXRF

Elemental intensities were obtained from five separate analytical runs using an Itrax μXRF Core Scanner (Cox Analytical Systems, Mölndal, Sweden) at the McMaster University Core Scanning Laboratory (MUCS-Lab): scans 1-4 were performed down the centre at 0.5 mm resolution, while scan 5 went down the right side at 0.2 mm resolution for comparison to the ICP-OES/MS data (Table 2.1). The X-ray beam is 8 mm long, perpendicular to the longitudinal axis, and 0.1 mm wide (0.8 mm^2; Kelloway et al., 2014), with a penetration depth on the order of 1 mm, though penetration may be even less in denser material like siltstone and shale. The raw energy spectra of each analytical scan were batch evaluated in QSpec software (Cox Analytics) and an additional calibration was performed on scan 5 using the Cody Shale (USGS rock standard Sco-1), which is an Upper Cretaceous formation from the Powder River Basin, Wyoming, USA (Hubert et al., 1972). This calibration converts the elemental counts to major oxide (SiO_2, Al_2O_3, TiO_2, Fe_2O_3, K_2O, CaO, and MnO) concentrations in weight percent and the remaining elements in ppm. In addition to this calibration, the data were transformed using the ULC with the incoherent:coherent scatter ratio (ln([Element]/ICR)), counts per second (ln([Element]/cps)), and a conservative element (ln([Element]/[Si])) used as divisors to determine the impact on correlation between μXRF elemental intensities and ICP-OES/MS elemental concentrations (Cf. Gregory et al., 2019).

2.2.2 ICP-OES/MS

Fifteen subsamples, 8 mudstone and 7 sandstone (based on colour), were collected at roughly 2 cm intervals for analysis using inductively-coupled plasma techniques (ICP-OES/MS; see Figure 2.3). For brevity, we will simply use ICP to refer to these methods collectively. A rotary drill (Foredom TX Series) with a diamond-encrusted carbide milling tip was used to collect about 0.2 g of material from individual laminae and pulverize the material into a fine powder (< 40 μm). Each sample had a vertical width and penetration depth of 2-3 mm, while the horizontal length varied between 10 and 20 mm, which is a total sample footprint of ~40-180 mm^3. Samples were digested and analysed by Activation Laboratories Ltd in Ancaster, Ontario, Canada using a lithium metaborate/tetraborate fusion technique and analysed by ICP for major and trace element concentrations; oxide results were presented for comparison with the Cody-calibrated μXRF data.

2.3 Results

2.3.1 Itrax Reproducibility

Spectra from each sample interval record the total counts (cts) of energy intensities, which are compared to the 'expected' intensity curve based on the user-defined elements using a least mean-square error (MSE) method. The average individual MSE for all intervals in the four runs was 1.28 (1.02-1.77, n=2284) so there was good fit between the energies detected and the user-defined elements (expected curve). The 55-60 elements that were detected in the scans were reduced to 16 elements that are common to palaeoenvironmental research (e.g., Gregory et al., 2019; Croudace et al., 2006; Thomson et al., 2006) and had sufficiently high intensities ($\sim 10^2 - 10^5$ cts): Al, Si, S, K, Ca, Ti, V, Cr, Mn, Fe, Cu, Ni, Rb, Sr, Zr, and Ba. Boxplots, which are effective at showing the spread and summary statistics of a dataset, were used to compare the data between each run (n=4; Figure 2.4). The box (interquartile range; 3Q-1Q) contains 50% of the data, with the median value represented by the notch and any outliers indicated by circles beyond the 'whiskers'. Major elements (K, Ti, Ca, Si, Fe, Sr) all showed less than 1% variation in the median value while Al, Zr, Rb, Cr, Mn, Ni, and S had $< 3\%$ variation. The elements V, Cu, and Ba showed the most variation between the median values, although it was still $< 5\%$. Even the elements that showed more outliers, such as Ca, Sr, Zr, and Si, had similar outlier values across all four scans. The near-overlapping median and box range values across the four scans indicates that the true median values are similar (95% confidence interval). Scatterplot comparisons between two scans showed strong to very strong average Spearman correlation ($R^2 > 0.6$; cf. Leclezio et al., 2015; Selala et al., 2019) for Sr, Rb, S, and Zr, with Fe, Ca, Ti, K, and Si having correlation values greater than 0.96. The remaining elements all showed weak to very weak correlations ($R^2 < 0.4$) with increased scatter about the $y = x$ regression line, although a linear trend was still apparent in Mn and Cu, likely due to the overall lower concentration of these elements (see subsection 2.3.2).

2.3.2 ICP-OES/MS Elemental Concentrations

Lithogeochemistry derived from ICP analysis showed 10 oxides and 45 individual elements. Two of the oxides (MgO and Na_2O) were of elements that are too light for μXRF detection and one (P_2O_5) was not detected so they were excluded from further analysis; combined, these three oxides comprised $< 4\%$ of the sample by weight. The remaining oxides (SiO_2, Al_2O_3, TiO_2, Fe_2O_3, K_2O, CaO, and MnO) comprised between 82.6 and 91.77 (median = 87.35) weight percent of the sample, with SiO_2 being the most prevalent (median = 67.47%; 59.32-74.03), followed by Al_2O_3 and CaO, Fe_2O_3 and K_2O,

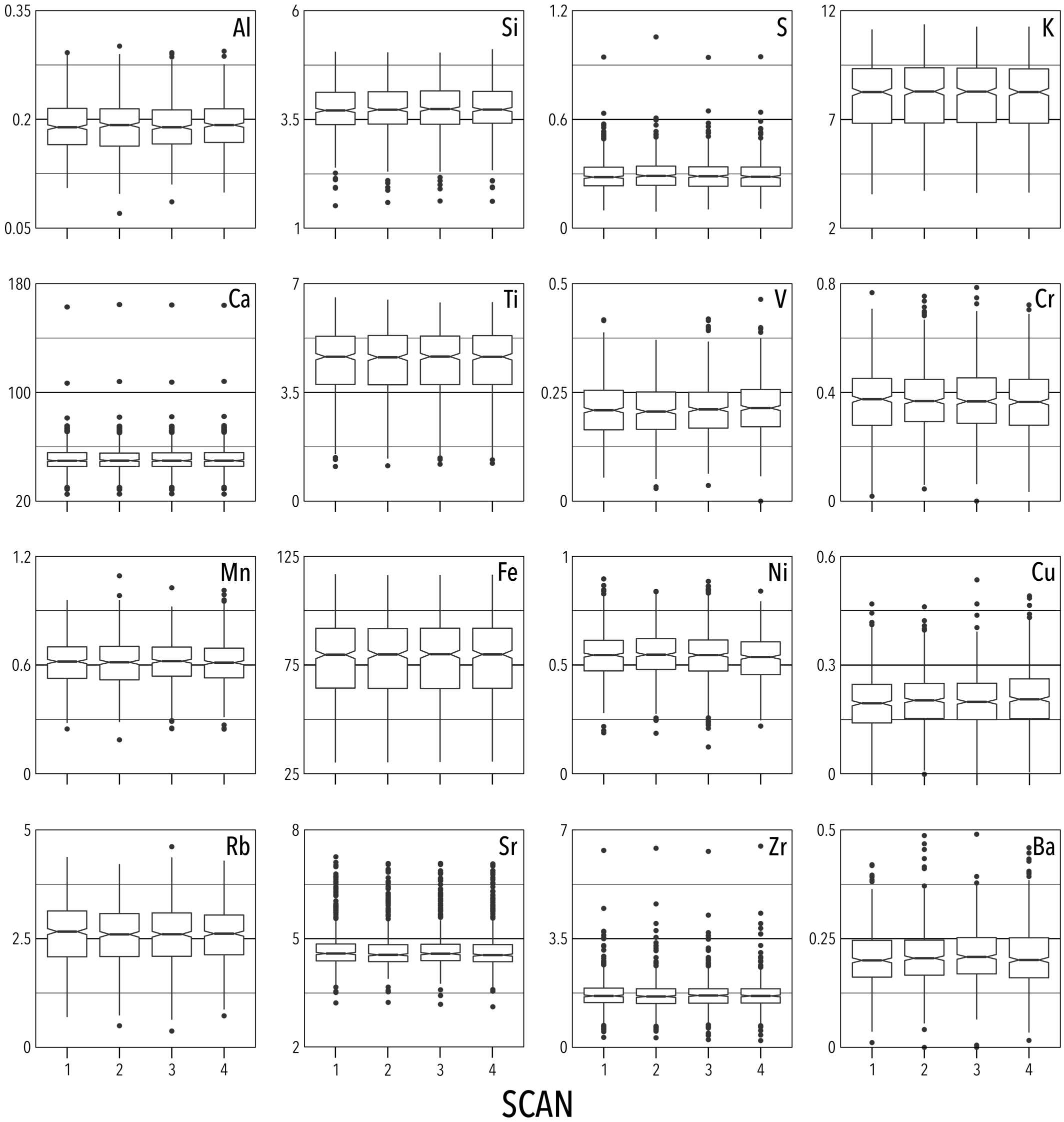

Figure 2.4: Boxplots of the elemental data, in kilo-counts (kcts), from scans 1-4. The notch represents the median value and the circles represent outliers. Note that even in elements with greater numbers of outliers (e.g. Ca, Zr, Sr), their values are similar between runs.

and trace amounts of TiO_2 and MnO. For the remaining elements of interest, Ba had the highest concentration (median = 309 ppm; 269-331), followed closely by Zr (median = 162 ppm; 143-205), Sr (median = 152 ppm; 137-238), and Rb (median = 87 ppm; 33-109); Cr, V, Ni, and Cu (in order of decreasing concentration) all had median values below 100 ppm.

The ICP data were quite distinct in the two different lithologies. The mudstone intervals had higher concentrations of Al_2O_3 and K_2O, likely incorporated into illite and kaolinite, as well as higher concentrations of TiO_2 and Fe_2O_3, while the sandstone intervals were typically higher in SiO_2 (quartz), CaO, and Zr/Rb. The Zr values on their own did not show a clear correlation to lithology so the Zr/Rb ratio is mainly driven by the Rb content, which is consistently at least 50% higher in the mudstone laminae. The mudstone intervals were also less oxygenated overall than the sandstone, as seen in the redox-related proxies MnO/TiO_2, which decreases with lower oxygen conditions in the sediment (Croudace et al., 2006; Thomson et al., 2006), and Redox (sum of V, Cr, and U), which increases with decreasing oxygen in sediments (Ben-Awuah et al., 2017; Tribovillard et al., 2006; Dypvik and Harris, 2001).

2.3.3 Comparison of ICP-OES/MS to μXRF

Absolute elemental concentrations from ICP analysis were compared to the batched Itrax data, the Cody Shale calibrated data, and log-ratioed (ULC) data to assess the fit between the μXRF elemental intensities and the absolute concentrations obtained through ICP analysis. At each ICP sample depth, the μXRF data were averaged over an 11-point window, centred on the depth, to provide the same number of total observations ($n = 15$) and to account for the ~2-3 mm span of the ICP samples; an 11-pt window is equivalent to 2 mm. While this provided a good way to compare the two datasets, there will still be some discrepancy due to the micro-scale analytical footprint of an Itrax core scanner (~0.8 mm^3) compared to the total coverage of the subsamples collected for ICP analysis (40-180 mm^3; see section 2.2). For example, if the lamina is at an oblique angle to the slab surface, then material from different lithologies can be incorporated into the homogenised ICP subsample, which would not be present in the volume of material analysed by μXRF. Similarly, micro-shells and fragments may be present in the lamina, which would be incorporated into the ICP subsample but may not be abundant enough to pass directly beneath the X-ray detector of the core scanner.

Bivariate plots, comparing the ICP- and μXRF-derived oxide data using a linear smoother ($y \sim x$) and Spearman correlation coefficient, were produced to show the correlation between the two analytical methods (Figure 2.5). Most of the oxides (SiO_2, Al_2O_3, TiO_2, Fe_2O_3, and K_2O) showed strong Spearman-Rho correlation coefficients of $R^2 > 0.6$ between the ICP and μXRF data, whether the μXRF data were calibrated to Cody Shale (wt.% and ppm) or left uncalibrated (counts). The ICP-derived MnO had a strong correlation ($R^2 = 0.66$) when compared to the calibrated data but only a moderate correlation ($R^2 = 0.50$) when compared to the uncalibrated data due to increased scatter about the $y = x$ regression line; however, a clear linear trend is still apparent in the scatterplots. The CaO concentration showed only moderate correlation for both calibrated and uncalibrated μXRF data ($R^2 = 0.52$ and 0.42, respectively) and had a higher level of scatter about the regression line however, the correlation would be stronger without a few outliers. The removal of the two highest outliers (red points, Figure 2.5), corresponding to depths of 60.6 mm and 137.6 mm, yielded R^2 values of 0.67 and 0.62 for calibrated and raw μXRF data, respectively. The Si-log-normalised data showed stronger correlations to the ICP concentrations compared to the uncalibrated and calibrated data for Fe ($R^2 = 0.83$), K ($R^2 = 0.70$), and Ti ($R^2 = 0.72$) but similar values for Al ($R^2 = 0.69$) and Mn ($R^2 = 0.65$). The relationship between CaO from ICP and Si-log-normalised Ca from μXRF had a near zero correlation ($R^2 = 0.02$), possibly due to the moderate positive correlation ($R = 0.57$) between Ca and Si, compared to the strongly negative ($R = -0.89$ to -0.95) relationship between SiO_2 and the other oxides. Since none of the calibrations resulted in significantly better correlations for all elements, the uncalibrated μXRF data will be presented for the remainder of the paper.

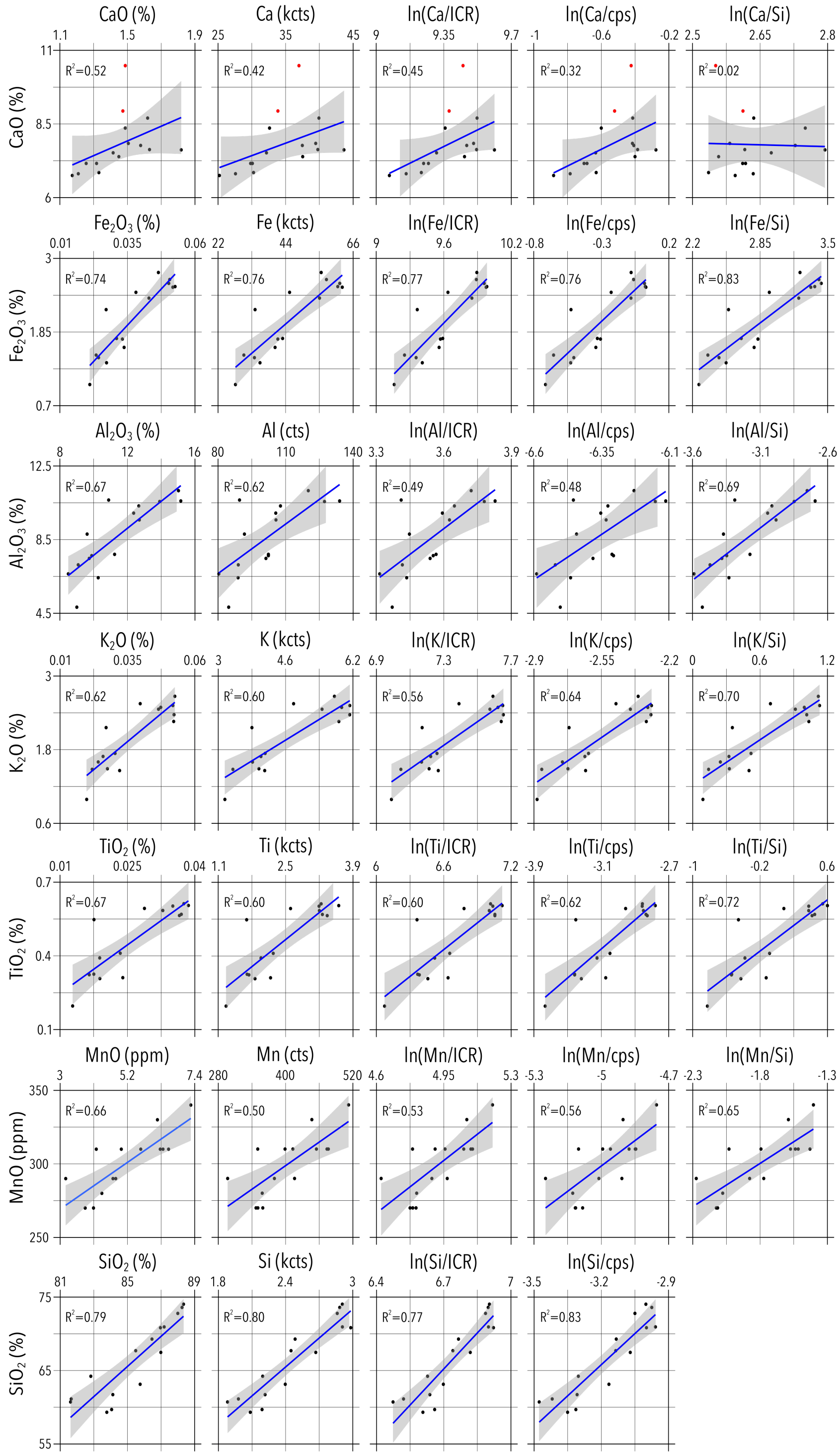

Figure 2.5: Bivariate plots of ICP-OES/MS results (y-axes) compared to various calibrations of Itrax results: Cody-shale calibrated (%), QSpec-batched (counts), and log-normalised. Red points in CaO graphs represent the outliers that result in weaker correlations.

Overall, these correlations are similar to those found by Gregory et al. (2019) when analysing modern lake sediments and in some cases better, though direct comparison is not possible as they used Kendall's tau correlations.

The elemental variation as a function of depth shows that the aliased μXRF data are very similar to the ICP concentrations (relative pattern of variation; Figure 2.6). When comparing the Al values, the μXRF data showed an overall smoother curve (less variation) than the ICP data, particularly in the middle six intervals from 100-200mm, and the Cody-calibrated values (Al_2O_3) showed a more distinct trend than the uncalibrated Al. An opposite pattern can be seen in the Ca trends, where the μXRF data display a more prominent trend throughout, although neither Itrax trend produced the same peak at 137.6 mm as the ICP-OES data. To provide a semi-quantitative comparison of the trends, simple confusion matrices were generated to examine how data points shifted relative to their respective means, regardless of the magnitude of that shift. If both datasets moved in the same direction (i.e. increased/decreased) relative to their respective mean then a 1 was assigned, otherwise a zero was assigned; the total 1s and 0s are presented in Table 2.2. Nearly all of the elements show simultaneous movements in both datasets, with the raw Ca trend showing the least similarity (60%) to the calcium oxide ($CaO_{ICP\text{-}OES}$) trend; however, when the oxide and raw Ca and Ti values are ratioed the trends become more similar (73%). The data sets moving opposite to each other could be the result of sampling errors while preparing material for ICP-OES analysis, which requires a larger sample size, so subtle offsets within the lithology could create discrepancies in the data. However, in the case of 'Redox' (V+Cr+U) the lower correlation is likely a result of the lower overall concentration of these elements (< 100 ppm; see subsection 2.3.2); a longer exposure time (e.g. 30 seconds) may increase the correlation of these proxies.

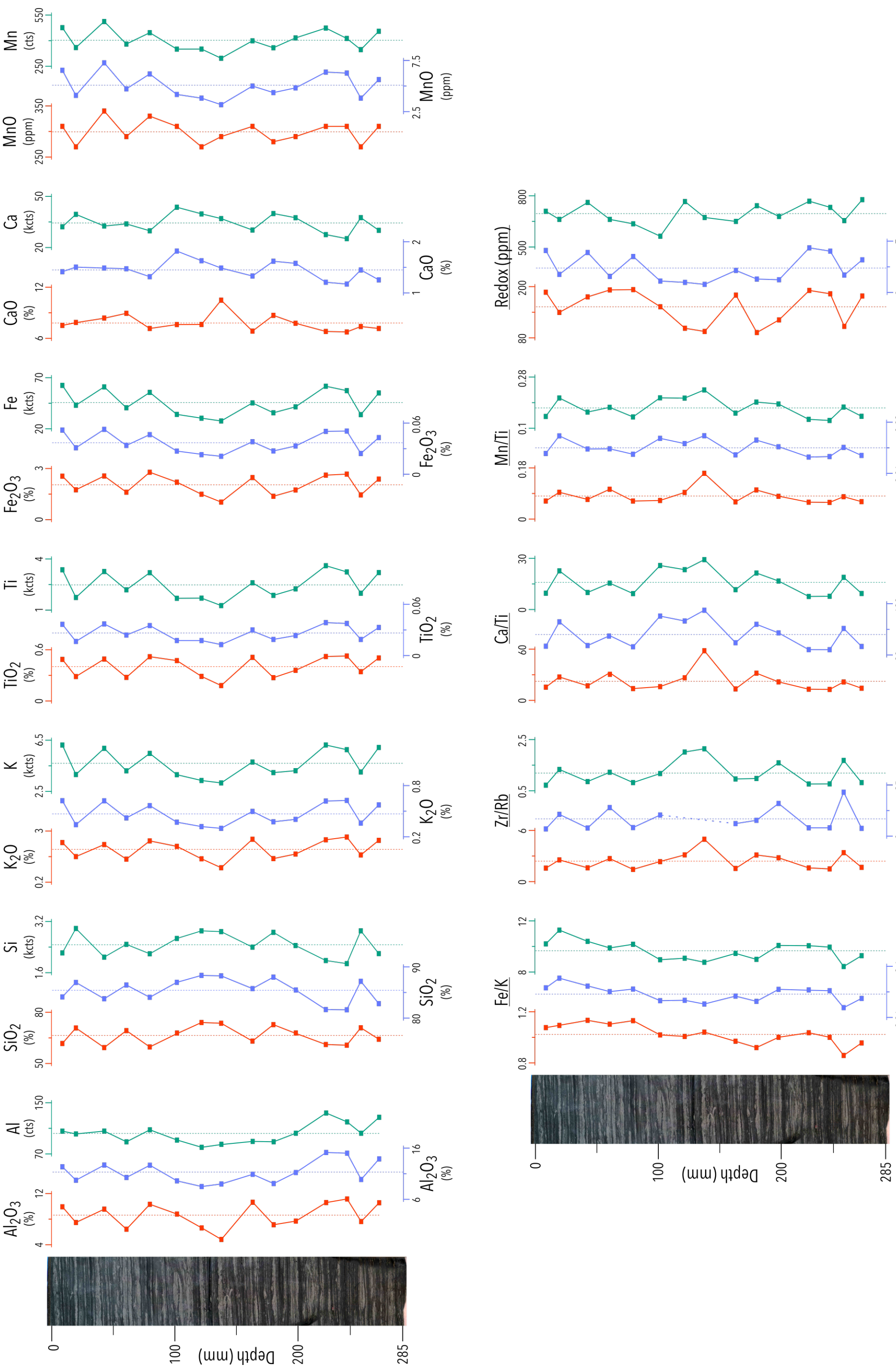

Figure 2.6: Oxide and elemental trends for ICP-OES (red), Cody-calibrated μXRF (blue), and batched μXRF (green) data. The Cody-calibrated Zr/Rb had two infinite intervals (121.6 and 137.6 mm) due to zeros in the Rb data so there is a break in the trend. The fine dashed line on each graph represents the mean.

Table 2.2: Confusion matrix results of single and ratioed elements; Redox = V+Cr+U. In the Cody-calibrated μXRF dataset, all but three Rb values were either 1 or 0 so the Zr/Rb trend could not be compared to the ICP trend accurately. Same (1): values (ICP and μXRF) responded the same relative to their respective means; Diverge (0): values responded in opposite directions relative to their respective means.

Single Elements

Oxides

	Al_2O_3	SiO_2	K_2O	TiO_2	Fe_2O_3	CaO	MnO
Same	13	14	14	14	14	12	13
Diverge	2	1	1	1	1	3	2

Raw Elements

	Al	Si	K	Ti	Fe	Ca	Mn
Same	11	14	14	14	13	9	12
Diverge	4	1	1	1	2	6	3

Element Ratios

Oxides

	Zr/Rb	$Redox$	CaO/TiO_2	MnO/TiO_2	Fe_2O_3/K_2O
Same	–	12	11	11	12
Diverge	–	3	4	4	3

Raw Elements

	Zr/Rb	$Redox$	Ca/Ti	Mn/Ti	Fe/K
Same	14	9	11	12	12
Diverge	1	6	4	3	3

2.3.4 Lithofacies

Lithologic analysis of the Cheese Slab showed mostly continuous laminae, with a low-angle inclination and preserved sedimentary structures (e.g. ripples, grading, cross-laminations; Figure 2.7). Petrographic analysis of thin sections showed that the sandstone laminae were mostly well-sorted and dominated by subangular, very fine sand- to coarse silt-sized quartz grains, with varying amounts of carbonate minerals, including subhedral grains and interstitial cement (Figure 2.8). Using X-ray diffraction (XRD) on a different section of the same core block, Grigg (2016) determined that feldspars were also a minor component of the sandstone but they were coated with calcite cement; therefore some of our carbonate grains may in fact be feldspars (see Figure 2.8A). Mineral grains in the mudstone were too small for visual identification but XRD analysis (Grigg, 2016) indicated these laminae to be dominated by illite and kaolinite, with higher concentrations of organic carbon relative to the quartz-rich sand laminae; Birgenheier et al. (2017) found similar results in their analysis of Blue Gate shale. Organic macerals up to very fine sand size can be observed in most laminae but in the mudstone intervals they also appear as distinct, though discontinuous, sub-millimetre thin beds, possibly settling out of a storm-enhanced fluid mud by flocculation (e.g., Plint, 2014).

Bioturbation throughout the section was low to moderate, with a Bioturbation Index (BI) of 1-4 (mean 2), which is a semi-quantitative measure indicating the ratio between preserved and disturbed sedimentary structures as a result of burrowing infauna. A BI of 0 indicates few or no burrows or trace fossils, BI of 3 indicates roughly 50% of the sedimentary structures (laminae) remain, and a BI of 6 is completely burrowed with no laminae preserved. Trace fossils of *Palaeophycus*, *Teichichnus*, *Planolites*, *Chondrites*, *Helminthopsis*, and *Zoophycos* were identified, which form the *Cruziana* ichnofacies (MacEachern et al., 2010) or the more proximal *Phycosiphon* ichnofacies recently described by MacEachern and Bann (2020), indicative of deposition in the sublittoral zone on a moderate- to low-energy medial shelf. Very rare (∼10 total) 'rotalid' and 'bolivinid' type calcareous foraminifera were observed in thin section with good preservation indicating that they were likely part of the living benthos at the time of deposition. The chambers were filled with carbonate cement (Figure 2.8C, D) and would produce anomalously high Ca values if the μXRF analysis passed over one directly, which could explain the lesser degree of correlation between the Itrax- and ICP-derived Ca concentrations.

Laminae were characterised and grouped according to their grain size, sedimentary

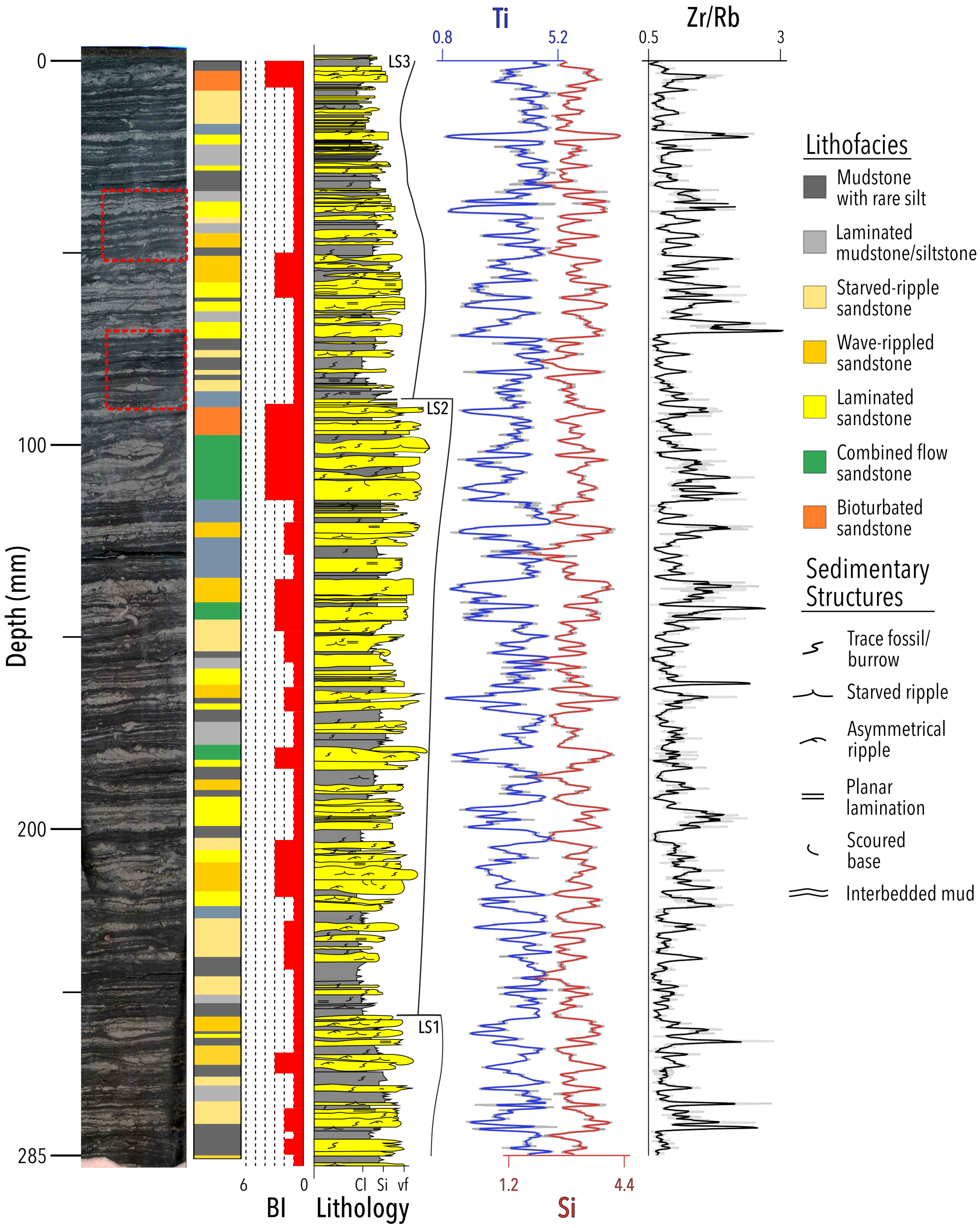

Figure 2.7: Core photo, lithofacies, BI, measured section, and μXRF-derived elements and ratios. The negatively-correlated Ti and Si trends closely follow changes in the lithology, with diverging trends associated with coarser-grained laminae. The dashed red boxes correspond to Figure 2.8 and the blue band represents the track of the 2 mm wide scanning beam. For the measured section, Cl = clay, Si = silt, and vf = very fine sand. The laminasets (LS1-3) are identified next to the lithology. Values for Ti and Si are in kilo-counts.

structures, and degree of bioturbation into 7 different microfacies: 1) mudstone with rare silt (29% of the section); 2) mudstone with laminated silt (12%); 3) starved-ripple sandstone (10%); 4) wave-rippled sandstone (17%); 5) combined-flow-rippled sandstone (12%); 6) laminated sandstone (14%); and 7) bioturbated sandstone (6%). Wave ripples were distinguished based on their symmetrical profile and the presence of convex-up cross-laminations, while combined-flow ripples have a slightly asymmetric profile and concave up cross-laminations (Figure 2.9); no ripples observed showed a highly asymmetric cross-section suggesting deposition by a solely unidirectional current. The presence of cross-laminations and symmetrical and asymmetrical ripples suggests that the sediments were dominated by combined flows. In thin section, the laminae show both normal grading, often with sharp and scoured basal contacts, and inverse grading, with evidence of bioturbation at the upper contact. Some intervals also display inverse- to normal-grading successions that are typical of river-fed hyperpycnal flows, however, the interpreted depth and distance from the shoreline based on the other proxies suggests that these intervals are either very distal expressions of river-fed hyperpycnal flows or they are wave- and current-generated hyperpycnal flows (e.g., Bhattacharya and MacEachern, 2009).

Increasing thickness and frequency of sandstone laminae was used to identify laminasets, which have sharp, upper contacts and an increase in wave and combined-flow reworking of the laminae approaching the top of a laminaset. Three laminasets (LS1-3) were identified in the Cheese Slab, though only LS2 is complete. The basal contact of the first laminaset, LS1, is not present but the top contact is visible at ~255 mm, where wave-modified sandstone laminae (Microfacies 4) transition to a mudstone-dominant unit with sparse silt (Microfacies 1). Moving upcore, LS2 shows a complete succession of mudstone with rare silt (Microfacies 1) at the base followed by an overall increase in sandstone laminae and evidence of wave and combined-flow reworking (Microfacies 5) up to 80 mm. Bioturbation, which has been used as a proxy for sedimentation rate (e.g., Bhattacharya et al., 2020, 2019), is higher at the top of LS2 than LS1, including a large *Zoophycos* burrow at 100 mm, indicating a significant decrease in the sedimentation rate, or a possible depositional hiatus, between LS2 and LS3. Laminaset 3, which is also incomplete, shows a more rapid transition from laminated siltstone-mudstone to combined-flow sandstone, with several millimetres at the base of LS3 compared to 30-40 mm at the base of LS2.

Generally, the grading patterns in the lower half of the core are more gradual and complete, with few sharp contacts until the upper few centimetres of LS2. Above 100 mm, the laminae show more fining upward successions with abrupt basal contacts and evidence of scour indicating more frequent, higher energy events. This pattern of fining upward with a sharp basal contact is indicative of an ignitive surge (Mulder et al., 2003), such as a wave-enhanced sediment gravity flow (WESGF; Macquaker et al., 2010), so this could represent a transition to more frequent storms in LS3. However, there is also a decrease in evidence of wave reworking (i.e. more parallel laminations) so the area of deposition may have shifted slightly below storm-wave base. Alternatively, the climatic conditions that existed during the deposition of LS2 may represent a period of above-average storm intensity, thus increasing the depth of storm-wave influence. Since the exact location of the core is unknown we are unable to provide an age but if we assume sedimentation rates of several tenths of a millimetre per year then the core represents roughly 200-300 years, so the climatic conditions of LS2 could be operating on a centennial-scale cycle; this would need to be investigated over a longer section (i.e. a few tens of metres).

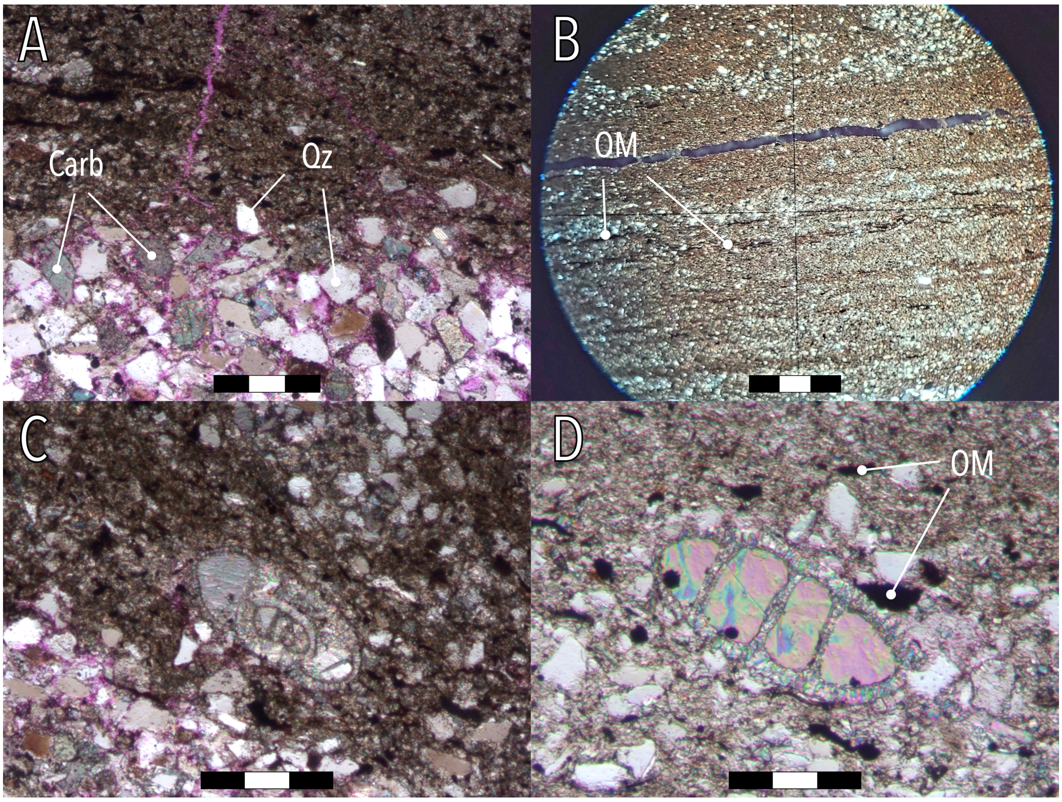

Figure 2.8: Thin Section photomicrographs in XPL: A) Grain size and mineral content comparison between the sandstone and mudstone intervals (Carb = Carbonate, Qz = Quartz, scale bar = 0.25mm). As noted in the text, the carbonate grains may actually be feldspar coated in calcite as seen by Grigg (2016); B) Fine-grained laminations in a siltstone-dominant heterolith (Microfacies 2). The mostly continuous laminations are indicative of the intermediate mudbelt; note the fine organic matter (OM) condensed horizons (scale bar = 1mm); C-D) Benthic, rotalid calcareous foraminifera with infilled chambers of carbonate cement (scale bars = 0.25mm).

2.4 Discussion

2.4.1 μXRF and Lithology

The μXRF-derived Ti, Si and Zr/Rb curves showed good correlation to the lithology and provided for added interpretation of coarsening- and fining-upward successions (see Figure 2.7). In this section, the sandstone intervals had higher Zr/Rb, Si, and Ca values,

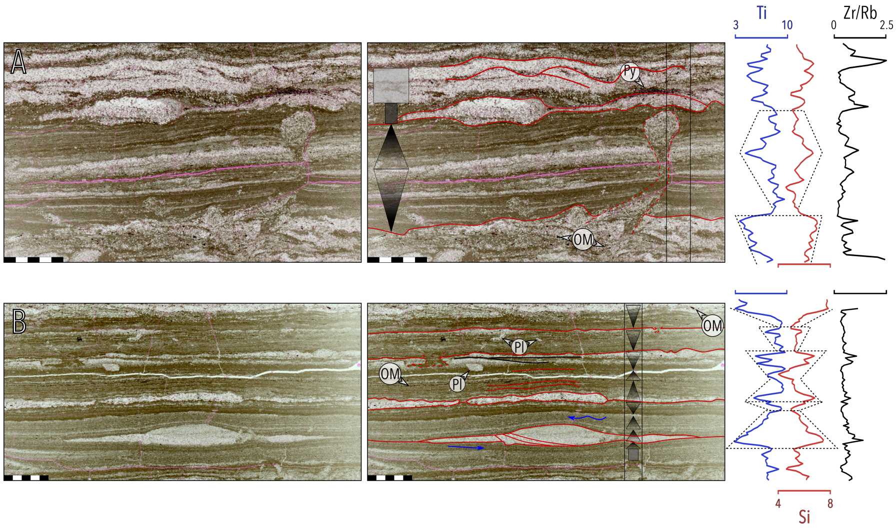

Figure 2.9: Sedimentary structures as seen in thin section (plane-polarized light). Dashed red lines indicate burrows and black box indicates location of scan. Notice the presence of combined flow in the starved ripple in B, as indicated by the blue arrows, compared to the undulating tops of wave-modified sediments at the top of A. Pl = *Planolites*, OM = organic matter, Py = Pyrite (see Figure 2.10). Ti and Si values are in kilo-counts (kcts).

while mudstone intervals were associated with Fe, Ti, K, and Al. The Zr/Rb ratio is a common grain-size indicator, with increasing values corresponding to coarser-grained sediments due to zirconium being contained in the heavy fraction, predominantly as zircons, while rubidium resides in the clay fraction from weathered aluminosilicates (Beil et al., 2018; Wang et al., 2011).The positive correlation between Si and Ca that we identified was also noticed to occur periodically in a 325 m long continuous succession from the Cretaceous Tarfaya Basin of southern Morocco (Beil et al., 2018). They interpreted these intervals as representing sediment winnowing and subsequent carbonate cementation at the trangressive surface, based on correlation to lithology, stable isotopes, and foraminifera. It is unlikely that the short length of the Cheese Slab is recording that large-scale of an event so the winnowing in our section is likely the result of increased turbulence at the seabed. In addition to identifying the coarsening- and fining-upward successions, the Ti, Si, and Zr/Rb curves provide information regarding the relative grain size changes through the section. The bottom half of the core shows more gradual changes as well as lower overall peaks, especially in the Zr/Rb values, while the upper 75 mm show the sharp basal contacts that are also identified in the lithology. The correlation can also be seen at the microscopic scale where the Ti, Si, and Zr/Rb follow the normal and inverse grading trends and can be used to identify sharp or gradual contacts. Even in cases of increased bioturbation, the underlying gradational trend is visible (see Figure 2.9).

Comparing the elemental intensity trends from the μXRF data to thin sections also allowed for a better understanding of the mineralogy (Figure 2.10). Since μXRF core scanners are not able to determine the oxidation state of the elements, it is not possible to know the mineral phase they are contained in. For example, Fe can be found as an oxide (Fe_2O_3), associated with carbonate as siderite ($FeCO_3$), or associated with sulphur as pyrite (FeS_2) depending on whether it's Fe^{2+} or Fe^{3+} as a result of the redox state in the sediments (Little et al., 2015; Tribovillard et al., 2006). However, comparing multiple elements and ratios allows for an accurate mineralogic composition to be obtained. The peaks in Si/Ti, Ca/Ti, and Mn/Ti ratios match the coarse-grained laminae and indicate an abundance of quartz and carbonate. The mudstone laminae were enriched in Fe, Ti, K, and Al indicating that these elements are being deposited in the clay fraction, mainly as illite and kaolinite, though visual identification of mineral grains in these layers was not possible. There are many thin, opaque laminae composed of organic matter present throughout these layers but in a single location at ~60 mm there is a peak in both the Fe and S/Fe curves indicating the presence of pyrite (i.e. sulfate-reducing conditions). This is a very localised phenomenon so this just indicates that while the benthos was mostly oxic to dysoxic, some areas may have been anoxic to euxinic (see Figure 2.9A); this relationship could prove effective at identifying anoxic intervals in longer cores.

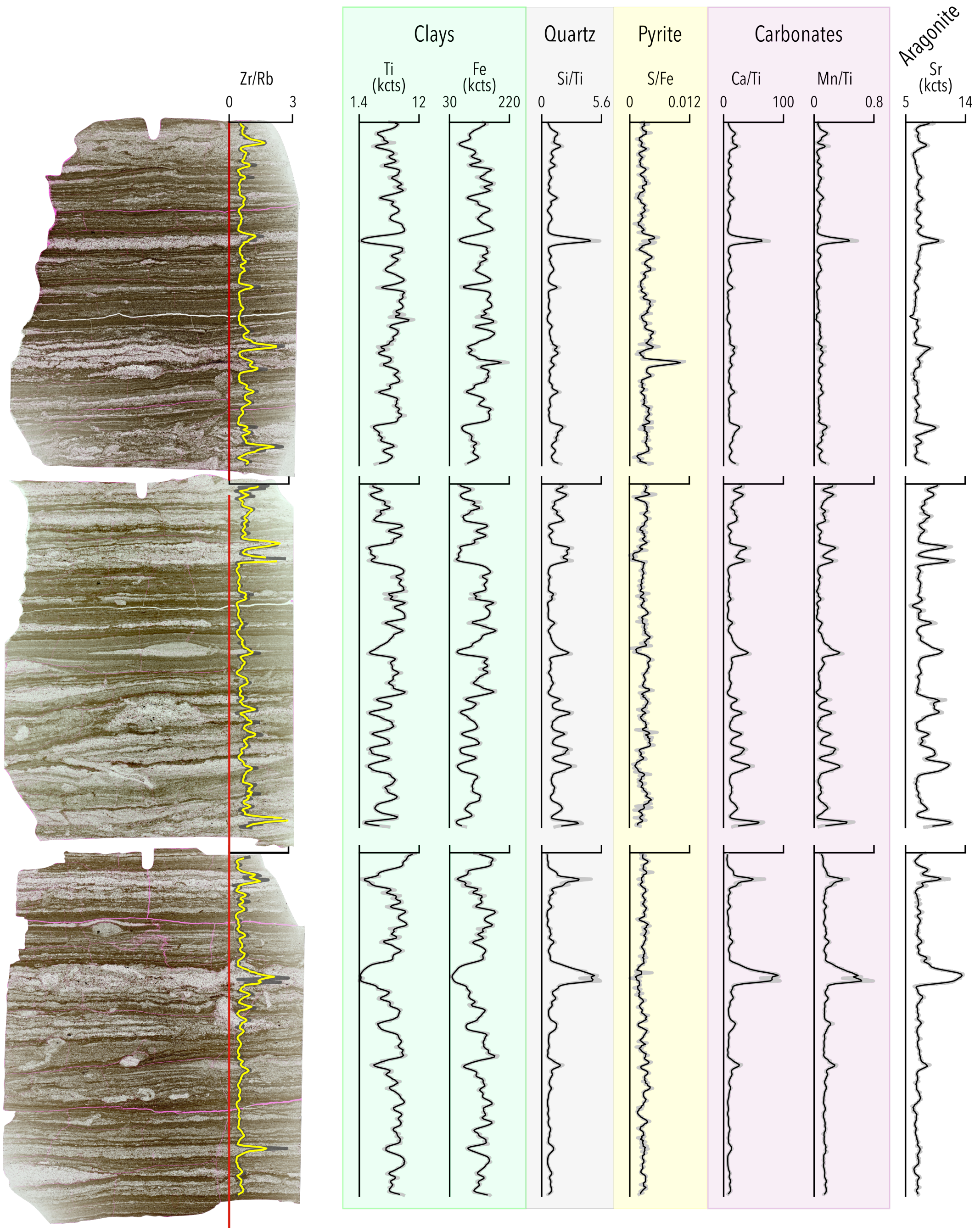

Figure 2.10: Comparing the μXRF signature to mineralogy. Scanned thin section images are in plane-polarized light. The peak in S/Fe in the top thin corresponds to the pyrite seen in Figure 2.9A.

2.4.2 Depositional Environment

Both the lithofacies and ichnofacies indicate the depositional environment to be close to, or just below, storm-wave base and influenced by offshore bottom currents. The WIS is thought to be storm dominated, although in any given location we can not be certain how frequently the sea floor was influenced by large storms. Studies of linked river systems by Lin et al. (2019) and Sharma et al. (2017) suggest annual river flood occurences that may have been storm-driven so it is likely that the sea floor was influenced by storm activity on a decadal scale, possibly every few years. Given the ubiquity of burrowing, the presence of benthic foraminifera, and lack of anoxic chemofacies the sediment water interface was oxic, with very localised zones of dysoxic to anoxic conditions, as indicated by the rare presence of pyrite. These localised low oxygen conditions help to explain the low diversity of burrows as well as the preservation of organic matter, as seen in thin section. Depositional mechanisms of sediments are typically interpreted based on the grain size and structures in the laminasets. A complete river-fed hyperpycnite has inverse to normal grading patterns, as flow energy waxes and wanes, and may also show asymmetric ripples. However, differences in flood magnitude, duration, and the distance from shoreline can result in base-truncated (e.g. no inverse grading) sequences, which can then be difficult to distinguish from other event beds (e.g., WESGF, tempestite, turbidite; Mulder et al., 2003; Macquaker et al., 2010; Schieber, 2016)). Our results show that adding chemofacies analysis using μXRF data may help to distinguish between river-fed and remobilised marine sediments due to the high volume of data. Previous research (e.g., Baumgardner and Rowe, 2017) has applied hierarchical cluster analysis (HCA) to group the elements and provide a rapid and quantitative method to establish chemofacies. For our data, we applied an unsupervised clustering algorithm (self-organising map; SOM) to better understand the principle elemental controls. In a SOM, observations in multi-dimensional space compete for nodes in a grid (tesselation) based on a discriminant function (e.g. Euclidean distance between the node parameters and the observations), and the parameters of each node are re-evaluated as new intervals are assigned. Since the clustering results from the SOM are topologically invariant, it is possible to create hierarchical groupings of nodes based on their topological relationships. In this way, nodes can subsequently be grouped into higher order 'superclusters' and 'ultra-clusters' if desired. We further grouped our observation clusters ($n = 169$) into $k = 5$ 'superclusters' (Figure 2.11). The two main elemental controls on the superclusters were Sr, which was highest in supercluster 1 and correlated with the sandstone laminae, and Fe, which was highest in supercluster 5 and correlated with the mudstone layers. The higher levels of Sr, indicating the presence of aragonite, in the sandy layers shows that these sediments originated from a shallow marine source, rather than directly from a fluvial source, and are therefore likely submarine sediment flows aided by turbulent conditions at the seabed from wave action. Based on the combined characteristics, these sediments were likely deposited in the intermediate mudbelt, at or just below storm wave base (see Figure 2.2; cf. Facies 2.4 of Birgenheier et al., 2017 and Microfacies 1 of Plint, 2014). The increase in sharp-based, fining upward successions above 100 mm may indicate a shift to more frequent events and this is supported further by an increase in the Fe/K ratio (see subsection 2.3.3), which would indicate more intense weathering of terrestrial rocks (e.g., Zarriess and Mackensen, 2010; Zarriess et al., 2011).

2.4.3 Implications for Petroleum Geology

The chemofacies analysis of elemental trends and clusters demonstrated promising results for application to hydrocarbon exploration and production. When plotted next to each other, the Ti and Si curves were well correlated with the lithology and mimicked the appearance of wireline logs (gamma and resistivity), which are the foundation of correlating surfaces across a basin. However, the number of elemental proxies, including

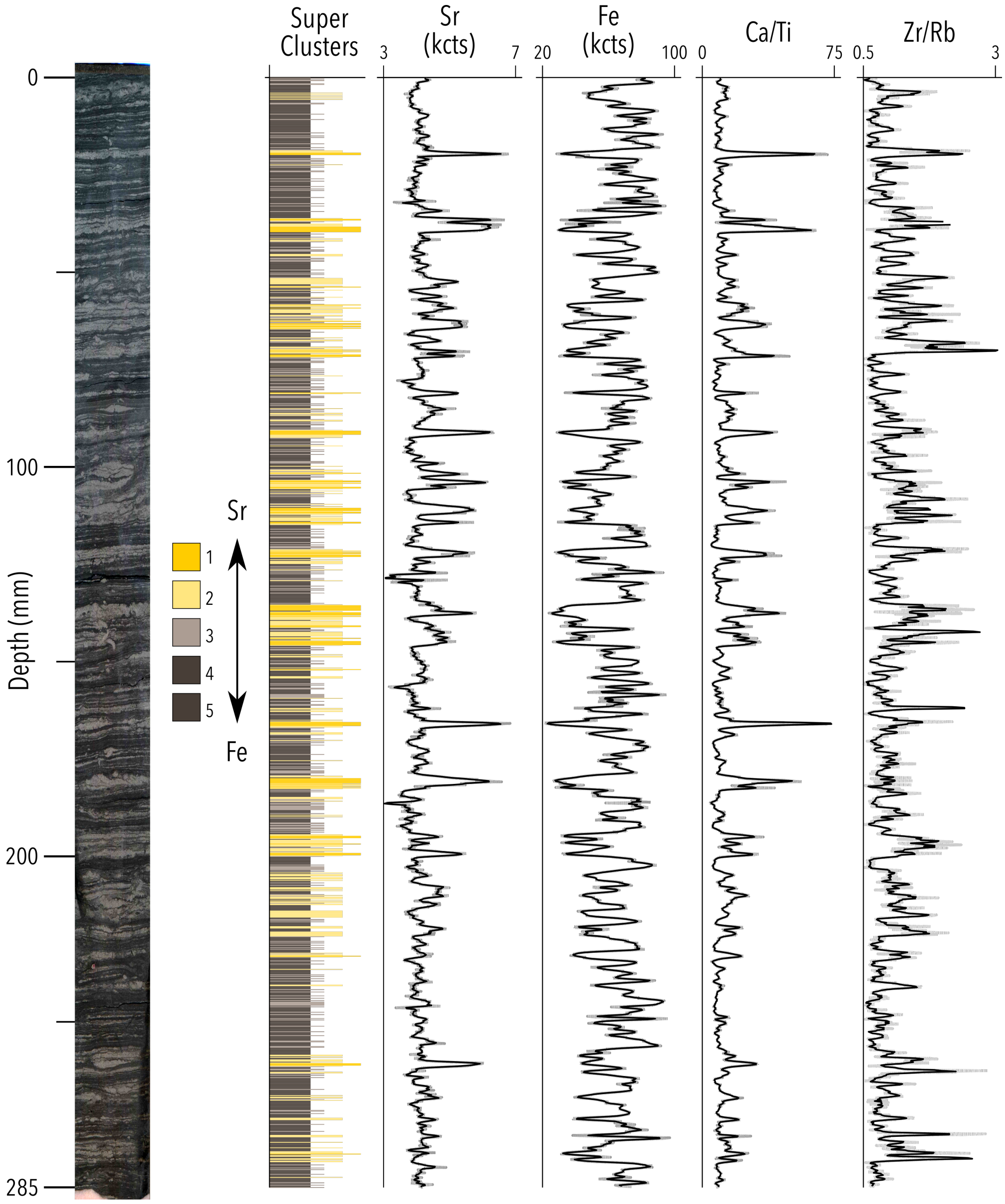

Figure 2.11: The supercluster results from the Self-Organising Map. Each interval was assigned to one of 5 superclusters, primarily controlled by Sr and Fe content, but K, Si, and Mn are also included in the decision tree. The superclusters were resized horizontally and coloured to correspond to lithology

ratios, and high-resolution vertical sampling obtained from μXRF core scanning allow for a more comprehensive investigation of the facies and have the potential to allow for more precise mapping (see Turner et al., 2016). For example, the presence of increased Sr in the sandstone layers indicates that these sediments were remobilised by wave action from a shallow marine environment as opposed to being directly river-fed, which provides information on the water depth and distance from shoreline. This information can be useful when correlating across multiple cores so as not to correlate a river-fed hyperpycnite with a wave-enhanced sediment gravity flow, which may have a similar lithology in the rock record.

Understanding the mechanical properties of fine-grained rock is an important factor in efficient hydrocarbon extraction as the mechanical strength, which increases with increased carbonate and silica cement, influences the geometry and extent of hydraulically induced fractures. Weaker, softer mudstones exhibit ductile deformation and may cause induced fractures to close due to rock creep. Grigg (2016) investigated the mechanical properties of the macro- and microfacies and their correlation to grain size and mineralogic composition. They found that XRD analysis, which is industry standard for assessing whether rocks will exhibit brittle or ductile deformation, lacks the resolution to characterise mudstones due to internal heterogeneity of micro-lithofacies. Our results show that μXRF analysis has the resolution needed to rapidly characterise the microfacies of very fine sandstone and mudstone based on relative grain size and composition, which would be beneficial in the planning of hydraulic fracturing activities.

Finally, superclustering with an unsupervised SOM shows promise for identifying significant boundaries, such as flooding surfaces, as well as providing information regarding sediment provenance (terrigenous vs. marine). By applying this method to the entire dataset first and then investigating the 'choices' made by the algorithm using a decision tree, the researcher is given a more complete characterisation of the chemofacies but still has the ability to use previous knowledge to interpret depositional mechanisms and environments. Our superclusters corresponded to visual changes in lithology when plotted by depth and resized and coloured based on comparison to the core. This method will need to be investigated further, first on longer successions and then to other cores laterally, to understand it's potential effectiveness at identifying regional bounding surfaces.

2.5 Conclusion

The data obtained from fine-grained sedimentary rock using an Itrax μXRF core scanner showed the same high level of reproducibility as demonstrated on soft sediment cores, with some major elements even demonstrating direct correlation between separate scans (Ca and Fe; $R^2 = 1$). The common elements Al, Ti, K, Fe, Si, Ca, and Mn showed strong to very strong Spearman correlation coefficients when compared to ICP-OES concentrations and both datasets showed similar down-core trends. The elements Cr, V, Ni, and Cu did not have as strong of a correlation due to their low concentrations (< 100 pmm). Overall, there was no significant impact to the correlation between μXRF elemental intensities and ICP-derived concentrations after calibrating the μXRF data using a variety of techniques. When the data trends (i.e. the positive or negative shift relative to the respective means) were compared using a simple confusion matrix, the correlations were stronger, with most of the elements moving in the same direction in each dataset in more than 80% of the samples.

The elemental signatures obtained from an Itrax μXRF core scanner showed strong correlation to the lithology and mineralogy at both a macroscopic and microscopic scale. The Ti and Si records, which were negatively correlated, effectively tracked lithology changes and could indicate sharp and gradational contacts, particularly when coupled with the Zr/Rb curve. When the data were clustered, a lower frequency signal was also evident indicating that the application of this method to longer successions of Mancos Shale could allow for a more accurate reconstruction of climatic and environmental changes within the Western Interior Seaway through the Upper Cretaceous. The μXRF data also provided added information regarding the mineralogic composition, showing that the sandstone layers had increased levels of Ca and Mn (as carbonates) and Sr (aragonite), indicating they had a shallow marine source. Therefore, it is likely that these laminae are recording submarine flows as a result of wave energy (e.g. WESGFs or tempestites) rather than direct input from river-fed hyperpycnites. In order to resolve these successions even further, palaeocurrent and bathymetric data would be required to determine whether the sediments flowed directly down slope or obliquely.

Our results indicate that fine-grained sedimentary rocks are ideal for palaeoenvironmental reconstructions using μXRF-derived elemental abundances as they minimise the sources of error caused by matrix effects in unconsolidated sediments such as organic matter, pore space, and water content. Additionally, fine-grained sediments from deeper basins typically display a more complete record than proximal, coarser-grained sequences as they do not undergo erosion or depositional hiatuses as frequently. The elemental trends and ratios used in this study were able to provide accurate information about petrography, depositional processes (turbidites, WESGFs), and environmental changes recorded in the mudstone succession at a significantly lower cost and analysis time. A single scan with the Itrax provided $n = 1425$ observations and was completed in less than 6 hours for ~\$150 USD compared to approximately three weeks and ~\$1300 USD required to prepare and analyse $n = 15$ samples with ICP-OES/MS. The high-resolution trends will also allow for more accurate correlation of climatic conditions across other Upper Cretaceous epeiric seas, thus improving our understanding of the climate system in a hothouse world.

Chapter 3.

Establishing high-resolution (500 μm) chemofacies of non-marine and marine depositional environments in the Upper Cretaceous Western Interior Seaway using a hierarchical clustering algorithm on μXRF elemental data.

This chapter has been prepared with the intention of submitting to the journal "Sedimentology"

3.1 INTRODUCTION

The origin and depositional mechanisms of fine-grained sedimentary rocks (mudstone) is an ongoing debate among sedimentologists, particularly when it comes to interpreting shallow- vs deep-water units. The upper-Devonian Bakken Formation of North Dakota, for example, is interpreted by roughly two-thirds of the studies as being a deep-water facies based on sedimentology (fine-grained, laminated clay), while the other third support shallow-water deposition based on stratigraphic relationships such as onlap patterns and the lack of landward-equivalent shallow-water strata (Petty, 2022). This discrepancy is due to the fact that mudstones are inherently difficult to map, owing to subtle variations in grain-size, texture, and sedimentary structures (Dypvik and Harris, 2001; Baumgardner and Rowe, 2017) and typically require petrographic thin-section analysis to detect lamination style and therefore interpret the depositional environment (Macquaker et al., 2010; Plint, 2014; Schieber, 2016; Birgenheier et al., 2017). Even electric well-log data (gamma radioactivity, spontaneous potential, resistivity) from these sediments can be relatively homogenous, showing more subtle variability down-core that can be difficult to characterise (Pearce et al., 1999; Turner et al., 2016). Despite the apparent visual and physical homogeneity, several studies have demonstrated that there is a significant level of variability in elemental abundances through these muddy successions (e.g., Algeo et al., 2004; Lash and Blood, 2014; Olde et al., 2015; El-Attar and Pranter, 2016; Beil et al., 2018; Profe et al., 2018), which can be used to establish detailed chemofacies descriptions based on dozens of proxies (elements and elemental ratios such as Fe/Ca, Ti/K, Zr/Rb) thereby improving the ability to interpret mudstones based on their depositional environment (Pearce et al., 1999; Turner et al., 2016; Pietras and Spiegel, 2018). However, studies using traditional techniques to analyse whole-rock geochemistry (e.g., ICP-OES/MS, WD-XRF, INAA) are often conducted at metre-scale sampling resolution and therefore merely provide ‘snapshots’ of the geochemical makeup of different mudstone units.

Advances in energy-dispersive X-ray diffraction (ED-XRF) analysis have allowed researchers to collect meaningful elemental data from cores at sub-millimetre sampling resolution using laboratory-based scanners, herein referred to as μXRF, providing much higher-resolution elemental data than is possible with traditional techniques. Micro-XRF core scanners, such as the Itrax Core Scanner (Cox Systems, Sweden), are able to detect the relative abundance of elements from Al (Z=13) to U (Z=92) at sampling intervals as low as 100μm, which is particularly important when studying mudstones with lower sedimentation rates or ancient sedimentary successions that have been vertically compressed. And while the data do not have the analytical accuracy of ICP-OES/MS (i.e., ppm or ppb), they have been shown to correlate well with absolute concentrations and mineral content obtained from traditional methods (Rowe et al., 2012; Gregory et al., 2019; Cerdà-Domènech et al., 2020; Gabriel et al., 2022a). Furthermore, since the instrument simply counts the number of emitted photons with a given energy, the elements are not subject to the dilution effect of traditional techniques, where the data are constrained to a unit volume (e.g., wt. % or ppm). The method is non-destructive and has been shown to have exceptional reproducibility between scans (Gabriel et al., 2022a), allowing for multiple analytical runs of the same sample to improve the signal-to-noise ratio. This paper uses lithology and high-resolution (500 μm) elemental data collected from an Itrax μXRF core scanner to describe the depositional environments in Upper Cretaceous (Turonian-Coniacian) coastal and marine sediments from the Western Interior Seaway of North America (WIS), with respect to their proximity to shoreline, weathering intensity at the seabed, and relative oxygenation in the sediment. These results will be important for establishing detailed geochemical signatures of these environments, particularly the more distal finer-grained units, which can then be applied to longer successions or cores from other epicontinental basins to enhance palaeoenvironmental interpretations and basin reconstructions.

3.1.1 Marine Depositional Environments

Conceptual models of depositional systems in epicontinental seaways with siliciclastic shorelines, such as the Upper Cretaceous Western Interior Seaway (WIS) of North America, demonstrate the general changes in sediment composition with increasing distance from shoreline and water depth (Walsh and Nittrouer, 2009; Bhattacharya, 2010; Hart, 2016; Birgenheier et al., 2017). Non-marine and shallow coastal sediments (shoreface, delta front), herein referred to as near-shore sediments, are dominated by coarser-grained siliciclastic sandstones with high concentrations of Ti, Si, K, and Al from fluvial input. Depending on biologic productivity, the shallow marine sands may also be enriched in aragonite (Sr) from macrofaunal shell precipitation (e.g., molluscs, gastropods). Deeper marine sediments, which are transported farther into the basin by wave- and current-enhanced sediment gravity flows (Macquaker et al., 2010) are dominated by fine-grained (silt and clay) deposits that transition from siliciclastic mudstones in the hemipelagic zone (prodelta and mudbelt) to more calcareous mudstones into the pelagic zone (sediment-starved shelf) (Hart, 2016; Birgenheier et al., 2017). The deltaic complexes of the WIS are interpreted to have been wave-dominated and therefore did not protrude as far into the basin as river-dominated deltas (Bhattacharya and Tye, 2004; Bhattacharya, 2006; Walsh and Nittrouer, 2009). In this type of system, the prodelta is typically limited in extent as the sediments are quickly re-worked, transported, and deposited along- and offshore in a wide, expansive mudbelt (many 10s to 100s of km; Hart, 2016), though the sediment accumulation may occur in more concentrated 'bulls-eye' areas due to various hydrographic and structural controls (i.e., the marine-dispersal-dominated (MDD) system of Walsh and Nittrouer, 2009).

As the depositional environment moves basinward and the water depth increases, the energy conditions at the seabed decrease, which decreases the amount of vertical mixing and oxygenation of the water column. This dysoxia is reflected by an increase in redox-sensitive elements, such as V, Cr, and U, which become insoluble in their reduced state and are therefore incorporated into the sediments. The lower oxygen conditions also increase the preservation potential for organic matter, which is reflected in variations in organophilic elements like Ni and Cu that can adsorb to settling organometallic ligands and thus be delivered to the sediments (Tribovillard et al., 2006). In some cases, these elements can be retained in the sediments even after the original organic matter has been consumed by microbial activity as post-depositional oxidation occurs (Thomson et al., 2006). Manganese, which precipitates out of oxic waters as Mn-oxyhydroxides but is soluble in its reduced state, also creates a very effective shuttle for delivering trace elements like Ni, Cu, and V to the sediments from the overlying water column, where they are released during reduction of the Mn-oxyhydroxides and are then available for other reactions (Tribovillard et al., 2006). While these general characteristics have been documented, the lower-resolution sampling is not as effective at identifying variability within these different environments where the changes may be highly localised. A more rigorous geochemical signature that combines multiple environmental proxies and their variance is needed to provide more information about the processes that are acting on the sediments at various points in the basin.

3.1.2 High-resolution Chemofacies

The amount of data obtained using μXRF core scanners can be difficult to analyse and interpret stratigraphically, particularly when trying to incorporate multiple proxies, and therefore multivariate statistical techniques are necessary to describe the chemofacies. The most common of these techniques is a Principal Component Analysis (PCA), which aims to minimise the dataset by identifying the proxies that are contributing to the most variance between observations (Wold et al., 1987; Abdi and Williams, 2010). While this may provide a good starting point for investigation, the results may be of limited use to marine sedimentology as the principal components are generally known and predictable (e.g., Fe, Ti, Si, Al for terrestrial siliciclastics) and the PCA does not provide a complete elemental characterisation of each observation. Hierarchical clustering algorithms (HCAs) are more effective at developing chemofacies since they can group observations according to their total elemental signature and therefore provide more information regarding how the geochemical composition is changing stratigraphically (Templ et al., 2008; Al Ibrahim et al., 2015; Baumgardner and Rowe, 2017). One such algorithm is known as a Self-Organising Map (SOM; Kohonen, 2013), which is an unsupervised, iterative algorithm where observations in multi-dimensional space compete for nodes in a regular, two-dimensional grid based on a discriminant function, typically the Euclidean distance between each observation and the nodes. Each node represents a different model that is spatially ordered so as new observations are assigned to each node, it's model parameters, as well as those from a subset of neighbouring models/nodes, are updated (Kohonen, 2013). By reducing the dataset to a much smaller set of models, the SOM clustering can be performed at least an order of magnitude faster and lighter (in terms of computational power) than traditional HCAs, which cluster the dataset by comparing every single point with all of the others (Kohonen, 2013). This makes it ideal for use with μXRF datasets, which can easily reach tens of thousands of observations e.g., an 1800 mm long core at 0.1-mm sampling interval would provide 18,000 data points. The initial SOM clustering is unsupervised, thus removing researcher bias, but as the clusters are topologically invariant they can be further grouped into higher order 'superclusters' to investigate the chemofacies at a variety of scales, depending on the research question. Gabriel et al. (2022a) demonstrated the potential utility of using a SOM for establishing chemofacies on a short (28.5 cm) section of highly interbedded (mud to very fine sand) Mancos Shale from the Uinta Basin using μXRF data at 200 μm intervals (1425 sample points). Their results showed that in addition to being rich in Si (quartz) the sandstone laminae were also higher in Sr (aragonite) indicating that the sediments were likely reworked and transported from a shallow-marine source rather than being directly deposited by fluvial processes.

3.2 MATERIALS AND METHODS

This study focuses on two separate Upper Cretaceous (Turonian-Santonian) sedimentary successions from the Western Interior Seaway (WIS) of North America (Figure 3.1), which occupied a retroarc foreland basin that initially formed during the Upper Jurassic (Oxfordian) as a result of subduction of the Farallon Plate beneath the North American Plate (Decelles, 1994; Miall et al., 2008; Birgenheier et al., 2017). Basin subsidence, combined with eustatic sea-level changes, resulted in several marine transgressions throughout the Cretaceous, with the most extensive transgression (+250 m) occurring at the end of the Turonian, when the WIS had a width of ~1500 km (Sageman et al., 1997; Miall et al., 2008; Joo and Sageman, 2014). The Upper Cretaceous climate was a period of sustained global warming, with extreme tropical sea-surface temperatures, ~35 °C, and high-latitude intermediate to bottom water temperatures ~20 °C occurring throughout the Turonian until ~91 Ma (Friedrich et al., 2012). The regional climate of the southwestern WIS through the Turonian, which lay between 30°N-40°N (Lin et al., 2019), was subtropical with consistent wet and humid conditions based on the abundance of coals and lack of evaporites (Bhattacharya and Tye, 2004), and the presence of swamp and floodplain palynomorphs in paralic settings (Akyuz et al., 2016); precipitation estimates are between 1500 mm/yr during sea-level lowstand and 2200 mm/yr during highstands (White et al., 2001). Studies of the Ferron and Gallup deltaic systems indicate fluvial discharge on the order of 10^2-10^3 m^3/s, which would have regularly produced hyperpy-

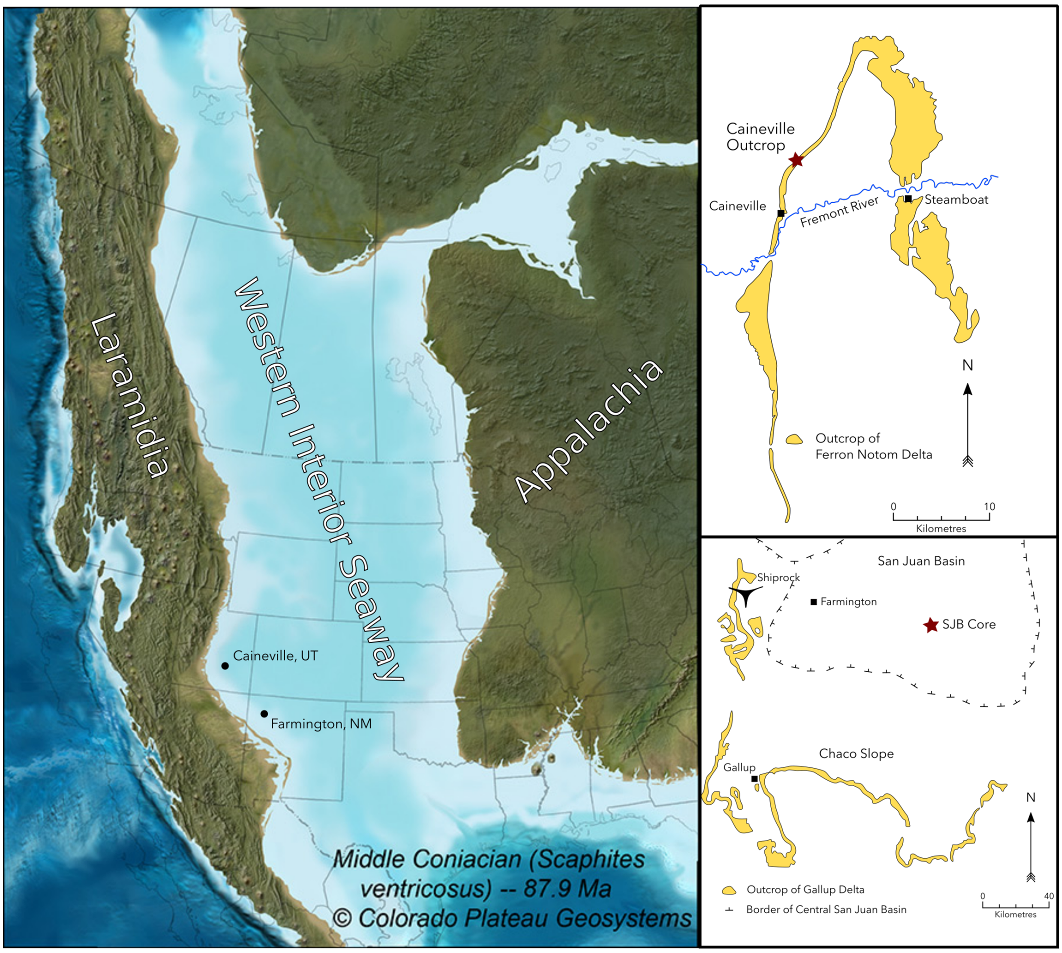

Figure 3.1: The Western Interior Seaway during the Middle Coniacian with the locations of the San Juan core (Well ID: San Juan 28-6 Ut 148M) and Caineville outcrop measured section. Basemap from Colorado Plateau Geosystems (www.deeptimemaps.com); Caineville outcrop map adapted from Zhu et al. (2012); Gallup outcrop map adapted from Campbell (1971).

cnal plumes, and that large storms likely impacted any given location on the coast at a decadal-scale frequency (Bhattacharya and Tye, 2004; Sharma et al., 2017; Lin et al., 2019). However, the more distal sediments around storm-wave base may have been impacted more frequently. Circulation models indicate an overall anti-clockwise circulation pattern in the WIS, with tropical Tethyan waters being drawn up the eastern margin and cooler Boreal waters moving south along the western shore, and that the confluence of these water masses was around modern-day New Mexico (Slingerland et al., 1996; White et al., 2001; Hart, 2016; Lowery et al., 2018).

3.2.1 San Juan Basin (SJB) Core

The first sedimentary succession, the *San Juan Basin (SJB)* core, is a 17-metre long section of Mancos Shale, a muddy shelf deposit from the WIS (Figure 3.1). The *SJB* succession was analysed using slabbed core that was collected by Schlumberger/TerraTek from the San Juan Basin in Rio Arriba County, New Mexico (Well ID: San Juan 28-6 148M; 36.6425°N, -107.4506°W) and archived at the New Mexico Bureau of Geology and Mineral Resources in Socorro, New Mexico. Several intervals of this core were loaned to McMaster University for non-destructive lithologic and elemental analyses and this study focuses on the interval between 6898-6955 ft (2102-2120 m) drilling depth. In the San Juan Basin, the Mancos Shale ranges from 500-700 metres thick and is informally divided into two units, lower and upper Mancos, which are separated by the end-Turonian Niobrara unconformity (Ridgley et al., 2013; Broadhead, 2015); this has also been called the Tocito unconformity (Molenaar et al., 2001). The lower Mancos, which intertongues with the underlying paralic Dakota Sandstone, is generally more heterogeneous, with five members: Graneros Shale, Greenhorn Limestone, Lower Carlile Shale, Juana Lopez Shale, and Upper Carlile Shale. The overlying upper Mancos on the other hand, which comprises between 275-475 m of the total thickness, is mainly dark, kerogen-rich marine shales with some interbedded marine siltstone and sandstone near the base that grades upward into mostly homogenous siliceous mudstone; it thickens from the southwest to the northeast moving towards the basin depocentre (Ridgley et al., 2013; Broadhead, 2015). Broadhead (2015) informally subdivided the upper Mancos into three separate units (from top), A, B, and C, based on prominent markers in gamma-ray and resistivity logs that indicated increased sand, silt, and possibly carbonate content; upper Mancos unit A is overlain by the Point Lookout Sandstone. The *SJB* core is from upper Mancos unit C and is interpreted to have been deposited between 150-180 km from the contemporaneous shoreline, associated with the deposition of the Dalton Sandstone and Dilco Coal members of the Crevasse Canyon Formation, based on comparison of the well-log data (NGR, resistivity) to the USGS Cross Section (Molenaar et al., 2001). Shelf slopes of the WIS were likely on the order of 0.04°-0.2° (Bhattacharya and MacEachern, 2009) so these sediments would have been deposited in ~100-125 m water depth. Each *SJB* core box, which contained up to 3 metres of core, was first photographed using a Nikon D3200 12-megapixel digital-SLR camera and the lithology was described to the lamina scale using the core and photographs so that contrast could be enhanced to accentuate the subtle variations in the more homogeneous intervals. Each visible lamina was measured and logged based on the presence of sedimentary structures such as ripple cross-bedding, laminations, and bioturbation. Where visible, bioturbation levels were ranked on the Bioturbation Index (BI; range 0-6), a semi-quantitative value indicating the amount of disturbance to laminae as a result of burrowing infauna, with zero indicating no disturbance and six indicating complete disturbance with few to no laminations remaining (MacEachern et al., 2010; MacEachern and Bann, 2020).

3.2.2 Caineville Outcrop

In addition to the SJB core, 29 samples were collected from an exposed outcrop of the Ferron-Notom deltaic system, near the town of Caineville, Utah, which includes mudbelt, prodelta, delta front, and fluvial channel belt and floodplain facies; there is no direct stratigraphic correlation between the core and outcrop samples. The full lithology and sequence-stratigraphic framework for this system was previously described and established by Zhu et al. (2012) based on 56 measured vertical sections, including this 180-metre Caineville section. The bottom of *Caineville* is represented by the prodeltaic facies of the Tununk Member, which conformably transitions into the overlying Ferron Member comprised of (moving upcore) prodelta, delta front, and finally fluvial channel-belt and floodplain facies. The fluvial sandstones and mudstones at the top of the Ferron Member are unconformably overlain by the deeper water mudbelt facies of the Blue Gate Member, indicating a major hiatus (~4 Ma; Zhu et al., 2012) due to a marine transgression. Each of the 29 samples (CN01-CN29) from this location were collected from finer-grained intervals within the larger units, including from the delta front and channel belts, to allow for a more accurate comparison to the mudstone deposits of the *SJB* core, which consists of mudbelt and sediment-starved shelf deposits of the Mancos Shale.

3.2.3 Elemental Composition

The elemental intensities were obtained using an Itrax μXRF core scanner with a molybdenum X-ray tube (30kV, 33mA), 500 μm vertical sampling resolution, and a 15 second exposure time to obtain elemental data for major, minor, and trace elements. The *Caineville* samples were disaggregated overnight in distilled water, mixed and centrifuged to homogenise and concentrate the sediment, and then loaded into an acrylic Sequential

Sample Reservoir (SSR) carrier for analysis with the Itrax (see Gregory et al., 2017, for methodology). The SSRs used for the Caineville outcrop samples were ∼1.5 cm long, which provided 27-30 data points for each sample. The *SJB* core was transferred from the boxes to an acrylic semi-tube, cut in half lengthwise, prior to being loaded into the Itrax, which allowed us to ensure a flat, level surface to maximise scanning integrity. Black, oil-based modelling clay was used to support the core and fill in gaps where necessary. The raw μXRF spectra from each scan were batch analysed to obtain elemental intensities using QSpec software (Cox Analytical Systems), which aims to minimise the mean-squared error between the obtained raw spectra and the 'expected' spectral curve based on the user-defined elements and X-ray tube parameters. All subsequent statistical analyses were performed in RStudio® (GNU Affero General Public License v.3) using R version 4.1.2+ (R Core Team, 2021).

In order to classify and group the observations of the SJB Core, the μXRF data were clustered using a SOM (SOMbrero package; Vialaneix et al., 2020) to group every observation according to its elemental signature, which could then be interpreted and compared to the Caineville depositional environments. The data were first centred using a row-wise Z-scale (row $\mu = 0$ and $\sigma = 1$) using every element detected in the batch analysis to normalise each element to the total signature of the observation. A selection of those row-centred elements with high (> several hundred) original counts (cts) and good detectability using μXRF (Croudace et al., 2006; Gregory et al., 2019; Gabriel et al., 2022a) were then used in the SOM: Al, Si, S, Ca, Ti, K, Sb, V, Cr, Mn, Fe, Ni, Cu, Zn, Rb, Sr, Zr, Th, U. The incoherent:coherent scatter ratio (ICR), which tends to vary with sample density (Brown et al., 2007; Boyle et al., 2015), was also included in the SOM. The initial tesselation is a square grid of $\sim 5\sqrt{n}$ nodes (n = 33,871), which, in this case, is approximated by a 30x30 grid. These 900 clusters were subsequently grouped into $k = 4$ and $k = 8$ superclusters to demonstrate changes in the chemofacies at various scales; these numbers were chosen based on reasonable splitting points in the dendrogram (see subsection 3.3.3).

3.3 RESULTS

3.3.1 μXRF Environmental Proxies

A total of 55-60 different elements were present in the data after batch analysis but this study focuses on a subset of high-concentration elements with high (> several hundred) total counts (cts) and good detectability using μXRF (Croudace et al., 2006; Gregory et al., 2019; Gabriel et al., 2022a). Visual analysis of the SJB core elemental data compared to the Itrax photograph showed that the total counts per second (cps) and coherent scatter (Mo coh) values dropped significantly at cracks in the core as well as at a some intervals (few centimetres) where the sensor lifted to avoid damage. These intervals of poor data, a total of 735 observations (0.368 m; 2.1%), were excluded from subsequent statistical analyses. For the Caineville samples, the acrylic reservoir dividers had significantly higher values of incoherent:coherent scatter relative to the sediment samples so these intervals were also removed from the analysis (Gregory et al., 2017).

Sediment Source and Composition

The relative changes in dominant sediment input, terrestrial vs marine, were shown with the Fe/Ca ratio, which is commonly used in palaeoenvironmental studies (Croudace and Rothwell, 2015). The Fe values had moderate to strong correlation to other siliciclastic elements, such as Ti ($R^2 = 0.7$), K ($R^2 = 0.62$), and Si ($R^2 = 0.63$), and a weak correlation to redox-sensitive elements (e.g., V, $R^2 = 0.29$) indicating that it mainly has a terrestrial source and has not been enriched due to authigenic processes (e.g., anoxia in the water/sediment). In addition to the overall composition, the relative grain-size changes were shown using the Zr/Rb ratio, which has commonly been used in palaeoenvironmental studies as a relative grain-size indicator (Dypvik and Harris, 2001; Wang et al., 2011; Hsiung et al., 2021) as Zr is typically contained in the heavier mineral zircon while Rb is contained in clay minerals, such as illite and micas. The relative weathering conditions (i.e., water energy) at the sediment-water interface were determined based on the relationship between Ti and K. In terms of mobility during weathering, Ti-bearing minerals, such as rutile, ilmenite, and titanomagnetite, are among the most stable and thus less susceptible to weathering compared to K, which is among the most mobile (Lisitzin, 1996), so variations in the Ti concentration of sediments have been shown to positively correlate with riverine runoff (e.g., Haug et al., 2003) and negatively correlate with transport distance (e.g., Chen et al., 2013). Finally, the Sr/Ca ratio was used as a proxy for aragonite presence and to distinguish shallower-water carbonate facies from deeper ones (Rothwell et al., 2006).

In addition to the lithologic composition, organic matter preservation and relative oxygenation were determined with the Cu/Ti and V/Cr ratios, respectively. Copper is commonly delivered to the sediments through adsorption onto organometallic ligands (Tribovillard et al., 2006; Rothwell and Croudace, 2015b) and can therefore represent the flux of marine organic matter (MOM) while V and Cr are the most easily reduced of the redox-sensitive transition metals making them useful for indicating even weakly reducing (i.e., suboxic) conditions (Cole et al., 2017) that may preserve the MOM. Since MOM is necessary for the formation of liquid hydrocarbons, identifying enriched intervals could help identify potential source rocks.

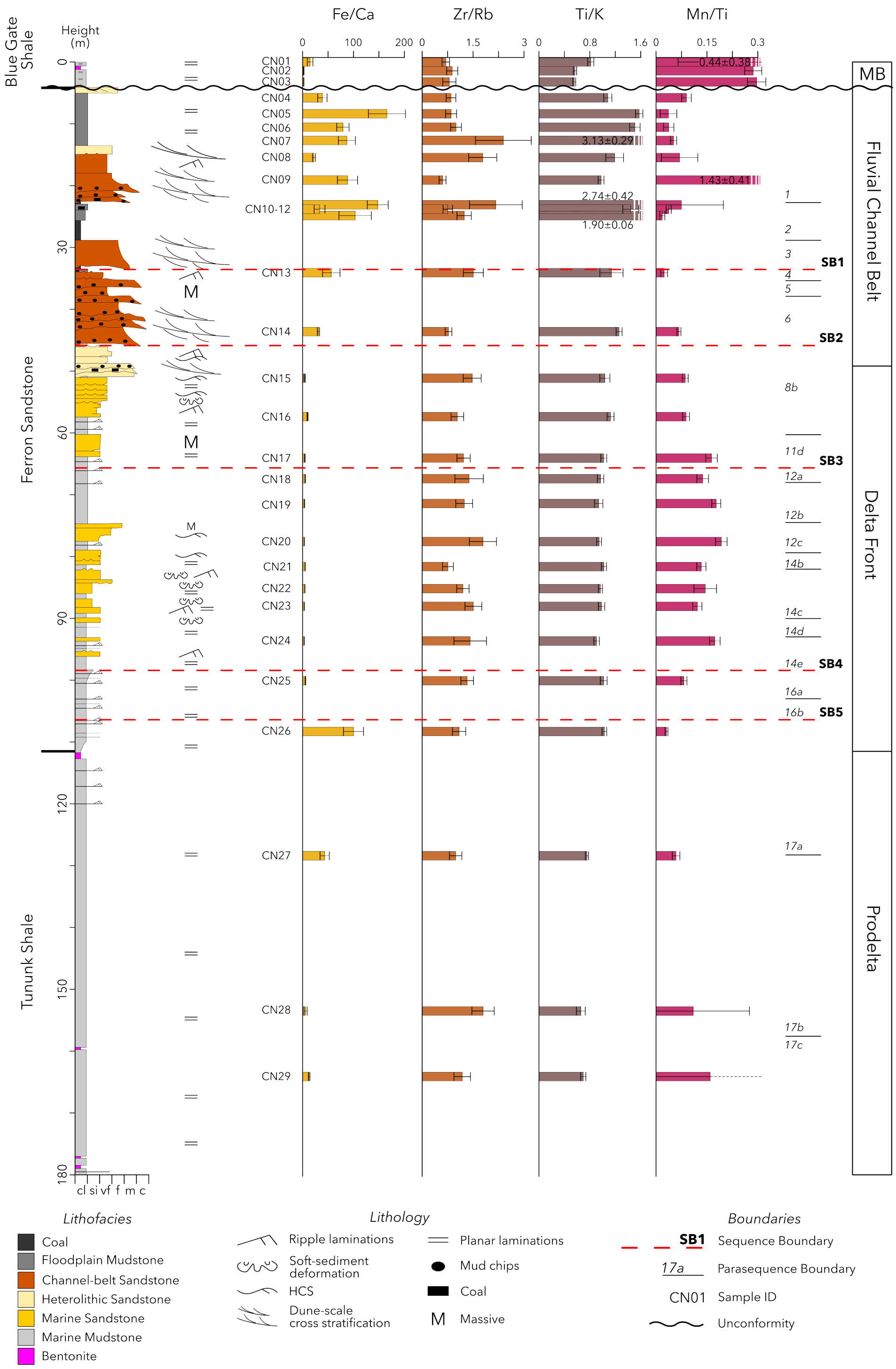

Figure 3.2: Measured section lithology and elemental data for the Caineville stratigraphic section. Sequence (SB) and parasequence boundaries (PS) were established by Zhu et al. (2012) based on regional lithostratigraphy.

3.3.2 Lithology

Caineville Outcrop

The Caineville section is 180 metres high and contains 19 parasequence (e.g., PS17c) and 5 sequence boundaries (e.g., SB1) from four depositional environments (Figure 3.2). A detailed description of the lithofacies and regional sequence-stratigraphic framework is beyond the scope of this research (readers are directed to Zhu et al. (2012)) but the general lithologic units and facies are as follows. The lowest lithologic unit is the Tununk Shale (>112 m), which is comprises prodeltaic marine mudstone, with sparse planar siltstone laminations at the base that transition up-section to rippled, very-fine lower sandstone laminations as the shoreline progrades. The Tununk Shale conformably transitions into the overlying Ferron Sandstone (3-112 m), which shows continued shoreline progradation as the basal prodelta mudstone transitions to delta-front sandstone (50-112 m) and finally to fluvial channel belt sandstone and floodplain mudstone (3-50 m). The Blue Gate Shale (0-3 m), which comprises proximal-mudbelt mudstones (Birgenheier et al., 2017; Gabriel et al., 2022a), unconformably overlies the floodplain mudstones of the upper Ferron Sandstone at 3 m; the hiatus between the two units is ~4 Ma, roughly spanning the Coniacian (Fielding, 2010).

SJB Core

The SJB Core is a continuous 17-metre long section (6898-6955 feet drilling depth) of mainly dark grey, homogenous mudstone (silt and clay) from the Upper Mancos C unit, although there were intervals of siltstone and very-fine sandstone interbedding. The core was originally logged by Jim Rine of Weatherford Laboratories, Houston, whose final report was provided along with the core. Four main lithofacies were identified in the core along with two unique-event units.

The most prevalent lithofacies in this core is structureless mudstone (LF1; ~62.8%), which is dark grey and is lacking in apparent stratification, though there are occasional millimetre-scale, planar lenses of fine silt, as well as several *Inoceramid* fragments, scattered throughout. Detrital matrix (i.e., clay minerals) comprises roughly 50% by volume of these sediments, based on thin section analysis by Weatherford Laboratories (J.Rine, *pers. comm.*), with quartz grains making up only ~2%. In the μXRF data, this facies has higher Fe/Ca values, relative to the median, indicating a more siliceous mudstone, with relatively stable conditions as seen by the median values in Zr/Rb as well as median values in the Ti/K ratio although this lithofacies had the lowest variance in Ti/K by an order of magnitude. The lack of features and stratification would suggest that this facies was deposited from settling of a fluid mud that was either delivered as a hyperpycnal plume from riverine input or resuspended in shallower water by wave or current energy and transported deeper into the basin.

The second most prevalent lithofacies was mudstone with siltstone laminae (silt-streaked mudstone; LF2), which comprises ~30.6% of the total core. This facies differs from LF1 by the increased number, and apparent grain size, of silt- and sandstone laminae, though these tend to be discontinuous over the width of the core. The laminae commonly show evidence of starved ripples, low-angle lamination, and millimetre-scale scour at the base, which indicates that they were deposited in the presence of bottom currents. Thin section analysis of the silt- and sandstone laminae showed they were mainly comprised of carbonate cement, foraminifer tests, and shell fragments that were too small to identify (J.Rine, *pers. comm.*). This facies is associated with the lowest Fe/Ca values, aside from the carbonate grainstone event bed at 6.5 m, indicating a more calcareous mudstone and while the Ti/K ratio is the lowest of any facies, the variance is significantly higher than in LF1 as a result of more variable energy conditions at the seabed.

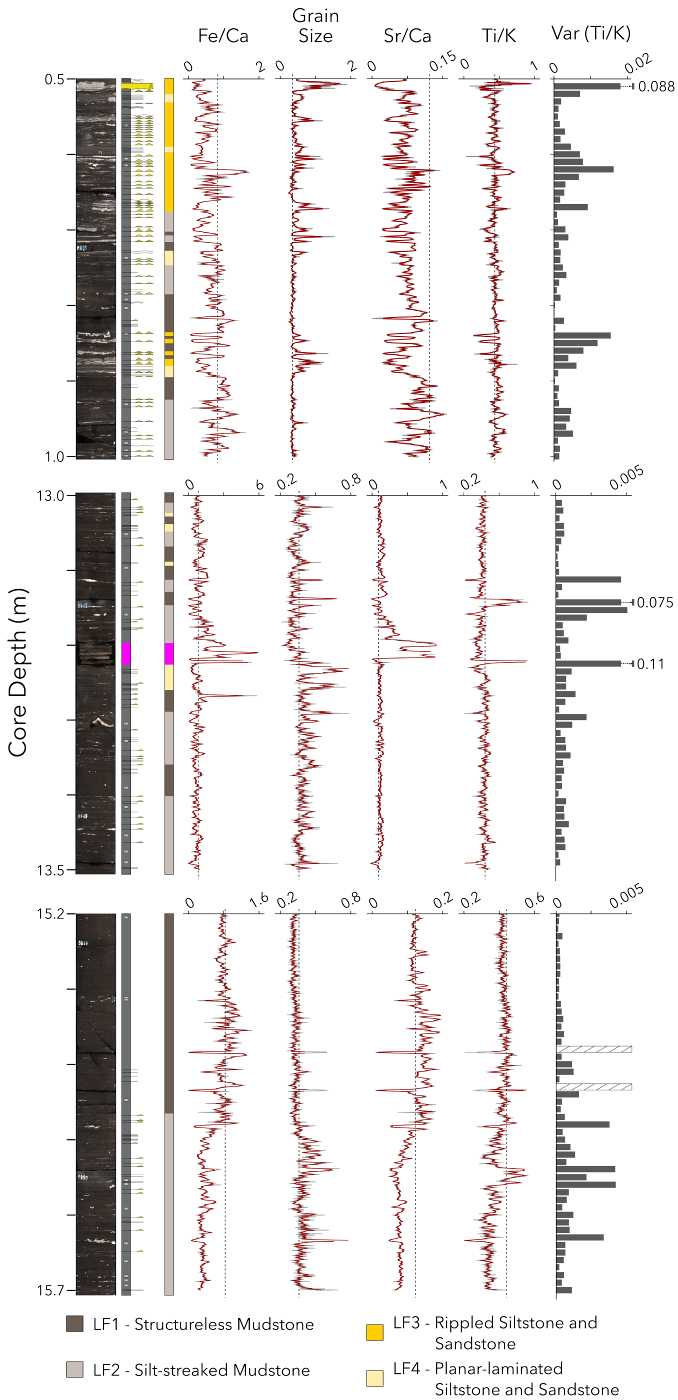

Figure 3.3: A comparison of the lithology, lithofacies, and elemental trends through three segments of the Mancos core. Values for the elements/ratios are in total counts. The bentonite, which was high in Ti and Zr, shows a sharp base but a more gradual decline above suggesting that after deposition, the tephra is being reworked and incorporated into the overlying sediments. Note the order of magnitude decrease in variance of Ti/K between LF1 (structureless mudstone) and the other lithofacies. Dashed lines represent the median values for the entire core for each proxy.

Lithofacies 3 (LF3) comprises $\sim$ 6.1% of the core and is characterised by siltstone to very-fine sandstone with nearly symmetrical convex-up ripples, a higher Ca content, relative to the median, higher Zr/Rb ratio, and generally higher variance in the Ti/K ratio, though the values tend to vary close to the median. As with the laminae in LF2, the silt- and sand-sized particles were carbonate-dominant, though in this lithofacies there was no carbonate cement and the shell fragments were large enough to identify (*Inoceramid*, pelecypod, brachiopod; J.Rine, *pers. comm.*). All of these proxies indicate that these sediments were deposited above storm-wave base in the highest energy conditions of any of the lithofacies, where they were continually reworked by wave action, probably from large storms, and bottom currents.

Finally, laminated siltstone (LF4) was the least prevalent ($\sim$0.4% of the core) and is characterised by planar-laminated siltstone to very-fine lower sandstone, with thin, millimetre scale laminae that were mostly planar and continuous across the width of the core. This type of lamination has been attributed to bottom currents where turbulent flow has been suppressed by high clay content in the water column directly above the seabed, so the laminae lack any wavy or inclined orientations (Plint, 2014). The carbonate content and Zr/Rb ratio are generally higher than median values in this lithofacies, indicating that the siltstone laminae are likely composed of biogenic material (e.g., foraminifera, radiolaria). Alternatively, winnowing of the clay fraction may have left voids surrounding the remaining silt-sized quartz grains that were subsequently filled in with carbonate cement growth (Cf. Beil et al., 2018; Yoon et al., 2019; Gabriel et al., 2022a). Both of these interpretations would indicate deposition in the mid to distal mudbelt near storm-wave base.

In addition to these four lithofacies, two 'event units' were also identified: a carbonate grainstone and a bentonite at depths of 6.75 m and 13.25 m, respectively. The grainstone unit is approximately 20 cm thick, with a high carbonate content (up to 50%; J.Rine, *pers. comm.*), though thin (centimetre-scale) siliciclastic mudstone interbeds are present throughout and they increase in thickness and frequency approaching the top of the bed, which is moderately bioturbated (BI = 2-3). The relative square-form shape of the μXRF elemental trends would suggest that the individual carbonate beds, which range from a few to several centimetres, were deposited rapidly and that there was minimal reworking post-deposition; even the structureless mudstone of LF1 showed continual higher frequency peaks in the elemental trends, albeit with much lower amplitude. The bentonite unit is approximately 2 cm thick and showed the highest values of K and Zr, which display a sharp basal contact with the underlying sediments but a more gradual upper contact, likely as a result of some incorporation of the tephra into the overlying muddy sediments.

3.3.3 Chemofacies

Caineville Outcrop

To establish the chemofacies for the depositional environments of the Caineville section, the mean and standard deviations were calculated using all of the intervals from that environment. The supratidal floodplain mudstone samples (CN04-CN07 and CN10-CN12) showed the lowest overall abundance of Ca ($\mu = 0.16$ x10^4; $\sigma = 0.12$ x10^4), high Fe ($\mu = 9.98$ x10^4; $\sigma = 2.61$ x10^4), and the highest Ti ($\mu = 6.03$ x10^3; $\sigma = 1.11$ x10^3) but lowest K ($\mu = 3.60$ x10^3; $\sigma = 1.31$ x10^3). Within the channel belt samples (CN08, CN09, CN13, CN14), the sediments have higher Ca ($\mu = 0.27$ x10^4; $\sigma = 0.16$ x10^4) and Fe ($\mu = 10.06$ x10^4; $\sigma = 4.0$ x10^4) values, as well as higher variances due to more variable conditions, but the variances in Ti and K significantly decreased ($\sigma = 0.76$ x10^3 and $\sigma = 0.64$ x10^3, respectively) as the higher and more-constant water energy is able to continuously mobilise the heavier Ti-bearing minerals as well as the clay minerals. The fully-marine delta front (samples CN15-CN26) is where a large volume of sediment is first deposited and subjected to nearly constant energy conditions, which in the case of the WIS is mainly from wave action, although fluvial, and likely some tidal, processes would also have had an influence. This environment has the highest Fe (μ = 10.59 x10^4; σ = 1.25 x10^4), an increase in Ca (μ = 2.41 x10^4; σ = 0.89 x10^4) over the fluvial environments, and an even abundance of Ti and K (μ = 4.75 x10^3 and μ = 4.79 x10^3, respectively); there is also a further drop in the variance in Ti and K, indicating the most consistent (i.e., average) conditions. Beyond the delta front, the overall terrestrial composition begins to decline, although the clay fraction continues to increase through the prodelta (μ_K = 6.64 x10^3; samples CN27-CN29) and into the proximal mudbelt (CN01-CN03), which has the highest K (μ = 7.77 x10^3) and where the siliciclastic fraction commonly exists as a fluid mud. The increase in clay, the lack of a hard substrate, as well as frequent influxes of fresh water from hyperpyncal plumes creating brackish (i.e., stressed) conditions, causes a decrease in marine productivity compared to the delta front, which can be seen in the lower Ca values (μ = 0.91 x10^4) with an increased variance (σ = 0.54 x10^4).

There were also differences in the relative oxygenation state between these environments, as seen in the V/Cr ratio. The lowest V/Cr, and therefore the highest oxygenation, occurs in the delta front (μ = 0.447; σ = 0.231), where the constant wave action keeps the waters well mixed. Moving landward, the V/Cr values increase in the channel belt (μ = 0.472; σ = 0.211) and further in the floodplain (μ = 0.513; σ = 0.228), where calm and even stagnant conditions may exist periodically, resulting in decreased mixing of the uppermost sediments. This is combined with a higher influx of terrestrial organic matter, which can outpace the aerobic activity of microorganisms and lead to reduced conditions. Basinward from the delta front, the V/Cr values increase much more rapidly and are highest, with respect to the Caineville environments, in the proximal mudbelt (μ = 0.659; σ = 0.483) as the energy at the seabed decreases with increasing water

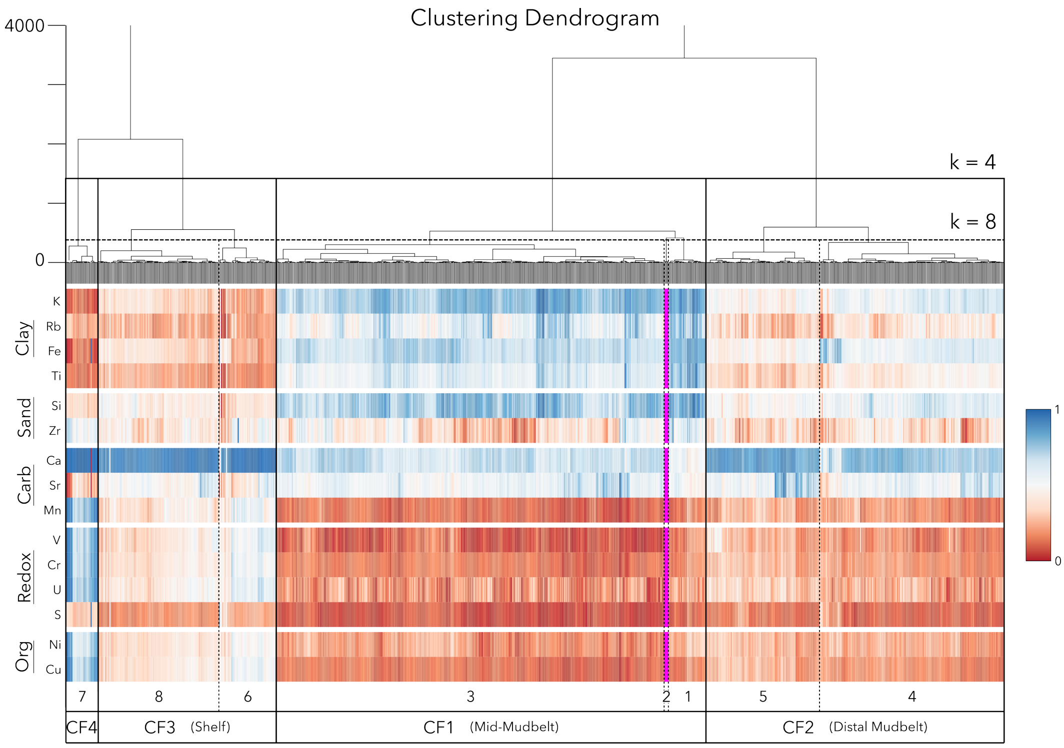

Figure 3.4: Hierarchical dendrogram (Ward's distance) from the Self-Organising Map showing elements re-scaled from 0 (red) to 1 (blue). The divisions for $k = 4$ (CF1-4)and $k = 8$ (1-8) are outlined and the bentonite cluster (2) is highlighted in magenta. The interpreted depositional environment for CF1-CF3 is written in brackets and matches the environments in Table 3.1 and Figure 3.5.

depth. There is also an increase in Cu/Ti ($\mu = 0.046$; $\sigma = 0.023$) in this zone suggesting a higher preservation of MOM. However, the higher variances in these proxies indicates that this environment is subject to significant shifts in oxygen conditions at the seabed due to mixing from storms or changes in freshwater input and organic matter flux to the sediments.

SJB Core

The cluster dendrogram for the SJB Core chemofacies, based on Ward's distance, is shown in Figure 3.4 along with heat logs of individual elements scaled to [0,1], using the equation $x - min(x)/\Delta(x)$. Due to the exceptionally high values of some elements in the bentonite, particularly K and Zr, these intervals were excluded from the scaling to better showcase the variability between the sediments. For this core, four superclusters were sufficient to accurately map the major units identified in the lithofacies (LF1-LF4; Figure 3.3). Overall, three of the superclusters show a trend of decreasing siliciclastic elements and increasing carbonates (Table 3.1), with the fourth being associated with the carbonate-rich beds (e.g., the grainstone unit at 6.75 m). Chemofacies 1 (CF1) had the highest concentration of siliciclastic elements, both clay (Fe, Ti, Rb, K) and sand (Si and Zr), and the lowest, albeit still moderate, concentration of Ca, indicating the highest input from terrigenous sediments of any of the chemofacies. Despite high siliciclastic input, including clay, the organophile (Ni and Cu) and redox-sensitive elements (V, Cr, U) are the lowest in this chemofacies so the influx of organic matter associated with the mud fraction was not high enough to overcome the available oxygen in the water column. Chemofacies 2 (CF2) decreases in the abundance of siliciclastic elements, particularly in the sand and Ti-bearing heavy mineral fractions, and increases in Ca content indicating a decrease in terrestrial influence as the depocentre moves further offshore. While still very low, there is also a slight increase in the abundance of organophile and redox-sensitive elements, suggesting lower oxygen and more preservation of organic matter in the sediments. This trend in elemental abundance continues into chemofacies 3(CF3), which shows the highest abundance of Ca and Mn of any chemofacies, aside from chemofacies 4, indicating that this facies was deposited the furthest from shoreline. The increased abundance of Ni and Cu suggest that there was an oxic and biologically productive water column, which increased the flux of MOM to the sediments, combined with dysoxic conditions in the sediment, as seen in the increased V, Cr, and U, which helped preserve the MOM.

Even with a cursory glance at the dendrogram, smaller clusters in one or more elements can be clearly seen dividing the four superclusters. At $k = 8$ superclusters, each of the three main chemofacies (CF1-CF3) were divided into two distinct groups, with CF4 remaining the same, and a third cluster was identified within CF1, which was associated with the bentonite (magenta band in Figure 3.4). Aside from the bentonite, CF1 was separated into a group with the highest siliciclastic, including Si and Zr, and lowest carbonate (*1*) and a group with lower siliciclastic, mainly Zr, and higher Ca and Sr (*3*), which may be indicating differences between times of increased fluvial runoff and relatively calmer periods with increased marine productivity; a similar division occurred in CF2. The distal chemofacies, CF3, had similar low siliciclastic content in both divisions and were instead differentiated based on higher and lower amounts of redox (V, Cr, U) and organophiles (Ni and Cu), indicating variability in the preservation of MOM.

3.4 DISCUSSION

3.4.1 Chemofacies of Depositional Environments

Comparison of the SJB Core chemofacies to the known depositional environments of the Caineville section, as well as the depositional models of Hart (2016) and Birgenheier et al. (2017), showed that the entire SJB core had a more distal depocentre (i.e., basinward of the prodelta) than the Caineville section, and the combination of the two, as well as additional Blue Gate Shale data from Gabriel et al. (2022a), contains a near-continual basinward trend from supra-/intertidal floodplain mudstone and channel-belt sandstones (upper Ferron - Caineville), through delta front sandstone and mudstone (lower Ferron - Caineville), the prodelta (Tununk - Caineville), the mudbelt (Blue Gate - Caineville; CF1 & CF2 - SJB core), and finally the sediment-starved shelf (CF3 - SJB core). Even though all of the samples were from the finer-grained fraction, there were still significant differences in their composition along a basinward transect, with the

Table 3.1: Mean (μ) and standard deviation (σ) of various environmental proxies. Bold and italicised numbers indicate the Depositional Environments with the highest and lowest values, respectively, for each proxy. The proximal mudbelt values also include Blue Gate μXRF data from Gabriel et al. (2022a). Values for Fe and Ca represent counts x10^4 and values for Ti and K represent kilo-counts.

Depositional Environment	Fe		Ca		Ti		K		Ti/K		Zr/Rb		V/Cr		Sr/Ca		Cu/Ti		Mn/Ti	
	μ	σ	μ	σ	μ	σ	μ	σ	μ	σ	μ	σ	μ	σ	μ	σ	μ	σ	μ	σ
CAINEVILLE																				
Floodplain	9.98	2.61	*0.16*	*0.12*	**6.03**	**1.11**	*3.60*	*1.31*	**1.9**	**0.72**	1.31	0.76	0.51	0.23	**1.30**	**0.71**	*0.03*	*0.02*	*0.05*	*0.05*
Channel	10.06	4.00	0.27	0.16	5.44	0.76	4.83	0.64	1.14	0.16	1.17	0.56	0.472	0.211	0.72	0.76	0.03	0.02	**0.39**	**0.63**
Delta Front	**10.59**	**1.25**	2.41	0.89	4.75	0.64	4.79	0.60	0.99	0.07	1.29	0.38	*0.447*	*0.231*	0.20	0.35	0.02	0.02	0.13	0.05
Prodelta	9.87	1.92	0.91	0.54	4.61	0.60	6.64	0.76	0.70	0.06	**1.34**	**0.43**	0.565	0.235	0.28	0.15	0.02	0.02	0.11	0.19
P. Mudbelt	8.04	2.02	4.84	1.29	4.36	1.09	**7.77**	**1.66**	0.56	0.08	0.72	0.34	0.659	0.483	0.10	0.05	0.05	0.02	0.17	0.21
SJB																				
CF1	7.49	0.92	7.49	0.95	3.13	0.39	6.76	0.50	0.46	0.05	*0.54*	*0.12*	1.08	0.36	0.14	0.02	0.06	0.02	0.16	0.03
CF2	7.05	1.18	10.39	1.62	2.53	0.35	5.83	0.63	0.43	0.04	0.65	0.19	1.22	0.46	0.12	0.02	0.06	0.03	0.20	0.04
CF3	*5.44*	*2.16*	**16.25**	**2.74**	*1.63*	*0.39*	4.26	0.87	*0.39*	*0.07*	0.97	1.02	**1.40**	**0.65**	*0.09*	*0.02*	**0.07**	**0.05**	0.30	0.15

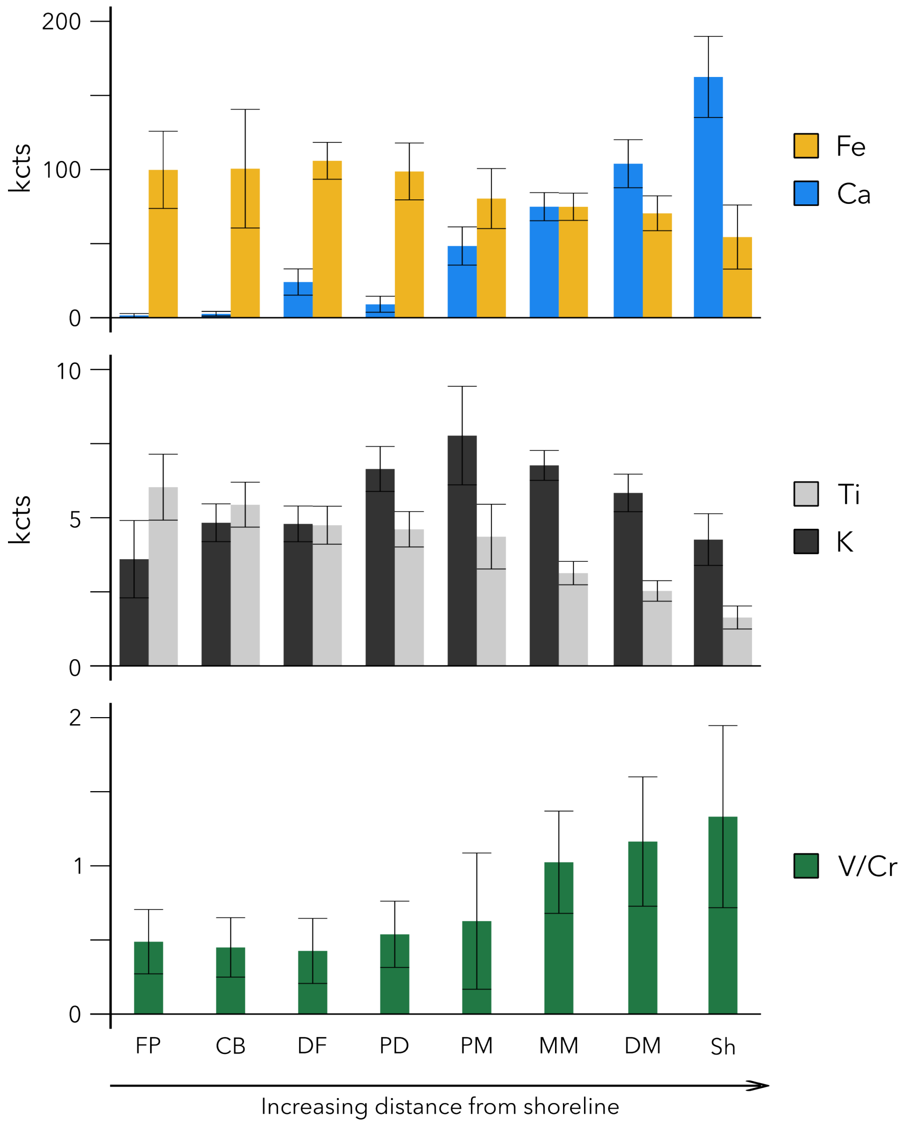

Figure 3.5: Comparison of the mean and standard deviation values for Fe, Ca, Ti, K, and V/Cr by depositional environment.

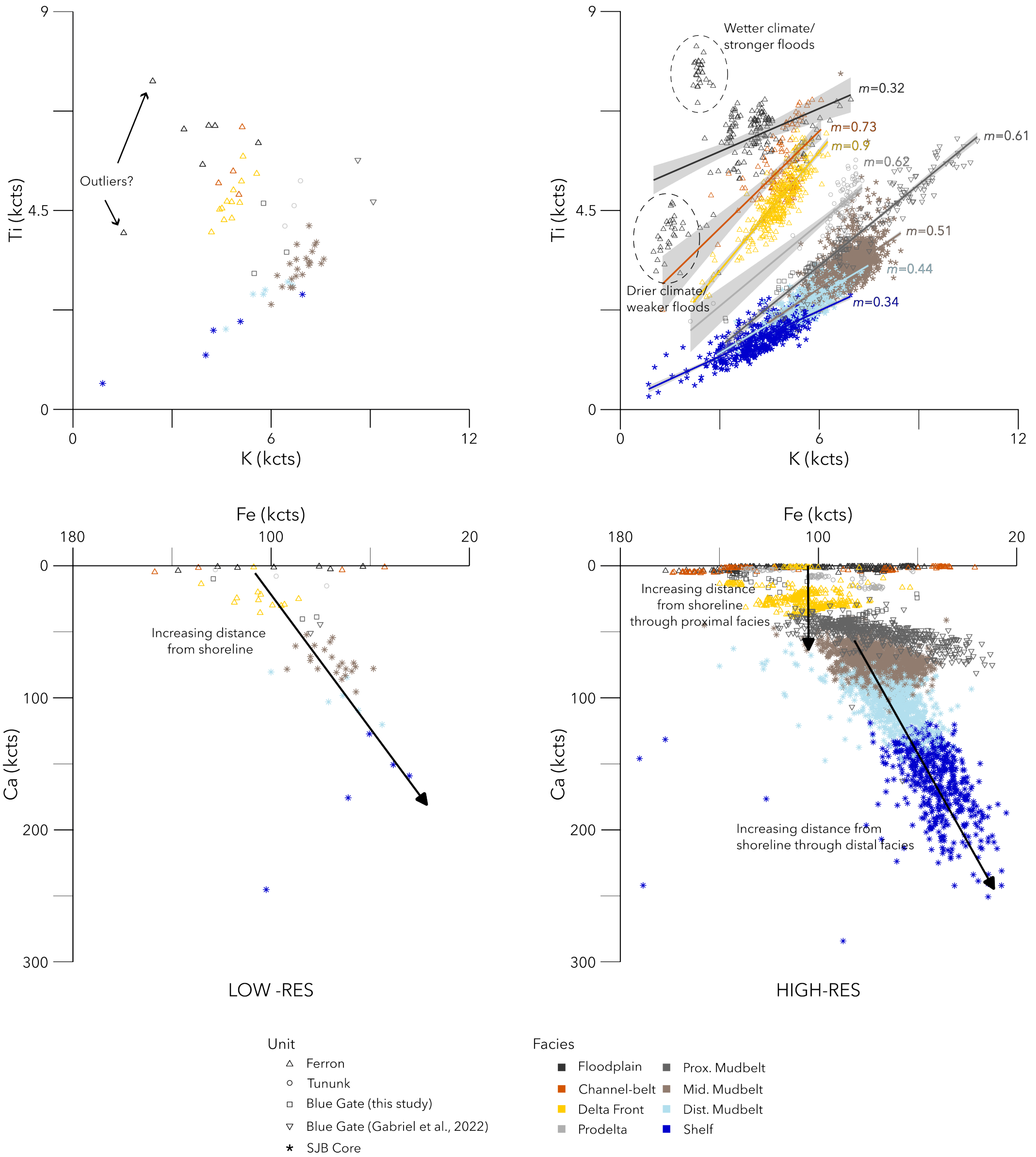

Figure 3.6: Cross plots showing the differences in Ca vs Fe and Ti vs K based on depositional facies. Low-Res plots use only the average values for each Caineville sample, two samples from the Gabriel et al. (2022a) Blue Gate, and 33 observations from the SJB core, representing 0.5 metre sampling. In the High-Res Ti vs K plot, the trendline and slope for each facies is given. The length of the trendline is related to the overall spread of the data and the decreasing slope away from the delta front indicates K is the more dominant control on siliciclastic variance in the lower energy environments. In the Fe vs Ca plot, the black arrows show the direction of increasing distance from shoreline; note the axes have been reversed to relate to water depth.

mean and standard deviations in Fe, Ca, Ti, K, and V/Cr effectively distinguishing each environment (Figure 3.5). The proxies Zr/Rb, Sr/Ca, Mn/Ti, and Cu/Ti were not as effective at distinguishing each environment but differences could be seen between the shallow areas and the deeper ones. Those proxies were better suited to investigating the chemostratigraphic changes through the core.

Fluvial Floodplain & Channel Belt

As expected, the channel-belt and floodplain deposits are almost entirely siliciclastic in their composition, with very low Ca values, although differences can be seen between the two environments (Figure 3.5). The floodplain chemofacies has the highest Ti and lowest K, on average, of any depositional environment but also the highest standard deviation relative to the mean in these elements. During times of increased flooding (e.g., storms), siliciclastic sediments comprised of both Ti- and K-bearing minerals would be deposited across the floodplain but as the flood wanes, the lower energy conditions on the floodplain would preferentially weather and transport the lighter K-bearing clay minerals. The scatterplot of Ti versus K shows that the data are separated into three groups, with one group being more abundant in Ti, a second having similar amounts of each element, and the last having lower amounts of both elements (Figure 3.6). These differences may be the result of variations in flood strength during wetter or drier periods or they might be the result of differences in the proximity of the sediments to the channel bank, where higher slopes would result in higher energy. The floodplain sediments also have a moderate V/Cr value resulting from some dysoxia due to organic-rich sediments that are seldom reworked to increase oxygenation. The channel-belt sediments had higher amounts of Fe and K but lower Ti and Ti/K resulting from the more-continuous energy conditions within the channel from fluvial activity. There was also an increase in Ca in the channel sediments, likely due to the erosion of older underlying marine sediments as the river cuts the channel belt but it could also indicate a more-direct connection to the marine environment if the channels are within the tidal backwater limit.

Shallow-Water Mudstone – Delta Front & Prodelta

The delta front is where fluvial and marine processes interact and is the location where a majority of the coarser-grained sand is deposited (Bhattacharya, 2006). Geochemically, this facies increased in both its overall carbonate content and variability, which indicates that the near-shore environment was subject to fluctuations in siliciclastic input (i.e., fluvial discharge) that would have impacted the productivity of the shallow-marine biota. Based on the microfossil (testate amoeba and foraminifera) assemblages, Turkistani et al. (2022) developed a salinity index for this Caineville section which shows highly variable conditions during the deposition of the Ferron-Notom delta-front sediments, from marine to brackish, as a result of changes in the amount of freshwater input. While there were fluctuations in the fluvial input, this environment seems to be balanced, on average, between input (fluvial) energy and output energy (from the reworking and transport due to marine processes), with equal amounts of Ti and K ($\mu_{Ti/K} = 0.993$, $m = 0.9$) and the lowest V/Cr (i.e., well-oxygenated; Table 3.1; Figure 3.6). It should be noted that due to the nature of the elemental data collected from a μXRF core scanner, these slope values in Ti vs K cannot be directly compared to elemental data collected from traditional techniques (e.g., ICP-OES), where the typical slope between Ti and K for bulk continental crust is around 0.49 (McLennan, 2001). Nevertheless, the relative slope change in the μXRF data between environments provides valuable information regarding the trends within and between them.

The prodelta is where fine-grained sediments, silt and clay, begin to accumulate in large amounts through hyperpyncal and wave-enhanced gravity flows (Bhattacharya, 2006; Walsh and Nittrouer, 2009). These sediments typically have a high water content and exist as fluid muds (nepheloid layers) on the seafloor with abundant suspended sediment (Bhattacharya, 2006; Hart, 2016) and tend to be deposited in relatively rapid events (e.g., hyperpycnal and sediment-gravity flows), resulting in highly variable bioturbation rates (MacEachern and Bann, 2020). As a result, the chemofacies of the prodelta has higher K values, with a continued decrease in Ti and a significant decrease in Ca content compared to the more productive delta front. Oxygen conditions in the sediments are also decreasing as the water depth and distance from shoreline increases. The slope in Ti vs K also decreases in the prodelta as the more-mobile clay minerals become the dominant source of siliciclastic variability in the lower energy environments; this decrease in slope continues through the remainder of the depositional environments.

Deep-Water Mudstone – Mudbelt & Shelf

The prodelta sediments are still mainly sourced from their associated delta but due to the high mobility of muds in the marine realm (Plint, 2014; Macquaker et al., 2010; Schieber et al., 2007), the sediments in the mudbelt may be transported 100s of kilometres from their original source and so can accumulate even in the absence of a local fluvial source (Figure 3.7). The WIS is interpreted to be mainly wave-dominated and so the sediments of the mudbelt may have been concentrated in more localised areas that migrated across the basin with longshore drift (Marine-dispersal-dominant (MDD) system; Walsh and Nittrouer, 2009). The chemofacies of the proximal mudbelt is defined by the highest clay content (K), but an overall decrease in siliciclastic content, and an increase in variability in these proxies, which may be reflecting changes in the locus of sedimentation on the mudbelt. In the more distal parts of the mudbelt, at or below SWB, the fine-grained sediments generally exist as a fluid mud with high suspended sediment concentration that likely acted to suppress the water energy from bottom currents as the standard deviation in most siliciclastic elements is low. As the total siliciclastic content decreases even further into the sediment-starved shelf, bottom currents are able to rework any remaining sediments, winnowing the clays and creating silt-sized ripples of skeletal carbonate material from foraminifera, coccolithophores, and shell micro-fragments. Even though Ti/K is the lowest in this environment, there is an increase in the standard deviation, particularly in K, as a result of intermittent settling and remobilisation of siliceous clays.

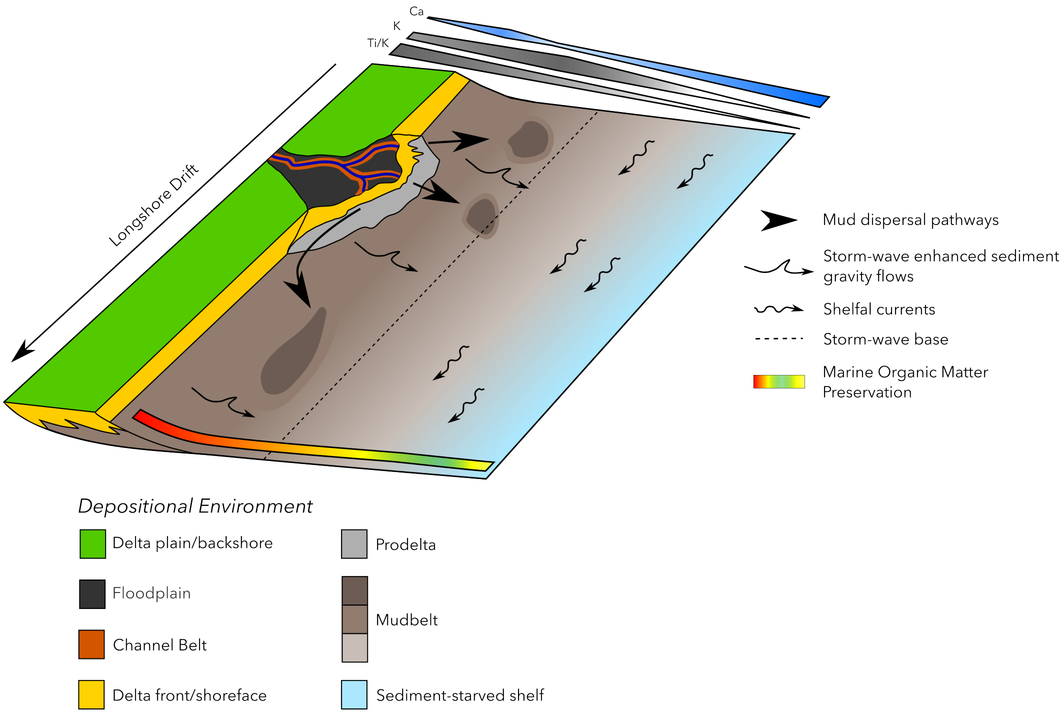

Figure 3.7: A conceptual model of depositional environments in an epicontinental sea with a wave-dominated, siliciclastic shoreline. Fine-grained sediments (silt and clay) are transported off- and along-shore by longshore drift, wave-enhanced sediment gravity flows, and bottom currents and accumulate in relatively local deposits (Marine-dispersal-dominant (MDD) system; Walsh and Nittrouer, 2009). Adapted from Walsh and Nittrouer (2009); Bhattacharya (2010); Hart (2016); Birgenheier et al. (2017).

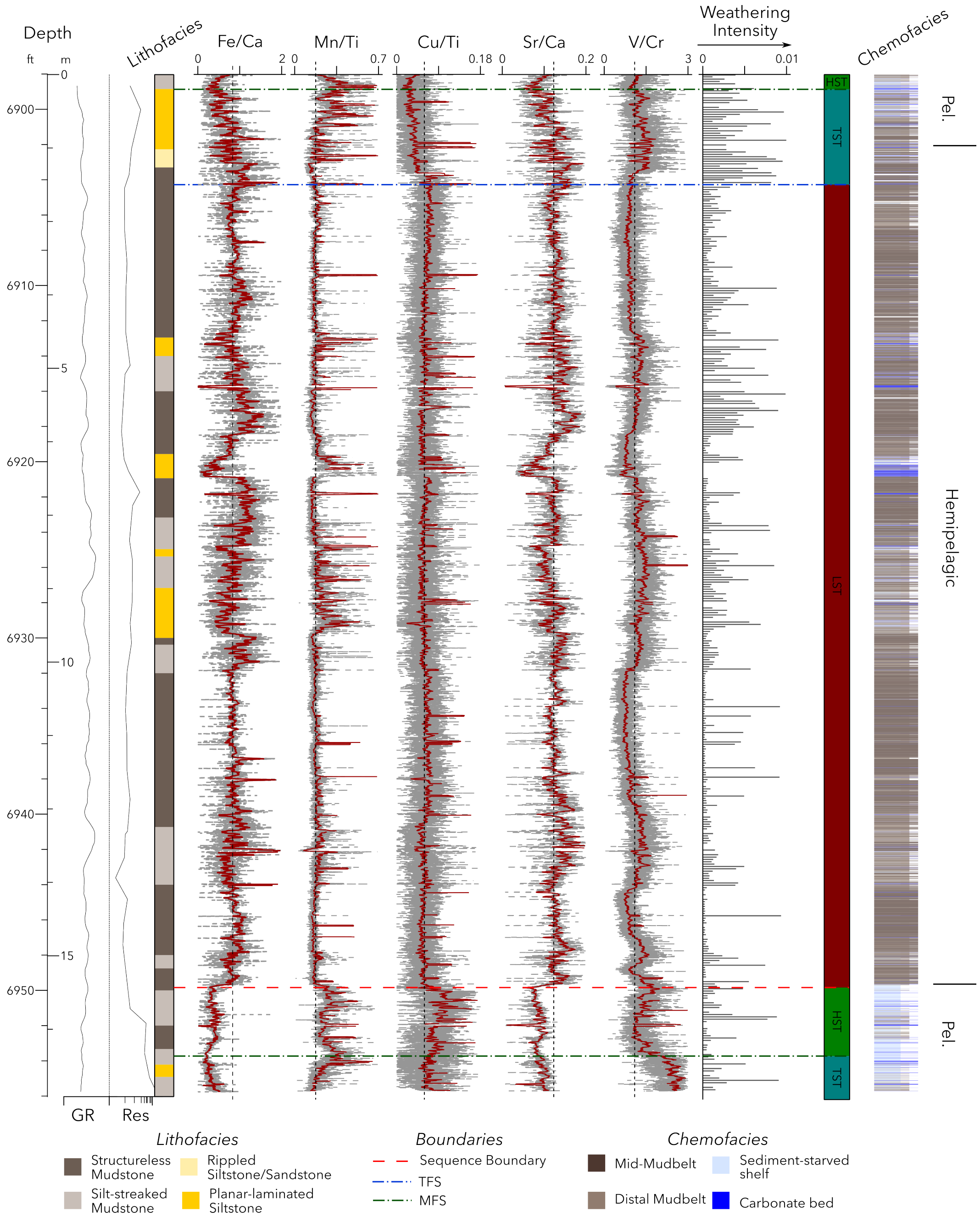

Figure 3.8: Chemostratigraphy and chemofacies changes in the SJB Core compared to the lithology and well-log data. The systems tracts and depositional environments on the right can only be established using the high-resolution μXRF elemental data, combined with the lithology.

3.4.2 Deposition of the SJB Core

The chemofacies, along with the chemostratigraphic variations in Mn/Ti, Sr/Ca and Cu/Ti, show significantly more variation than the well-log data and can be used to establish candidate flooding surfaces and systems tracts (Figure 3.8). The base of the core, up to 15.5 m, is mainly comprised of calcareous mudstone from the sediment-starved shelf (CF 3) and shows transgressive systems tract (TST) up to a flooding surface at ∼17 m, identified by a minimum in terrestrial input (Fe/Ca) and a maximum in Mn/Ti (maximum flooding surface; Corbin et al., 2000; De Rafélis et al., 2001; Olde et al., 2015). Above the maximum flooding surface, the highstand systems tract (HST) is defined by increasing terrestrial input and decreasing Mn/Ti, which shows a minimum at sequence boundaries, although the sediments are still being deposited in the distal mudbelt (CF 2) to shelf environments. There is a rapid shift above 15.5 m to significantly more siliceous mudstone of the mid-mudbelt (CF 1), which at higher scale occurs over ∼0.1 m and may be the correlative conformity associated with a near-shore sequence boundary from relative sea-level fall (forced regression), which is further supported by the minimum values in Mn/Ti. Alternatively, this signature may be the result of lateral movement of muddy sediment across the mudbelt and not due to a change in sea level. There is also a sharp decrease in Cu/Ti and V/Cr across this transition indicating a lower preservation of MOM due to increased oxygen in the sediments (see Figure 3.7). Above 15.5 m, the sediments are more siliceous and are deposited in the mid-mudbelt, near or below SWB, as part of a potential lowstand systems tract (LST). While overall the chemostratigraphy is relatively constant through the LST (1.5-15.5 m) and is mainly part of the mid-mudbelt chemofacies (CF 2), the interval from 4-9 metres is more variable. Above 1.5 m, the terrestrial input starts to decrease again, along with increasing Mn/Ti and V/Cr, and the chemofacies transition to more distal mudbelt and shelf environments, potentially indicating the start of the next TST.

This framework is not identifiable at all in the well-log data, which are mostly unchanging through this interval, and while a traditional geochemical study may have identified some variation downcore, the lower resolution would be unable to accurately identify the centimetre-scale transitions between the systems tracts. Furthermore, without the chemofacies, the lithologic analysis of this section may misinterpret the sequence-boundary correlative conformity as a flooding surface. The base of the core contains coarser-grained, starved-ripple laminae, some of which are a few millimetres thick, that transition upward to dark-grey, structureless mudstone, which would generally be interpreted as a marine transgression (i.e., flooding surface) in near-shore siliciclastic sediments. The chemofacies show that the environment actually shifts from a pelagic to a hemipelagic zone and therefore represents a shallower depocentre.

3.4.3 Shallow- vs Deep-Water Mudstone

As recent research has shown, fine-grained sediments (silt and clay) can be deposited in wide range of water depths and energy conditions (Plint et al., 2012; Plint, 2014; Schieber et al., 2013; Schieber, 2016) and that using lithology or stratigraphy alone can result in ambiguous interpretations between shallow- and deep-water mudstones (Petty, 2022). In deeper, calcareous sediments, the guidelines for interpreting the lithology are not the same as for near-shore siliciclastic sediments. In proximal settings, the transition from laminated or thinly-bedded units to overlying structureless mudstone is interpreted as a flooding surface due to a relative rise in sea level (transgression). However, in distal hemipelagic to pelagic environments this relationship is somewhat reversed, with the deeper sediment-starved shelf being defined by mudstone with thin, starved-ripple laminations of silt-sized grains that are being reworked mainly by shore-normal bottom currents, while the shallower distal mudbelt is mostly structureless mudstone settling out of a fluid mud where the concentration of suspended sediment is probably too high to be reworked by the lower-energy bottom currents. Therefore, the transition to structureless mudstone in this environment actually represents a shallower/more proximal depocentre as a result of a relative sea-level fall.

The μXRF data showed that shallow-water sediments (delta front, prodelta) have higher Ti/K values due to closer proximity to the fluvial source but the relationship between the two elements is closer to equilibrium, as indicated by the higher slope values, suggesting more-equal input and output energies. The deep-water muds, beyond the prodelta, have lower Ti/K values as the heavier Ti-bearing minerals settle out faster than the K-bearing clays as well as lower slopes due to the more-mobile clays accounting for the majority of the variation. In the mid- to distal mudbelt, suspended sediment concentration is high enough to suppress the energy of the bottom currents and the siliciclastic variation is lower but as that concentration decreases basinward into the sediment-starved shelf, the sediments are exposed to those currents and the siliciclastic variation increases. While the average Fe values only slightly decrease beyond the prodelta, the Ca values increase rapidly as the sediments become more calcareous. The deep-water mudstones also have higher values and variations in the V/Cr ratio, indicating lower overall oxygen conditions that are still quite variable.

3.5 CONCLUSION

The high-resolution elemental data obtained with an Itrax μXRF core scanner were able to provide detailed chemofacies descriptions of the depositional environments of the Western Interior Seaway. The volume of data obtained from this method allows for the analysis of elemental variability at a scale not possible with traditional techniques. In addition to showing the relationship between different elements, the μXRF data showed the variance in each element within the different environments. The delta front had the most consistent conditions based on the lowest standard deviation with respect to the mean in Fe and Ca and nearly equal values and standard deviations of Ti and K. Moving landward or seaward resulted not only in changes in data variance, but which proxy was controlling it. Moving landward, the variance in shoreline proximity indicators is more controlled by Fe while basinward it is controlled by Ca; in both directions, clay minerals (K) become the more dominant control on variations in weathering intensity. To the best of our knowledge, this is the first research to document this geochemical characteristic of different depositional environments of ancient epicontinental seaways. By defining these slope values, they can provide a reference point for all μXRF core scanning studies since the nature of the data do not allow them to be directly compared to traditional techniques (e.g., ICP-OES). These chemofacies and chemostratigraphic descriptions will provide a reference point for future studies of marine sediments from epicontinental seas and allow for the rapid classification of sediments with respect to their depositional environment and proximity to shoreline, as well the accurate identification of significant surfaces, which will lead to more robust models of basin evolution due to fluctuating sea level and climate.

The μXRF elemental data can be collected much faster than lamina-scale lithologic analysis ($\sim$34,000 data points in $<$ 7 days) and were more effective at showcasing the heterogeneities in the mudstone than traditional methods. Hierarchical clustering of the μXRF data using a Self-Organising Map was an effective way to rapidly cluster the intervals into chemofacies that could be investigated at a variety of scales with even a cursory glance. The more superclusters that are created, the more localised the variation would be. By applying this technique to other cores from within a basin, similar chemofacies could be established that would allow for more accurate correlations.

Chapter 4.

Mapping marine transgressive-regressive depositional cycles from the Western Interior Seaway of North America using high-resolution (500 μm) chemostratigraphy of the Upper Cretaceous Mancos Shale

This chapter has been prepared with the intention of submitting to the journal "Palaeogeography, Palaeoclimatology, Palaeoecology"

4.1 Introduction

The sedimentary deposits of epicontinental seaways, which have frequently occupied extensive areas of the continents during periods of sea-level highstands, provide valuable information about how the climate system operates in global greenhouse conditions. Due to their relative flatness and shallow depths, the sedimentary sequences from these basins can be correlated over distances at least an order of magnitude greater than modern continental shelf deposits (Schieber, 2016), providing much more information about the scope (e.g., local, regional, global) of environmental changes, including *eurybatic* (relative sea-level; Haq, 2014) shifts. Sequence stratigraphy greatly enhanced our understanding of, and ability to reconstruct, ancient epicontinental marine basins. Traditional lithostratigraphy simply grouped units of similar lithology (e.g., sand vs mud) and used arbitrary vertical cutoffs as the boundary between lithostratigraphic units, with little consideration being given to the lateral continuity of the different groups, units, or members (e.g., Wheeler and Mallory, 1953, 1956). Conversely, sequence stratigraphy takes into account the offshore progression of sedimentary facies, from fluvial to shallow marine to deep basin, and associates them as a single, genetically-related conformable unit, or sequence, that is bounded by an unconformity surface (van Wagoner et al., 1990; Bhattacharya, 2011). The original cratonic-scale sequences from the interior of North America were described from outcrop based on gross lithology (quartz sand, shale, carbonate) and separated by six laterally extensive unconformities that could be mapped over thousands of kilometres (Sloss, 1963). These sequences, which span the latest Precambrian to the present, were on the order of 10^2-10^3 metres thick and represented time scales of 10^5-10^7 years, although more localized unconformities could be observed in numerous locations subdividing these sequences. More recently, higher-resolution techniques such as seismic stratigraphy and detailed lithologic analysis have shown that these early sequences (now generally recognised as ‘supersequences’; Krapez, 1996; Catuneanu, 2019) are comprised of several higher-order conformable successions (Sloss, 1988; van Wagoner et al., 1990). There are no set spatial or temporal ranges associated with each order and the upper limit on the number of orders is mainly a function of data resolution (Catuneanu, 2019). In areas with extensive and well-preserved outcrops, such as those associated with the Cretaceous Western Interior Seaway (WIS) of North America, studies using detailed (sub-metre scale) lithologic analysis of coastal and near-shore sandstone facies have developed sequence-stratigraphic frameworks of shoreline trajectories showing higher-order cycles operating over 1-10 metres on time scales of 10^4-10^5 years (Zhu et al., 2012; Lin et al., 2019). As these higher-order cycles tend to be basinal, or even sub-basinal, in extent, identifying them is important to creating basin-specific sequence-stratigraphic frameworks that demonstrate climate variability at a more local scale.

Mudstone facies on the other hand have poor preservation potential in outcrop and the relative homogeneity in their composition and texture make them notoriously difficult to map, even in core (Dypvik and Harris, 2001; Baumgardner and Rowe, 2017). However, since mudstones occupy a much larger area of the basin (10s to 100s of km wide in epicontinental seaways; Hart, 2016) and often retain a more complete record than sandier facies, including them in sequence-stratigraphic frameworks is crucial to fully reconstructing the basin evolution. Typically these units are mapped in the subsurface based on seismic and well-log data (gamma radiation, spontaneous potential, resistivity) but these methods lack the resolution to accurately define cycles operating at submetre-scale, which can lead to ambiguous correlations (Pearce et al., 1999; Turner et al., 2016). These limitations have led to the development of basin cross-sections with thick, largely undifferentiated muddy successions (Figure 4.1; see also Nummedal and Molenaar, 1995; Molenaar et al., 2001; Ridgley et al., 2013) since they cannot be reliably correlated with the higher-resolution cycles established in near-shore environments (North et al., 2005).

Even where core has been collected, the subtle variations in lithology and texture make lithologic analysis a very time-consuming procedure, often requiring petrographic thin sections and X-ray diffraction (XRD) to observe the sedimentary structures and mineralogic composition (Yoon et al., 2019).

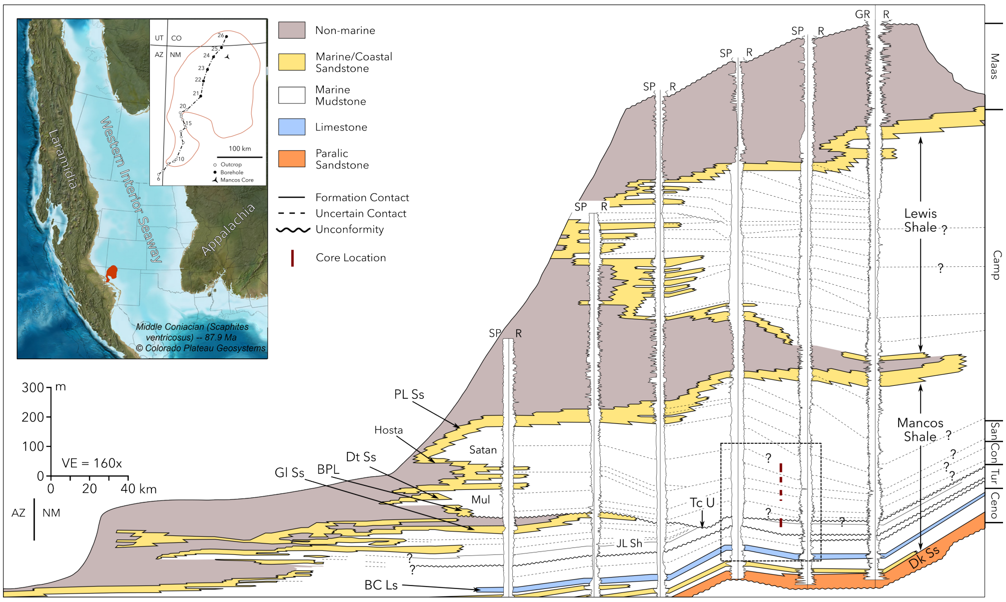

Figure 4.1: Stratigraphic cross section (dip-oriented) of the San Juan Basin from eastern-central Arizona through northwestern New Mexico based on measured outcrop (locations 6-20) and well-log data (locations 21-26; SP - spontaneous potential, R - resistivity, GR - gamma ray) adapted from Molenaar et al. (2001). The dashed surfaces and the (?) are taken directly from Molenaar et al. (2001) and represent uncertainty in the location/continuity of a surface. Dk Ss – Dakota Sandstone; BC Ls – Bridge Creek Limestone (also referred to as Greenhorn Limestone (Broadhead, 2021)); JL Sh – Juana Lopez shale; Tc U – Tocito unconformity (also referred to as the Niobrara unconformity (Broadhead, 2021)); Gl Ss – Gallup Sandstone; BPL – Borrego Pass Lentil; Dt Ss – Dalton Sandstone; PL Ss – Point Lookout Sandstone; Mul – Mulatto Tongue, Satan – Satan Tongue, both of the Mancos Shale. Dotted box represents area denoted in Figure 4.2. INSET: The Western Interior Seaway during the Middle Coniacian with the locations of the San Juan Basin, the USGS D-D' cross-section line, and the well location for this study (Well ID: San Juan 28-6 Ut 148M). Basemap from Colorado Plateau Geosystems (www.deeptimemaps.com).

4.1.1 Chemofacies & Chemostratigraphy

Variations in the elemental abundances of mudstone units can provide much more information about their depositional environment, mainly because of the number of proxies that can be used, which is > 200 when various elemental ratios are included (Craigie, 2018), compared to the 2-3 proxies typically measured by well-log techniques. Establishing the chemostratigraphy, which maps the downcore variations in elemental abundances, can be used to identify shoreline trajectories and significant surfaces based on the changes in siliciclastic input (e.g., Pearce et al., 1999; De Rafélis et al., 2001; Algeo et al., 2004; Olde et al., 2015; Turner et al., 2016) while the chemofacies, which describe the geochemical signature of each observation, can be used to classify the sediments and group them according to their depositional environment (e.g., delta front, prodelta, mudbelt Hart, 2016; Birgenheier et al., 2017; Gabriel et al., 2022b).

A number of studies on mudstones have investigated the correlation of chemostratigraphy to sequence stratigraphy. De Rafélis et al. (2001) and Jarvis et al. (2001) used the geochemistry of hemipelagic and pelagic mudstones to establish criteria for determining systems tracts and sea-level change and showed that in addition to the trends in siliciclastic input (Si, Ti, and Zr), Mn was also well-correlated with the systems tracts showing minimum values at sequence boundaries (3^{rd} order) and through the lowstand systems tract (LST), which increase through the transgressive systems tract (TST) to the maximum flooding surface (MFS) and then decline again through the highstand systems tract (HST) to the sequence boundary. Olde et al. (2015) examined a 405-m core of hemipelagic sediments from the Upper Cretaceous Bohemian Basin (Czech Republic) and were able to identify major marine trangressions at 0.4-1 Ma cycles based on variations in Ti/Al, Si/Al, Zr/Al, and Mn. Major regressive cycles (1-2 Ma) were defined by long-term highs in Ti/Al, Si/Al, and Zr/Al with an associated low in Mn. At a smaller scale, sharp-based increases in Ti/Al followed by more gradual declines were associated with transgressive surfaces where finer-grained clays are more easily eroded during the initial marine transgression before overall siliciclastic content decreases; these cycles were operating at ∼0.4 Ma frequency. However, the lower sampling resolution of these studies (∼1-2 m intervals), combined with lower sedimentation rates in hemipelagic and pelagic settings, means that higher-order cycles at 100 ka frequency or less are not reliably detectable (Olde et al., 2015) and therefore correlating them with high-resolution sequence-stratigraphic frameworks of proximal environments (e.g., Lin et al., 2019) is difficult.

4.1.2 μXRF Core Scanning

Recent technological advances in core scanners utilising energy-dispersive X-ray fluorescence (ED-XRF), such as the Itrax Core Scanner (Cox Systems, Sweden), have allowed for the collection of elemental data from sediment cores at sampling resolutions as low as 100 μm cheaper and faster than traditional techniques; these data are typically referred to as μXRF. Gabriel et al. (2022a) used both ICP-OES and μXRF elemental data, at 2 cm and 0.2 mm sampling resolution, respectively, to describe a short (28.5 cm) section of Mancos Shale from the Uinta Basin, Utah. The 15 samples collected for ICP-OES, each of which homogenised 2-3 mm, required approximately 3 weeks to collect, process, and analyse and cost ∼\$1700 CAD. In contrast, the μXRF analysis, which only took 6 hours and cost less than \$200 CAD, provided 1425 data points, each of which 'homogenised' only 100 μm (X-ray beam width); that is, there were 10-15 μXRF data points *within* each ICP-OES sample. This allowed the researchers identify sharp-based transitions in the lithology occurring over a few millimetres that were associated with short-lived sediment gravity flows induced by wave and current action. Gabriel et al. (2022b) provided a detailed chemofacies description of sedimentary rocks from various coastal and marine environments of the WIS using Itrax μXRF elemental data, showing not only the average values of different proxies in these environments, but also the variance in them. The relationship between Ti, which is less mobile in the environment (Lisitzin, 1996), and K was particularly useful at distinguishing between the various zones. Titanium showed a continual decrease moving offshore, as siliciclastic input decreases, but K, which is typically associated with clay minerals weathered from aluminosilicates and feldspars, increased from the intertidal and shoreline environments to the prodelta and mudbelt, where the majority of siliceous mud is deposited, and then decreased into the calcareous mud of the pelagic zone. These environments could be further distinguished by the slope in Ti vs K, which was the highest ($m = 0.9$) in the delta front as a result of relatively continuous input and reworking energies, and decreased in both directions away from the delta front as lower, but in areas more variable, energy conditions preferentially weathered the more-mobile K-bearing minerals (see Figure 6 in Gabriel et al., 2022b).

This current study builds on the previous chemofacies research and attempts to identify the chemostratigraphic signature of different depositional cycles and surfaces, which can then be correlated with the sequence-stratigraphic framework from near-shore environments (e.g., Sixsmith et al., 2008; Lin et al., 2019). Using high-resolution (0.5 mm sampling interval) elemental data obtained from an Itrax μXRF core scanner, this research will establish chemostratigraphic flooding surfaces and chemofacies in a muddy shelf deposit, the Mancos Shale, from the Western Interior Seaway (WIS) of North America in order to identify transgressive-regressive (T-R) depositional cycles that can be correlated with near-shore facies. Additionally, these high-resolution data will allow us to characterise the elemental signature of different systems tracts and flooding surfaces, something that has been lacking from the literature (LaGrange et al., 2020). While other studies have used ED-XRF to analyse the chemostratigraphy of mudrock and establish depositional cycles (Turner et al., 2016; Beil et al., 2018; Ma et al., 2014), to the best of our knowledge this is the highest-resolution chemostratigraphic study ever conducted on marine mudstone deposits from an epicontinental seaway.

4.2 Geologic Setting

The Mancos Shale is a distal muddy marine deposit that formed in the WIS during the Upper Cretaceous (Cenomanian - mid-Campanian; Figure 4.1). The period between 97 and 91 Ma (Cenomanian to late Turonian) has been shown to be the warmest interval in the past 115 Ma with tropical sea-surface temperatures >35 °C, which was followed by an overall cooling trend to the present, likely as a result of increased connection and water mixing between the north and south Atlantic (Friedrich et al., 2012). The WIS, which at its maximum extent connected the northern Boreal Ocean (Arctic Ocean) to the Tethys Sea (Gulf of Mexico) and was ~1500 km wide, occupied a retroarc foreland basin that formed as a result of the westward migration of the North American Plate due to rapid spreading of the Atlantic mid-ocean ridge starting in the Middle Jurassic (Miall et al., 2008); other contemporary epicontinental marine basins include the Bohemian Basin (eastern Europe; Olde et al., 2015), the Tarfaya Basin (Morocco; Beil et al., 2018), and the Levant Basin (Egypt; Baioumy and Lehmann, 2017). Uplift and erosion of the Sevier orogenic belt along the western continental margin caused the deposition of several sandy deposits in the near-shore environments (e.g., beaches, barrier islands, deltas) that intertongue with the finer-grained sediments (silt and clay) of the Mancos Shale moving to the northeast. Subsequent structural deformation during the Laramide orogeny (late Upper Cretaceous to Palaeogene) resulted in the formation of several sub-basins, including the San Juan Basin of New Mexico, which helped to preserve the Upper Cretaceous strata (Broadhead, 2015, 2021). High-resolution sequence stratigraphy of Upper Cretaceous deltaic complexes of the WIS, such as the Gallup and Ferron Sandstones, have shown marine transgressive-regressive cycles at several Milankovitch-scale frequencies, with sequences, parasequence sets, and parasequences operating on 100 ka, 46.2 ka, and

19.7 ka, respectively (Zhu et al., 2012; Lin et al., 2019). The parasequence sets of Lin et al. (2019) show shoreline advance and retreat of 60 km and 48 km, respectively, which roughly equate to relative sea-level changes of 34-38 m. The scale and frequency of these shifts, as well as similar data from the tropical Atlantic, suggests a glacio-eustatic control on sea-level fluctuations caused by Antarctic ice caps that have been estimated at ∼5-10 x10^6 km^3(Miller et al., 2003; Bornemann et al., 2008).

The Mancos Shale is informally divided into two main units, the upper and lower Mancos, which are separated by the end-Turonian Tocito unconformity (see page 86); the Tocito has also been referred to as the basal Niobrara unconformity (e.g., Ridgley et al., 2013; Broadhead, 2015). The lower Mancos overlies and intertongues with the paralic Dakota Sandstone as a dark-grey, marine shale (Graneros Member) which gradationally transitions upward to more calcareous-rich shales in the Greenhorn (Bridge Creek) Limestone Member and then back to darker, thin-bedded shales through the Lower Carlile and Juana Lopez Members, where thin beds of calcarenite and very-fine sandstone are also present. In the southwest of the San Juan Basin, the Juana Lopez is conformably overlain by the Montezuma Valley (Upper Carlile) Member, which intertongues with the Gallup Sandstone, but in the more distal regions erosion has removed these overlying strata and the Juana Lopez is unconformably overlain by the upper Mancos at the Tocito unconformity. In contrast, the upper Mancos, which has been informally divided into units (descending) A, B, and C, and reaches thicknesses of 500 metres in the centre of the basin (Broadhead, 2015), is mainly dark-grey marine shales with considerably less interbedding and sedimentary structures, particularly in units A and B. The upper Mancos A intertongues with, and is overlain by, the Point Lookout Sandstone. The San Juan Basin has been producing oil and natural gas since the 1920s and the upper Mancos unit C has been the primary source rock, though recently it has been given increasing attention as an unconventional reservoir as well (Broadhead, 2021).

Detrital zircon analysis and dating has shown a major shift in sediment provenance in the San Juan Basin across the Tocito unconformity (Ferron, 2019). The underlying Gallup fluvial sandstones, which would be associated with the lower Mancos, show a dominant source from western terranes such as the Sevier orogenic belt, the Cordilleran Magmatic Arc, as well as other mixed terranes while the overlying Torrivo sandstones, which are part of the Coniacian Crevasse Canyon Formation, are mainly sourced from the southern Mogollon highlands and are more feldspathic than the Gallup (Ferron, 2019). Geochemical studies of the Mancos Shale (and various members of it; e.g., Blue Gate, Tununk) have shown it to be overall a more siliceous mudstone relative to other mudstones of North America such as the Marcellus, Eagleford, and Haynesville Shales, with less than 20% carbonate content and roughly equal amounts (∼40% each) of silica (quartz) and clay, mainly illite but also some kaolinite and smectite (Birgenheier et al., 2017). However, there is strong variation in the relative amounts of each of these components with increasing distance from shoreline. While total siliciclastic content decreases offshore, the clay fraction (Al, K, Rb) increases from the shoreline to the prodelta and proximal mudbelt before decreasing through the rest of the hemipelagic zone with the other siliciclastics (Gabriel et al., 2022b). In addition to being more calcareous, these distal hemipelagic and pelagic sediments, which are deposited well below storm-wave base (SWB), typically have higher amounts of Cu and redox-sensitive elements indicating an increased preservation of marine organic matter (MOM) relative to more proximal depocentres (Hart, 2016; Birgenheier et al., 2017; Gabriel et al., 2022b).

4.3 Materials & Methods

The core used for this study is a 94-metre succession of Mancos Shale, in five continuous but separated intervals, that was drilled from the San Juan Basin by Schlumberger/TerraTek (Well ID: San Juan 28-6 148M; 36.6425°N, -107.4506°W) in Rio Arriba County, New Mexico (see Figure 4.1). The core is archived at the New Mexico Bureau of Geology and Mineral Resources in Socorro, New Mexico and the slab portion was loaned to McMaster University for non-destructive analysis of the lithology and elemental composition. In addition to the core material, well-log data (NGR, SP, resistivity) and an overall core description and interpretation by Weatherford Industries were provided. The well-log data were used to approximately align this core to the USGS cross-section for the northwestern San Juan Basin to provide stratigraphic position and allow correlation of the distal mudstone to shoreline facies transitions (Figure 4.2). It should be noted that a direct correlation was difficult because 1) this well is located to the

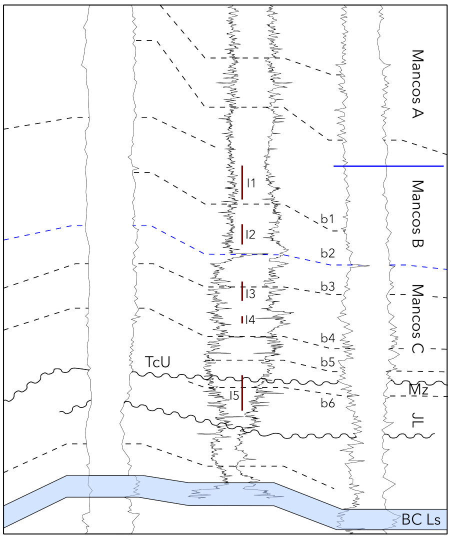

Figure 4.2: Alignment of the well-log data from Well 148M 28-6 (this study) to the well-log data from the cross section of Molenaar et al. (2001). Fine dashed lines represent uncertain contacts, wavy lines represent unconformities (see Figure 4.1), and the blue lines (dashed and solid) denote the member boundaries of the upper Mancos as defined by Broadhead (2015). Estimated contacts that are within the entire span of the core are numbered but only b6, which marks the boundary between the Juana Lopez and Montezuma Valley member, and b3, which may be associated with a minor flooding surface in the Dalton Sandstone, appear to intersect with any of the core intervals (I5 and I3, respectively). The Tocito unconformity (TcU) also intersects with I5.

southeast of the transect between hole 24 and 25 and therefore may have had local differences in depositional environment, and 2) the USGS cross-section used a variable datum for interpretation and therefore the surfaces may not be in the correct orientation to align with the San Juan well. Each core box, which contained up to 3 metres (10 feet), was photographed prior to any analysis using a Nikon D3200 12-megapixel digital-SLR camera and lithology was then described from the core and the photographs, which allowed for contrast and scale changes to enhance the subtle variations through the more-visually homogenous intervals.

4.3.1 μXRF Data

Elemental data were collected with an Itrax μXRF Core Scanner, which can analyse up to 1.8 metres of core in a single, automated process with minimal preparation of the sample required, particularly with well-consolidated sedimentary rock. The core was transferred from the boxes to an acrylic semi-tube with an internal diameter matching the core ($\sim$9 cm) to be loaded into the scanner and black modelling clay was used to support the core and fill in cracks where necessary to ensure a flat, level surface. Each section was analysed with a molybdenum X-ray tube (30 kV, 33 mA) at a 0.5-mm sampling interval and 15-second exposure time. To obtain the elemental intensities in total counts (cts), the raw energy spectra from each interval were batch analysed using QSpec software (Cox Analytic Systems), which aims to minimise the mean-squared error between the obtained raw spectra and the 'expected' spectral curve by adjusting the X-ray tube parameters and which elements are present. All subsequent statistical analyses were performed in RStudio® (GNU Affero General Public License v.3) using R version 4.1.2+ (R Core Team, 2021) and various openly-available statistical packages.

The chemofacies were established using an unsupervised, hierarchical clustering algorithm known as a Self-Organising Map (SOM; R Package SOMbrero Vialaneix et al., 2020), which is an iterative algorithm where observations in multi-dimensional space compete for nodes in a grid based on a discriminant function, such as the Euclidian distance between the node and observation (see Gabriel et al., 2022a,b). Prior to being input into the SOM, the data were 'centred' using a row-wise Z scaling ($\mu_{row} = 0$, $\sigma_{row} = 1$) so that each element was normalised to the total elemental signature of that interval, which represents an instant of geologic time. By scaling the data to the observation rather than the variable (i.e., element), the strong distinction between laminae of different lithologies, say siliciclastic mud and sand, is maintained (Gabriel et al., 2022a,b). After scaling, the dataset was reduced to 19 elements that are common to palaeoenvironmental studies and have good detection efficiency with an Itrax (Croudace et al., 2006; Gregory et al., 2019; Gabriel et al., 2022a): Al, Si, S, Ca, Ti, K, Sb, V, Cr, Mn, Fe, Ni, Cu, Zn, Rb, Sr, Zr, Th, and U; the ratio of incoherent:coherent scatter (ICR) was also included as it tends to vary with sample density (Brown et al., 2007; Boyle et al., 2015) and has values of a similar order as the normalised elements. The initial tesselation is approximated by a square grid with side length of $\sim 5\sqrt{n}$, where n is the number of observations, and since the SOM is topologically invariant, those clusters can be further grouped into *superclusters* to address the specific questions of the research. For example, Gabriel et al. (2022b) used four superclusters to characterise the dominant depositional environments in a 17-metre long interval of Mancos Shale but showed that eight superclusters were able to further divide the intervals into periods of higher marine organic matter (MOM) preservation or increased siliciclastic input, as well as isolate a visually-identified bentonite layer.

4.4 Results

4.4.1 Chemofacies from the SOM

For the entire dataset ($n = 185,237$ observations), an initial grid of 40 by 40 was used (1600 clusters) and then further clustered into $k = 4$, $k = 8$, and $k = 12$ superclusters to describe the chemofacies and associate them with a depositional environment (Figure 4.3; Cf. Gabriel et al., 2022b). Overall, the chemofacies established using $k = 4$ superclusters show an increasing water depth and distance from a fluvial source, as seen by Gabriel et al. (2022b), based on variations in Fe, Ca, Ti, K, and V/Cr. Chemofacies 3 (CF3; $n = 30,992$ observations) is a *siliceous* mudstone with exceptionally high values of Fe (μ = 17.13 x10^4) relative to Ca (μ = 2.96 x10^4), similar values of Ti relative to K (μ = 6.66 x10^3 and μ = 7.73 x10^3, respectively), and low V/Cr (i.e., oxic sediment, μ = 1.00). Chemofacies 1 (CF1), which was the most abundant ($n = 94,969$ observations), is an *intermediate* mudstone with nearly equal values of Fe and Ca (μ = 8.34 x10^4 and μ = 8.96 x10^4, respectively), similar values of K relative to CF3 (μ = 7.44 x10^3), although there is a significant drop in Ti (μ = 3.62 x10^3), and a slight increase in V/Cr (μ = 1.91) suggesting decreased oxygen in the sediments. Chemofacies 2 (CF2; $n = 58,629$ observations) is a *calcareous* mudstone showing further decreases in Fe (μ = 6.81 x10^3), Ti (μ = 2.13 x10^3), and K (μ = 5.00 x10^3) and the highest Ca (μ = 18.05 x10^4) and all proxies have a higher standard deviation than CF1 indicating more variable conditions. Chemofacies 4 (CF4) has moderate values in all proxies, falling roughly between CF1 and CF2, but rarely occurs through the core ($n = 647$) so was not included in the overall chemostratigraphic interpretation.

At $k = 8$ and $k = 12$ superclusters, the three main chemofacies were divided into groups with enrichments in various elements. The siliceous mudstone, CF3, was divided

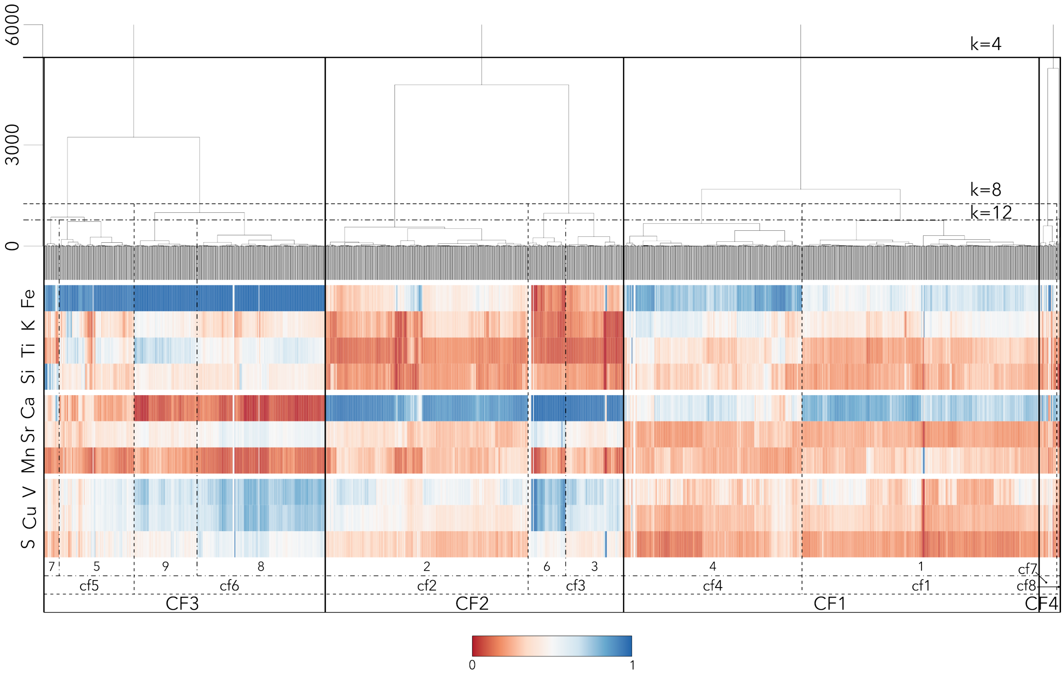

Figure 4.3: Cluster dendrogram and heat maps of select elements included in the Self-Organising Map. The initial 1600 clusters are generated with an unsupervised algorithm, which eliminates any researcher bias, but the number of superclusters, k, can be chosen based on researcher knowledge and to match the specific research goals.

into a group with higher Fe, Ti, V, Cu, and S at $k = 8$ (cf6) suggesting higher terrestrial input resulting in lower oxygen conditions and more preservation of organic matter and at $k = 12$, a group clustered out with exceptionally high Si compared to any other cluster in the core (7). This group also had low abundances of Ti and K and the lowest V/Cr values, although the standard deviations were among the highest. The intermediate mudstone, CF1, was also divided into groups based on higher values of Fe, K, Ti, and Si (cf4) although the Fe, Ti, and Si abundances are all lower than any grouping from CF3; K is similar in abundance and standard deviation between the groups. The abundances of V, Cu, and S, which are the lowest in CF1, show minimal variation between the higher-order superclusters, indicating consistently oxygenated conditions in these sediments. Finally, the calcareous mudstone, CF2, was divided based on enrichments in V, Cu, and to a lesser degree, S (cf3), but the siliciclastic elements were low in both groups; cf3 also had a single cluster with the highest S and high Fe indicating that some sparse areas of anoxia existed during or post deposition of these sediments.

4.4.2 Chemostratigraphy

The core is in five separate but continuous intervals that have a total span of 6557'-7285' drilling depth: I1, 6557'-6657' (~29 m); I2, 6729'-6789' (~18 m); I3, 6898'-6956' (~17 m); I4, 7000'-7021' (~5.5 m); and I5, 7180'-7285' (~24 m); core was not collected between these intervals (Figure 4.4). Most of the core comes from the upper Mancos, units B and C (Broadhead, 2015, as described by), with a section of the lower Mancos (Montezuma Valley and Juana Lopez members) present in I5 below a major surface of erosion representing the Tocito unconformity at 71.5 m. Based on comparison with the USGS cross section, I1 has the most distal depocentre, 170-180 km from shoreline, while the lower part of I5 is the most proximal at roughly 70 km from shoreline. The WIS likely had very shallow shelf slopes (0.04°-0.3° Bhattacharya and MacEachern, 2009; Molenaar et al., 2001) so the water depths would be <100 m for I5 up to >150 m for I1, which is evident in the lithology.

The elemental intensities, presented in total counts (cts) or kilo-counts (kcts) of fluoresced X-rays with a given energy, along with the chemofacies were used to characterise the sediments based on their composition and proximity to shoreline. In particular, Fe/Ca (proximity/water depth), Ti+K+Si (siliciclastic input), Ti/K (weathering intensity), V/Cr (relative oxygenation), and Cu/Ti (marine organic matter) have been shown to have meaningful differences between depositional environment (delta front, prodelta, mudbelt, sediment-starved shelf) not just in their respective values but also in the spread and variance of the data (Gabriel et al., 2022b). Chemostratigraphic flooding surfaces were placed at the point of maximum regression (transgressive flooding surface; TFS)

Table 4.1: The mean and standard deviation values for several proxies according to supercluster: $k = 4$, CF1-3; $k = 8$, cf1-6; $k = 12$, 1-9. The bold and italic numbers represent the chemofacies with the highest and lowest values for each proxy by group, respectively. The values for Fe and Ca are presented in counts x10^4 and the values for Ti, K, and Si are in kilo-counts (x10^3). The higher-order superclusters are all grouped based on the lower-order cluster they split from (i.e., CF3 divided into cf5 and cf6, which divided further into 8,9,5,7). The values for CF1, the intermediate mudstone, remained the same between $k = 8$ and $k = 12$ superclusters suggesting this environment has the most consistent conditions (see Discussion).

	Super Cluster	**Fe** μ	**Fe** σ	**Ca** μ	**Ca** σ	**Ti** μ	**Ti** σ	**K** μ	**K** σ	**Si** μ	**Si** σ	**Ti/K** μ	**Ti/K** σ	**V/Cr** μ	**V/Cr** σ
$k = 4$	CF3	**17.13**	**3.67**	*2.96*	*1.81*	**6.66**	**1.36**	**7.73**	**1.48**	**2.31**	**0.37**	**0.88**	**0.32**	*1.00*	*0.53*
	CF1	8.34	1.79	8.96	2.18	3.62	0.87	7.44	1.13	2.11	0.27	0.49	0.11	1.91	0.97
	CF2	*6.81*	*2.99*	**18.05**	**6.26**	*2.13*	*0.95*	*5.00*	*1.96*	*1.54*	*0.47*	*0.45*	*0.58*	**2.96**	**2.47**
$k = 8$	cf6	**18.16**	**3.23**	*2.16*	*3.39*	**7.1**	**0.79**	**7.98**	**1.11**	2.25	0.23	*0.32*	*0.17*	1.79	0.68
	cf5	14.38	3.35	5.09	1.97	5.47	1.78	7.07	2.02	**2.48**	**0.58**	**0.79**	**0.27**	*1.07*	*0.74*
	cf4	9.84	2.13	7.17	1.43	4.34	0.98	7.86	1.10	2.31	0.28	0.56	0.14	1.73	0.85
	cf1	7.61	0.99	9.82	1.95	3.27	0.54	7.24	1.09	2.02	0.21	0.45	0.08	2.00	1.01
	cf2	7.41	2.48	15.10	2.52	2.50	0.77	5.78	1.47	1.71	0.35	0.45	0.19	2.88	1.73
	cf3	*5.31*	*3.58*	**25.54**	**6.67**	*1.18*	*0.67*	*3.05*	*1.68*	*1.11*	*0.46*	0.46	1.05	**3.18**	**3.73**
$k = 12$	8	**19.27**	**3.42**	*2.12*	*0.86*	6.90	0.81	7.72	1.17	2.25	0.26	**0.92**	**0.41**	0.94	0.45
	9	16.09	1.26	2.24	0.81	**7.48**	**0.61**	**8.48**	**0.78**	2.27	0.15	0.88	0.06	1.03	0.35
	5	15.35	2.74	4.66	1.44	6.15	1.04	7.50	1.79	2.25	0.27	0.85	0.22	1.1	0.72
	7	10.03	2.18	7.03	2.72	2.39	1.01	5.11	1.82	**3.51**	**0.43**	0.49	0.26	*0.91*	*0.81*
	4	9.84	2.13	7.17	1.43	4.34	0.98	7.86	1.10	2.31	0.28	0.56	0.14	1.73	0.85
	1	7.61	0.99	9.82	1.95	3.27	0.54	7.24	1.09	2.02	0.21	*0.45*	*0.08*	2.00	1.01
	2	7.41	2.48	15.10	2.52	2.50	0.77	5.78	1.47	1.71	0.35	0.45	0.19	2.88	1.73
	3	6.73	4.01	21.94	4.25	1.52	0.55	3.88	1.48	1.36	0.34	0.46	0.99	**3.35**	**3.28**
	6	*3.53*	*1.72*	**30.05**	**6.40**	*0.76*	*0.57*	*2.00*	*1.27*	*0.80*	*0.40*	0.45	1.12	2.96	4.22

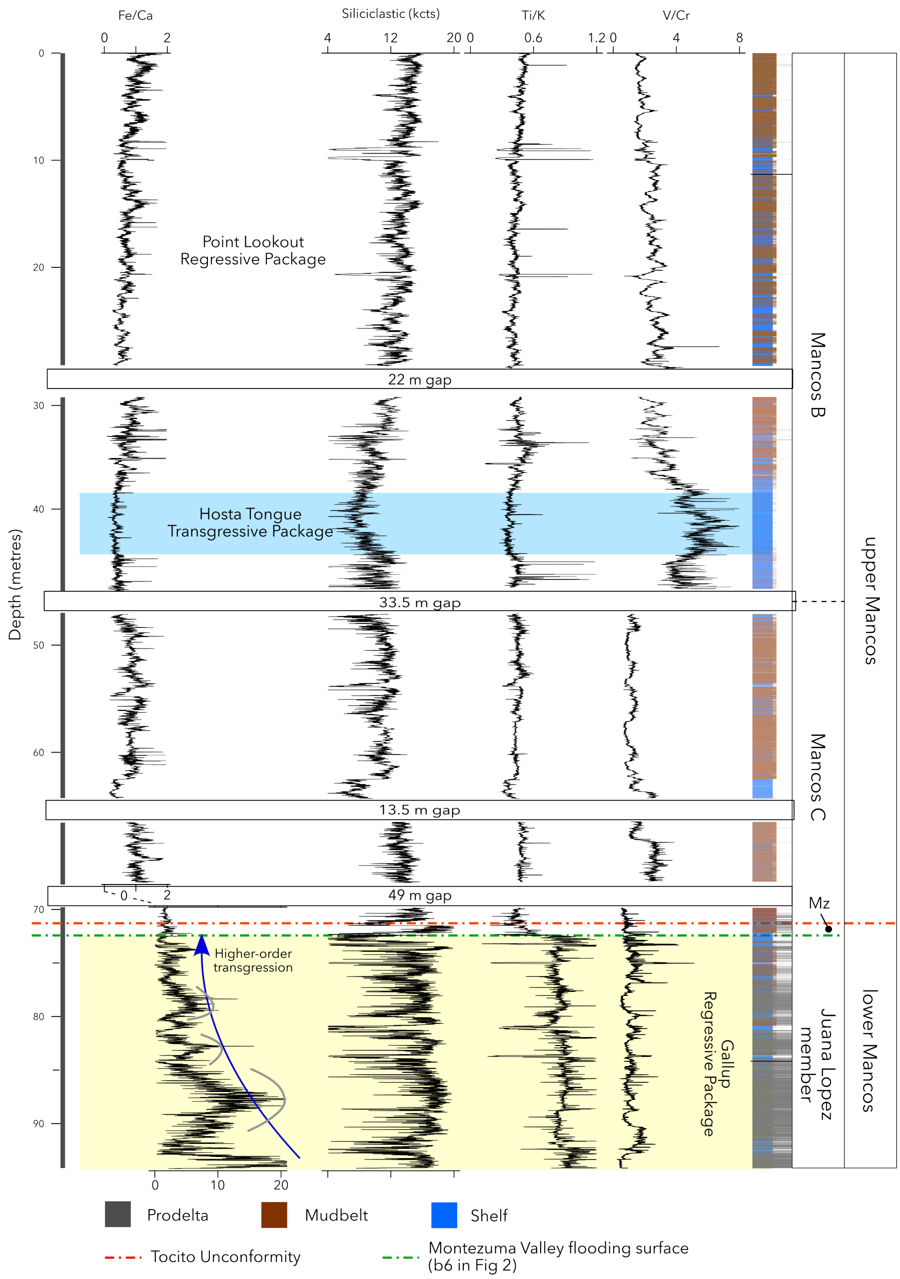

Figure 4.4: The entire section of Mancos Core showing the variation in Fe/Ca (note the order of magnitude drop between I5 and the other intervals), total siliciclastic (K+Ti+Si), Ti/K, and V/Cr. The chemofacies for k = 4 superclusters are shown on the right, along with the major lithologic units. The Gallup Regressive Package represents a major regressive phase (3$^{\text{nd}}$ order) as indicated by the high Ti/K although this core is showing a higher-order (4$^{\text{th}}$) transgressive phase as indicated by the decreasing Fe/Ca. The Hosta Tongue Transgressive Package likely represents an even higher-order (5$^{\text{th}}$?) cycle. Grey lines indicated higher-order cycle that comprise the 4$^{\text{th}}$ order transgressive phase; Mz – Montezuma Valley Member of lower Mancos.

and maximum transgression (maximum flooding surface; MFS) to establish depositional transgressive-regressive (T-R) cycles. Maximum regression was identified by peaks in the Fe/Ca and siliciclastic content while maximum transgression occurred at the troughs of those proxies; a complete T-R cycle is bounded by two MFS. The values in V/Cr and Cu/Ti, proxies for dysoxia and MOM preservation, respectively, have a similar cycle though it is roughly 90° out of phase relative to the terrestrial trends.

I1 – 6557-6657'; 0-29.2 m

Interval 1 (I1) is from the upper Mancos B and is comprised almost entirely of dark-grey mudstone with limited sedimentary structures or laminae, aside from two carbonate-rich facies at 9 and 9.8 metres and some scattered *Inoceramid* and other bivalve fragments (Figure 4.5). Overall, the Fe/Ca, siliciclastic input, and Ti/K values increase from the bottom of the section to the top, with average values going from 0.541-1.52, 12.39-14.74 kcts, and 0.416-0.509, respectively. There is an associated decrease in the average V/Cr, with values going from 2.77 at the bottom to 1.67 at the top. The chemofacies at the bottom of the core mainly comprise CF2 (calcareous mudstone), which fluctuates moving upcore becoming more dominated by CF1 (intermediate mudstone).

I2 – 6729-6789'; 29.2-47.1 m

Interval 2 (I2), also from upper Mancos B, has considerably more lithologic variation. The bottom 3 m (44-47 m) has numerous laminations and ripple beds comprised mainly of silt- to sand-sized carbonate grains, based on thin section analysis by Weatherford Industries (J.Rine, *pers.comm.*). This transitions upcore to a more homogenous lithofacies (relative to the rest of I2) with sparse coarse-silt planar laminae defines much of the middle of this interval, up to ~39 m where silt lamina thickness and frequency increase and wave-rippled laminations become more prominent; there is a large carbonate nodule at

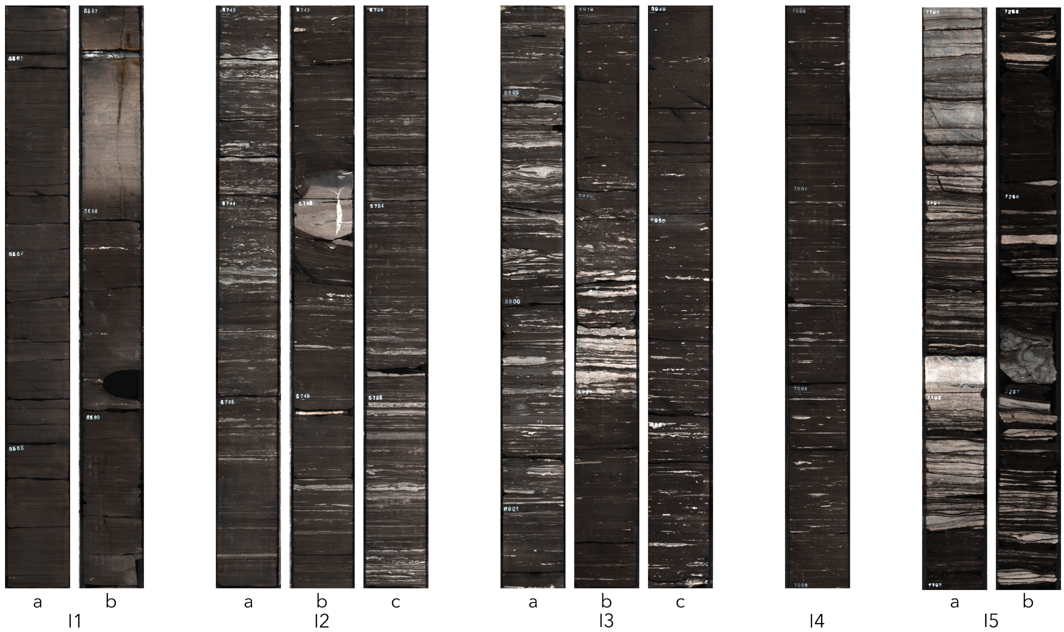

Figure 4.5: Examples of some of the lithofacies that make up the Mancos Core. All images are ∼1 m intervals; white number stamps represent core drilling depth in feet. **I1a** – structureless, intermediate (CF1) mudstone that comprises almost the entire 29 m of I1. **I1b** – carbonate-rich interval at 9 m. It has gradational top and bottom contacts and internal structures (wavy laminations?) are visible. **I2a** – transgressive surface in the upper portion of I2 with basal scour underlying rippled-siltstone and moderate bioturbation. **I2b** – relatively structureless mudstone towards the top of I2. The carbonate nodule has sharp contacts all around and deformation of the surrounding laminae is visible. **I2c** – the calcareous mudstone (CF2) at the base of I2 with significantly more laminations, including wave ripples with basal scour and dense planar laminae. **I3a** – top portion of I3 showing highest-energy conditions with wave rippled silt to very fine sandstone. The coarser sediments are comprised of skeletal carbonate material, not quartz, indicating deep-water deposition and reworking by storm waves. **I3b** – calcitic grainstone bed. **I3c** – transition from silt-streaked calcareous mudstone (CF2) to structureless intermediate mudstone (CF1) i.e., marine regression. In shallow siliciclastic environments, this transition may be interpreted as a flooding surface (transgression) due to the decrease and disappearance of silt-sized lamina. **I4** – silt-streaked intermediate mudstone that comprises the entirety of I4; laminations decrease upcore. **I5a** – thick-bedded sandstone near the top of the Juana Lopez Member, indicating the highest-energy depocentre. **I5b** – siliceous mudstone (CF3) with wave-rippled sandstone at the base of I5. The sandstone beds have basal scour and show internal cross-laminations. Despite looking similar to the structureless mudstone of I1, the mudstone intervals in I5 belong to the siliceous mudstone chemofacies (CF3) and are therefore shallow-water mudstones.

35 m. At 33 m, the lithofacies sharply transitions to a mudstone with numerous laminations and ripple beds of skeletal carbonate material (foraminifer, pelecypod, brachiopod, *Inoceramid* fragments; J.Rine, *pers.comm.*), suggesting an erosive surface possibly due to a marine transgression. This transitions to a final homogenous mudstone lithofacies with sparse fine-silt lamina that is more similar in appearance to I1 than other sections of I2.

This interval shows a similar overall increase in Fe/Ca from the bottom to the top, although the regular cyclicity that is seen in I1 is not as apparent in this interval until the upper few metres, above ~34 m. The siliciclastic input, V/Cr, and Ti/K (to a lesser extent), however, all show an intermediary phase of shoreline transgression that is not as apparent in the Fe/Ca signal. The trends are relatively straight from the bottom to ~45 m, where there is a decrease in total siliciclastic and Ti/K to 42 m and an associated increase in V/Cr, indicating a significant shoreline transgression. The chemofacies through this section are dominated by CF2, with only sparse intervals of CF1, indicating an even more calcareous mudstone, relative to the base of I1. Above 42 m, the siliciclastic and Ti/K values increase with the Fe/Ca, the V/Cr values decrease, and the regular cyclicity observed in I1 becomes more apparent. This is also associated with an increase in the abundance of CF1, indicating a more siliceous mudstone towards the top of the interval.

I3 – 6898-6956'; 47.1-64.3 m

Interval 3 is a part of upper Mancos C, occurring below a major condensed section seen in the gamma log, and shows a similar lithology to I2, with lithofacies varying between more visually-homogenous mudstone with sparse fine-silt laminae to units with abundant planar and wave-rippled silt to fine-sand laminae that are mainly comprised of carbonate material. There is a 20-cm thick calcitic grainstone unit and 2-cm thick bentonite present in I3. The base of this interval is mudstone with sparse starved-ripple laminae comprised of carbonate material, which transitions rapidly into structureless mudstone ~63 m that is punctuated only by the bentonite until ~55 m where the sediments become more laminated with thin (millimetre-scale) siltstone laminae that are either relatively planar and continuous across the core or starved-rippled and discontinuous. The top 1.5 m of this interval has centimetre-scale beds of silt-sized grains showing convex-up, nearly symmetrical wave ripples, dense, planar laminations, and scour surfaces indicating deposition a relatively high-energy setting. As in I2, these silt-sized laminae were comprised of skeletal carbonate material. The last 0.5 m transitions back to a more homogeneous mudstone with streaked, thin silt laminations.

The silt-streaked mudstone at the base of this interval almost entirely comprises the calcareous mudstone chemofacies, CF2, while the structureless and laminated mudstone above 63 m mainly comprises the intermediate CF1 chemofacies indicating a transition to a shallower, more proximal depocentre, although there are some areas with more intervals of CF2. The top 0.5 m shows an increase in the frequency of CF2, indicating a shift back to more pelagic settings (i.e., deeper, more distal depocentre).

I4 – 7000-7021'; 64.3-70 m

This short interval, also from Mancos C, comprises mudstone with thin silt laminae, which decrease in thickness, frequency, and lateral continuity moving upcore. The trends in Fe/Ca, siliciclastic content, and Ti/K are relatively stable through this interval but there is a significant shift in the V/Cr (oxygenation) values, which are higher from the base of the interval to ~66 m, where they rapidly decrease over several centimetres. Overall, this interval comprises the intermediate mudstone chemofacies, CF1.

I5 – 7180-7285'; 69.8-94.1 m

Interval 5 (I5) is lithologically the most heterogeneous and contains the end-Turonian Tocito unconformity, which is a major erosive surface that resulted from tectonic uplift (Figure 4.6). In the lithology, this surface is identified by structureless mudstone below with a sharp transition to overlying highly bioturbated (BI=5-6) glauconitic muddy sandstone and a burrowing surface indicative of a *Glossifungites* ichnofacies (Hu and Plint, 2009; Li et al., 2010; Zhu et al., 2012) at 71.5 m. Geochemically, the most distinct signature of this surface was in the Si/K values, which spike (i.e., sharp basal contact) at the transgressive surface in contrast to the more gradual increases seen in the sandy beds at the bottom of the figure. At $k = 12$ superclusters, this interval was isolated as a sub-cluster of the siliceous mudstone chemofacies, CF3, and it does not occur anywhere else in abundance in the whole core section.

The lowest 10 m of I5 is mostly dark, structureless mudstone with occasional centimetre-scale beds of wave-rippled, very-fine sandstone, which could be the result of larger storm events. Despite being visually similar to the structureless mudstone in the higher intervals, the chemofacies shows these mudstones to be the most siliceous and were therefore deposited much closer to the palaeoshoreline than the mudstones in the higher intervals. The variability in all of the proxies appears higher in this lowest interval as well, further supporting deposition in a higher-energy environment. Bedding thickness and frequency increase from ~84 to 80 m, and some sandstone intervals show relatively high-angle beds suggesting deposition within the prodelta, which would have higher-angle clinoforms than the relatively flat mudbelt and shelf. There is a sharp transition to structureless mudstone at 80 m (i.e., a flooding surface) but laminations begin within a metre, first as millimetre-scale, starved ripples that are discontinuous across the core and then transitioning to larger, centimetre-scale laminations and finally to rippled sandstone beds that are several centimetres thick. Around 72 m there is another rapid transition to

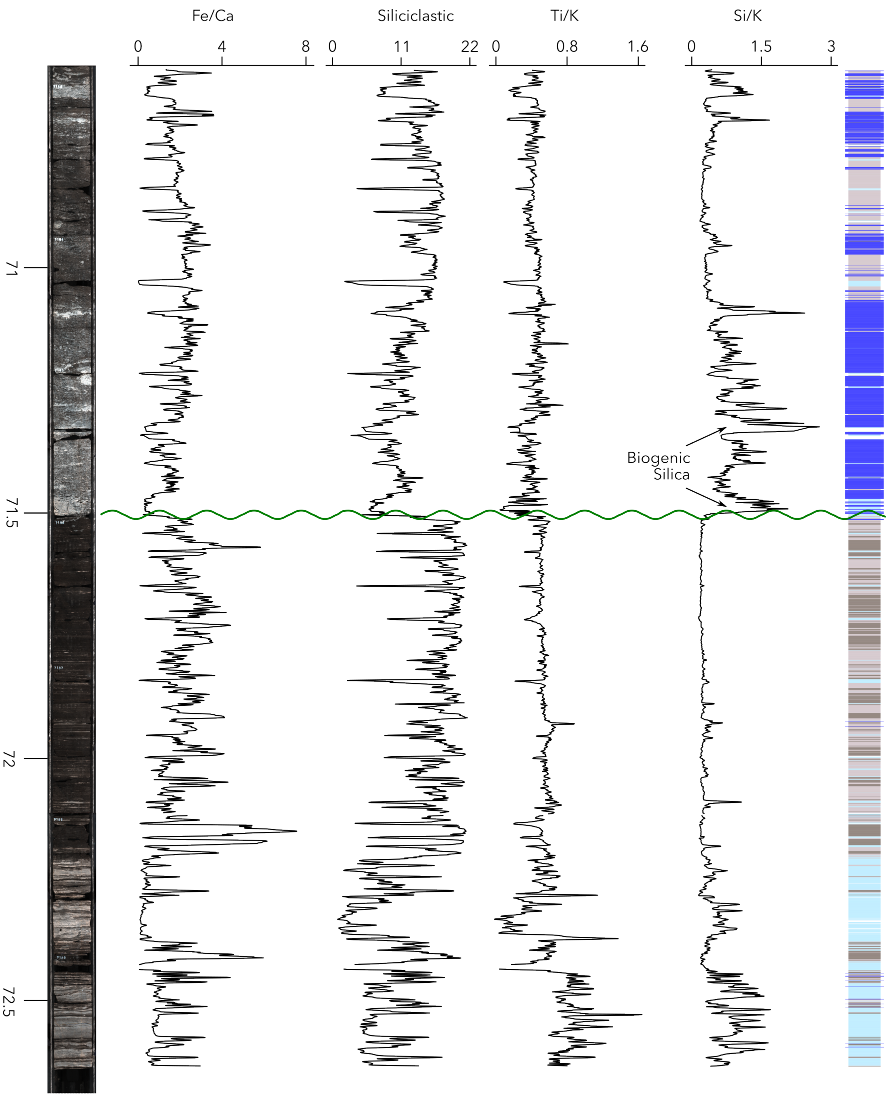

Figure 4.6: The lithology, chemostratigraphy and chemofacies signature of the Tocito unconformity. In the lithology, this surface is a sharp-contact between underlying dark mudstone and overlying glauconitic sand with a *Glossifungites* ichnofacies at the contact. Geochemically, this surface is mainly defined by a spike in Si/K as a result of winnowing of the clay fraction in combination with an increased influence from biogenic silica. The chemofacies that identifies this zone clustered out at $k = 12$ superclusters (see Figure 4.3)

structureless mudstone, which would likely start a similar succession as the previous cycle except for the major erosive surface associated with the Tocito unconformity.

4.5 Discussion

4.5.1 Chemofacies with a Self-Organising Map

The SOM clustering is a rapid way to group sediments, even visually homogenous ones, based on their geochemical signature. Even prior to analysing and interpreting the clusters, graphically plotting them can show variability at a variety of scales allowing for more precise correlations (Figure 4.7). By plotting the elemental data as heat logs against the dendrogram, even a cursory view can point out where different elements are clustering together, and the number of superclusters can be adjusted accordingly to isolate them.

Comparing the makeup of these chemofacies to those presented by Gabriel et al. (2022b) allows the sediments to be interpreted based on their depositional environment and proximity to shoreline. The siliceous chemofacies, CF3, had a similar makeup to the prodelta facies identified in the late-Turonian Ferron-Notom delta, which is located farther north along the palaeoshoreline from the San Juan Basin, but with higher values in siliciclastic elements, particularly Fe, suggesting increased fluvial runoff. This chemofacies is only associated with the Juana Lopez member (I5), which was contemporaneous with the Ferron-Notom delta, indicating there were environmental differences between these two areas. The difference between these environments could be due to their locations with the WIS, which had an anti-clockwise circulation, with northern Boreal (Arctic) waters being drawn south along the western shoreline (Slingerland et al., 1996; White et al., 2001; Hart, 2016; Lowery et al., 2018). The San Juan Basin is farther south than the Ferron and therefore the more distal sedimentary record may be preserving a mixed signal from the Gallup deltaic system, which is the closest source to this core, as well as the more-northern Ferron systems (Notom, Last Chance, Vernal). Alternatively, the local palaeoclimate of the southern Gallup system may have been wetter due to its closer proximity to the tropical Tethys Ocean. The intermediate chemofacies, CF1, and calcareous chemofacies each had values similar to those identified by Gabriel et al. (2022b) for the mid- to distal mudbelt and sediment-starved shelf, respectively. Due to a lack of age control for the core, accurate sedimentation rates can not be determined and those may be contributing some bias to the standard deviations. More proximal, siliceous sediments deposited on the prodelta would have a higher sedimentation rate than more distal sediments of the mudbelt and shelf so the prodelta sediments would be expected to show more variation over the same core length.

The hierarchical nature of the SOM, as well as its ability to analyse large datasets (10^6 or 10^7 observations; Kohonen, 2013), makes it ideal for analysing μXRF data with respect to sequence-stratigraphic studies as they, too, are hierarchical in nature and the SOM can be easily tailored to meet the needs of the study. As the scale of the study decreases, so too does the areal extent of the surfaces and conformable units that are being

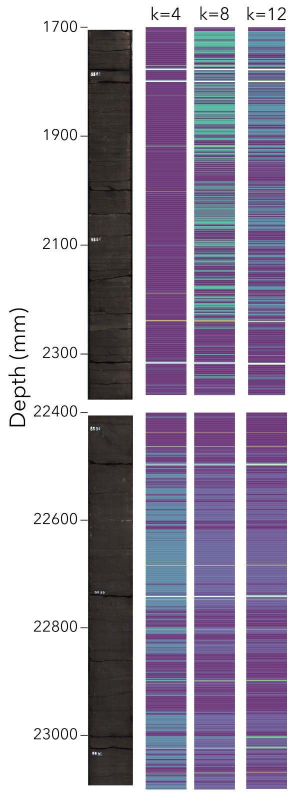

Figure 4.7: A comparison of the chemofacies for two visually-identical structureless mudstone units. Even without interpreting the chemofacies, differences can clearly be seen between the two units indicating they were subject to different environmental conditions at the time of deposition. By increasing the number of superclusters it can also be seen that the upper unit (1700-2400 mm) also has more inherent heterogeneity than the bottom unit, which shows a nearly identical pattern in all three logs even though the colours are slightly different.

mapped (Catuneanu, 2019). With $k = 4$ superclusters, the chemofacies described large-scale variations between depositional environments according to water depth (prodelta, proximal mudbelt, and distal mudbelt/shelf), likely at the scale of 3rd order sequences (seismic-scale). These sequences typically describe continental- to global-scale variations and can therefore be correlated across several basins. However, higher-order cycles describe variations at a basinal or even sub-basinal scale and can therefore be used to correlate across more-localised regions.

By increasing to $k = 8$ and $k = 12$, sub-environments could be identified within these major zones (Figure 4.9), including the transgressive surface of erosion associated with the Tocito unconformity at $k = 12$ superclusters, which was a grouping of the prodelta chemofacies (CF3) with high Si values. Increasing the number of superclusters also showcases the variability in the prodeltaic environment, particularly in siliciclastic content, and shelfal environment, where the variability can be seen mostly in the redox conditions, compared to the relative stability of the mudbelt. As mentioned above, the higher sedimentation rate in the prodelta, combined with those sediments being deposited during the warmest period of the Turonian, would naturally lead to more variation in the environmental proxies. However, the variation seen in the shelf, where sedimentation rates are significantly lower, is an interesting result and suggests that bottom water currents were highly variable in terms of their energy and oxygenation. More stable conditions in terms of V/Cr (lower standard deviation) are associated with periods of higher siliciclastic content (Fe, Ti, and K), which may indicate that the higher clay content acts to suppress the bottom currents, similar to the mudbelt. During times of higher Ca, the sediments comprise marine organic matter from pelagic fallout (foraminifera, coccolithophores, calcareous algae) and an increased flux of this organic matter could lead to dysoxic conditions through microbial degradation. An alternative explanation is that

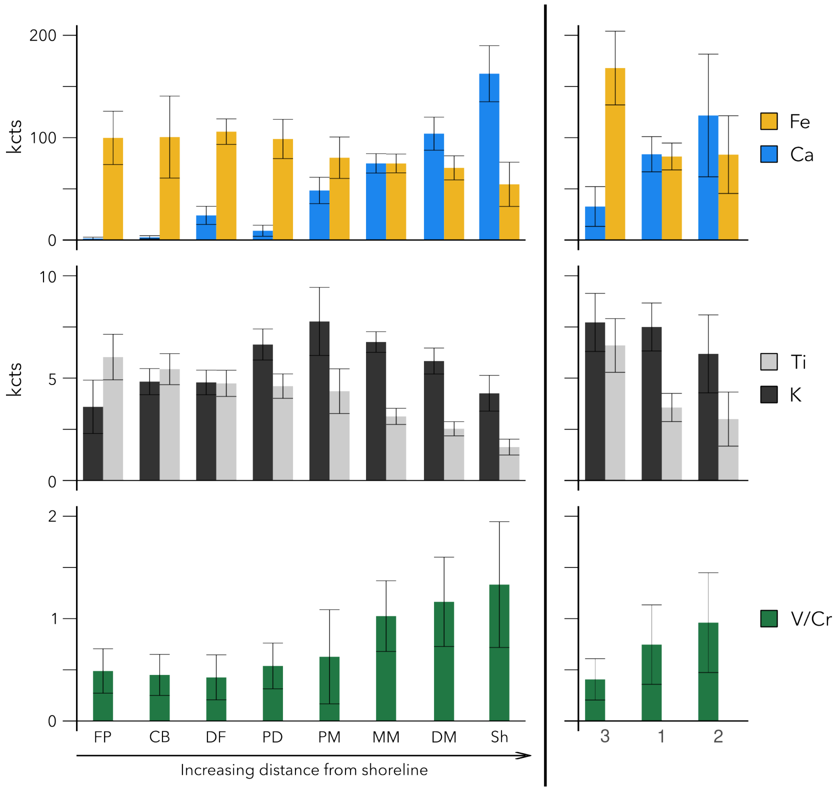

Figure 4.8: Bar plots showing the mean and standard deviations for Fe, Ca, Ti, K, and V/Cr by chemofacies/depositional environment. Data on the left are from Gabriel et al. (2022b) (FP - Floodplain; CB - Channel Belt; DF - Delta Front; PD - Prodelta; PM - Proximal Mudbelt; MM - Mid-Mudbelt; DM - Distal Mudbelt; Sh - Shelf). The chemofacies identified here are mostly similar in composition to the prodelta, mudbelt, and shelf although the prodelta facies in this core, CF3, is higher in Fe, Ti, and K than the prodelta from their study, which is represented by the Ferron-Notom Member of the Mancos Shale.

the variation is related to the location of this core in the WIS. Computer-generated circulation models suggest that the WIS had an anti-clockwise circulation, with warmer waters of the Tethys being drawn up the eastern shores and cooler Boreal water flowing south along the western margin, and that the confluence of these waters may have been close to the area of the San Juan Basin (Slingerland et al., 1996; Lowery et al., 2018). Changes in thermohaline circulation may have caused the mixing front of these two water masses to shift and since the Boreal waters are more oxygen-rich and carbonate-poor than the Tethyan, this would impact both the redox conditions and Ca content at the sediment-water interface. It can also be seen that the average values of elements may not be sufficient to distinguish between sediments deposited in different zones and instead requires the spread of the data as well.

4.5.2 Chemostratigraphic Signature of Surfaces

Accurate reconstruction of depositional cycles in a basin requires the identification of significant chronostratigraphic surfaces that can be correlated across several cores. Sequence boundaries have been shown to have significant diachroneity and therefore flooding surfaces are considered more effective chronostratigraphic surfaces (Bhattacharya, 2011). Furthermore, all depositional cycles from the sequence down are built of smaller stratal packages (e.g., parasequences, bedsets, laminasets) that are bounded by flooding surfaces, so they are more appropriate to use in hierarchical analyses. Within a complete T-R cycle there are two key flooding surfaces: the transgressive flooding surface (TFS) which occurs at the point of maximum regression and the initial sea-level rise and the maximum flooding surface (MFS) where sea level stabilises and the shoreline begins to aggrade/prograde again. In the μXRF data, maximum regression is identified at the point where increasing siliciclastic content due to shoreline progradation switches to a decreasing trend as a result of relative sea-level rise (Figure 4.10). This is the point where the chemostratigraphic TFS was placed. Above the TFS, siliciclastic content decreases rapidly through the marine transgressive phase, which is typical of the trends seen in near-shore environments where the transgressive systems tract is condensed relative to the highstand and lowstand tracts (regression) due to lower sedimentation rates as the depocentre increases in distance from the shoreline (Bhattacharya et al., 2019). The chemostratigraphic MFS is identified at the end of the transgressive phase where siliciclastic content starts to increase again.

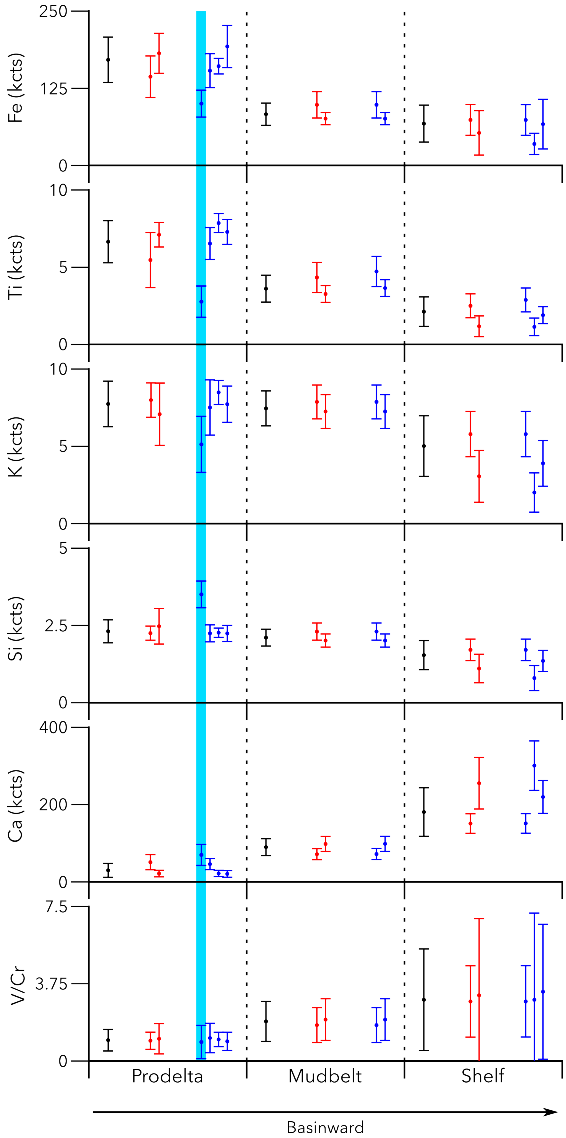

Figure 4.9: Mean and standard deviations of Fe, Ti, K, Si, Ca, and V/Cr by depositional environment for $k = 4$ (black), $k = 8$ (red), and $k = 12$ (blue) superclusters. The prodelta chemofacies, CF3, shows the most intra-environmental variability, dividing into two and then four sub-groups while the mudbelt shows the most consistent conditions. The light-blue vertical band represents the chemofacies associated with the Tocito transgressive surface of erosion (Figure 4.6).

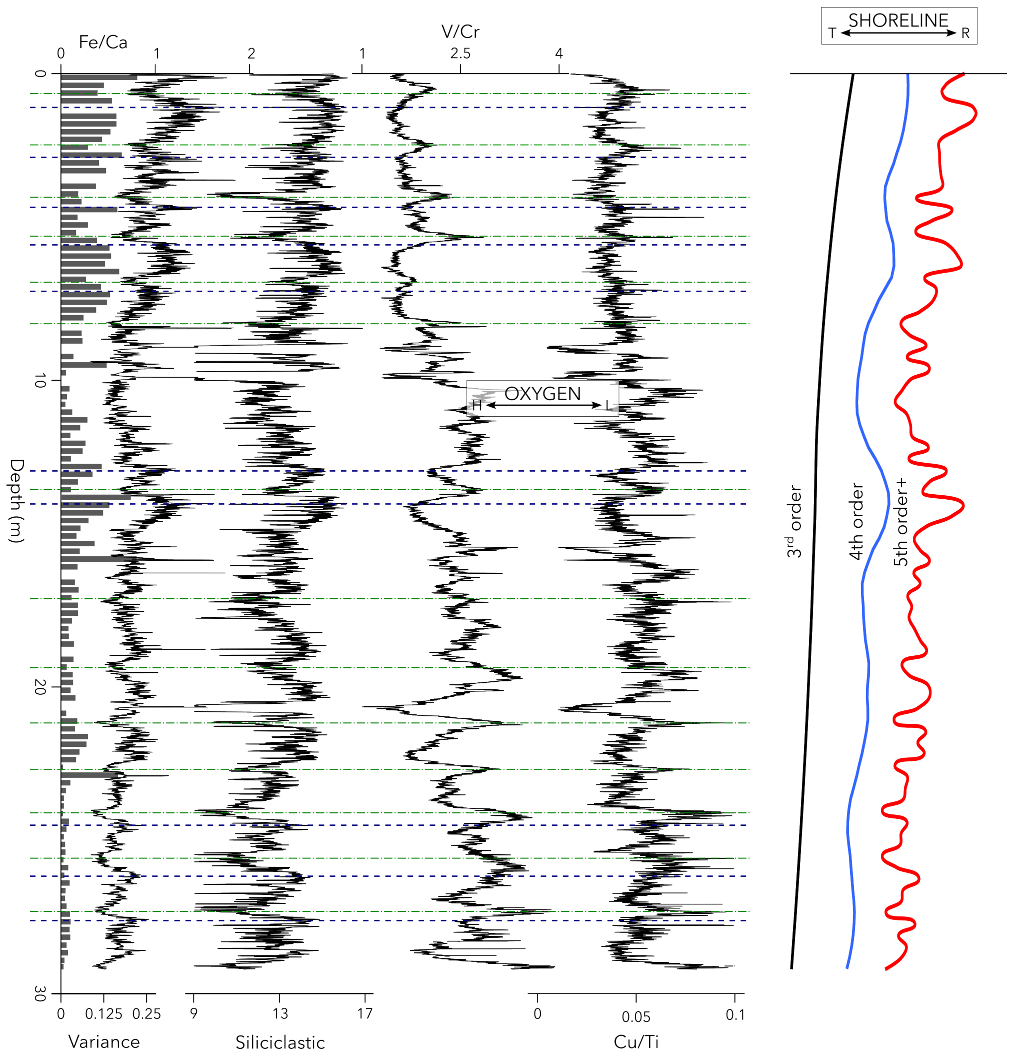

Figure 4.10: Depositional cycles through I1. Blue dashed lines represent the transgressive flooding surface and green dashed lines represent the maximum flooding surface, two of which bound a complete T-R cycle. Shoreline trajectories for 3rd (black), 4th (blue), and 5th (red) order, or higher, cycles are shown based on a loess smoother applied to the Fe/Ca data using a span of 1, 0.2, and 0.02, respectively. Due to a lack of age control, the order numbers are estimated based on the cycles present in the entire core. The variance in the Fe/Ca data was calculated in 20-cm bins and also follows the shoreline trajectory.

While these surfaces can be reliably identified in 3rd- and 4th-order sequences (Algeo et al., 2004; Olde et al., 2015; Turner et al., 2016), the ability to reliably identify both of these surfaces in higher-order cycles is unique to the high-resolution sampling of μXRF. In near-shore environments, these two surfaces often occupy the same space due to a hiatus in sediment deposition (i.e., an unconformity) but in the distal environments these surfaces separate and the data between them represent a correlative conformity. Therefore, identifying both of these surfaces not only provides for better correlation to near-shore depositional cycles but also provides a palaeoenvironmental record of time span between them, something that is not possible in near-shore environments. This will enable the expansion of sequence-stratigraphic frameworks into the distal muddy facies providing for more accurate basin reconstructions, aiding in both palaeoclimatic research and hydrocarbon exploration.

The Tocito unconformity, present in this core at 71.5 m, is a major transgressive surface of erosion resulting from tectonic uplift and shows a significantly different chemostratigraphic signature. While the other areas of the core record the transgressive phase following the TFS, the Tocito is represented by a sharp transition in several proxies, but particularly in the Si/K ratio and in the chemofacies at $k = 12$ superclusters. An increase of silica relative to the other siliciclastic elements can indicate intervals of increased biogenic silica from siliceous micro-organisms such as diatoms and radiolaria. The Si/K ratio is low and mostly constant through the lower interval of mudbelt deposition but spikes at the *Glossifungites* surface that lithologically identifies a transgressive surface of erosion (Hu and Plint, 2009; Li et al., 2010; Zhu et al., 2012). There are a few more spikes in the Si/K throughout the bioturbated, glauconitic sandy interval above the Tocito unconformity, all of which are associated with *Glossifungites* surfaces, so this may also prove to be a unique geochemical signature of this ichnofacies.

4.5.3 Chemostratigraphic Signature of Depositional Phases

Not only were the μXRF data able to identify both surfaces with greater accuracy, they provided significantly more information about the behaviour of each individual T-R cycle related to the near-shore stacking patterns (progradational, aggradational, retrogradational; Figure 4.11). Each T-R cycle is bounded top and bottom by a chemostratigraphic MFS and could be observed at a number of different orders, which all typically contain a longer record of the regressive phase than the transgressive one. The regressive phase also showed differences in the stacking patterns (progradational, aggradational, retrogradational), which are related to the relationship between sediment supply and accommodation space. The regressive interval of the bottom cycle (TR1), which covers ∼1500 mm, initially shows a strong progradational phase (i.e., low slope in Fe/Ca vs Depth) followed by a moderate retrogradational phase and finally a second progradational phase; the subsequent transgressive interval of this cycle declines over ∼250 mm. In contrast, the next T-R cycle, TR2, exhibits only a single progradational phase which is weaker (i.e., higher slope), due to a more aggradational stacking pattern, and slightly shorter (∼1200mm) than TR1 followed by a transgressive interval covering ∼450 mm. Finally, TR3 begins with a stronger progradtional phase, similar to TR1, which is followed by an intermediate aggradational phase and then a second progradation before the transgressive interval.

The chemostratigraphic signature of the correlative conformity has so far been lacking in the literature (LaGrange et al., 2020) as traditional methods of analysing mudstone (well-log, ICP-OES/MS) lack the sampling resolution to accurately identify both the TFS and MFS. The μXRF chemostratigraphy of this Mancos core identifies two types of correlative conformity (CC), one associated with flooding surfaces and one associated with an erosional sequence boundary. The majority of the CCs were associated with flooding surfaces and showed a condensed transgressive interval (i.e., decreasing Fe/Ca

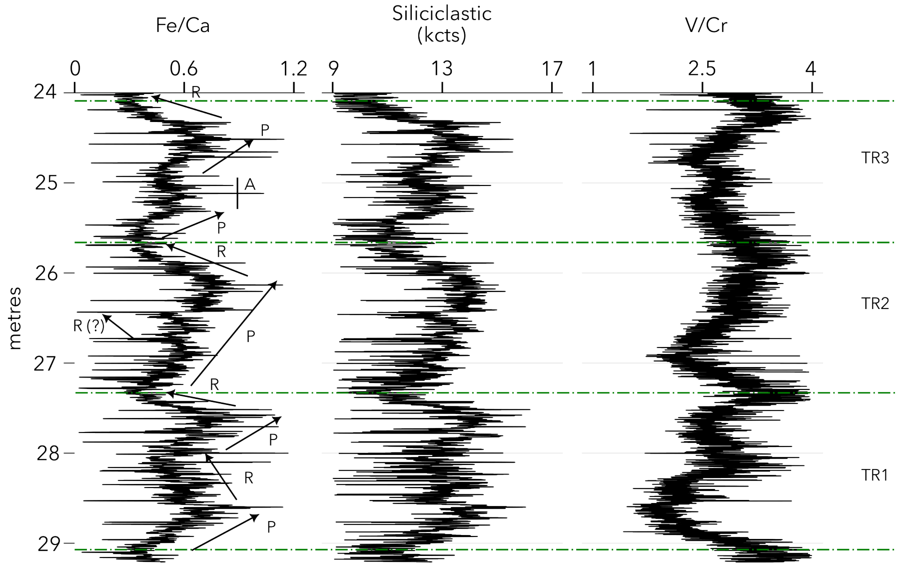

Figure 4.11: Stacking patterns in the highest-order T-R cycles identified in I1. These individual sedimentary cycles, which each occur over ∼1500 mm, show differences in their progradational (P), aggradational (A), and retrogradational (R) patterns that could be correlated to near-shore depositional systems. Each of these cycles likely corresponds to a parasequence as identified by Lin et al. (2019) and therefore represents ∼20 ka.

and siliciclastic content), relative to the regressive phase, of shoreline retreat. At the highest order cycle in I1, the CC is a relatively straight line indicating steady, continual decline but at lower orders, the transgressive phase shows a series of backstepping, higher-order cycles. Since I1 is entirely dark, structureless mudstone, these cycles can not be identified lithologically and while a higher-resolution (0.5 m) traditional geochemical study will show the overall trend, accurately identifying either of the surfaces would be purely coincidental.

The other CC is associated with a regressive phase that may identify a sequence boundary in near-shore facies as a result of relative sea-level fall (forced regression). In I3, at ∼63 m, there is a similar, but opposite, chemostratigraphic signature to the transgressive CC where terrestrial input rapidly increases over a more calcareous lower mudstone indicating shoreline progradation; this is also accompanied by a minimum in Mn/Ti, which has been previously associated with sequence boundaries (De Rafélis et al., 2001; Olde et al., 2015).

Since strict age control or sedimentation rates are not available for this core it is difficult to determine which order cycles are being identified here but if the highest-frequency T-R cycles (1500 mm) are similar to those of the parasequences identified in the Gallup sandstone by Lin et al. (2019) then each one represents ~19.7 ka, or an average sedimentation rate of 76 mm/ka. This is similar to the sedimentation rates estimated in the Bohemian Basin (Olde et al., 2015, 90 mm/ka;) and Tarfaya Basin (Beil et al., 2018, 60-90mm/ka;) so the T-R cycles in I1 are likely parasequences resulting from Milankovitch cyclicity (precession; 19 ka – 23 ka). The average sedimentation rate can be further divided into a transgressive- and regressive-phase rate, with the latter being 3-10x higher than the former. Therefore, the μXRF data were able to not only detect the Milankovitch precessional cycle but also *map* the variations within it.

4.5.4 Correlation to Near-Shore Depositional Cycles

The base of the core (I5) is part of an overall lower-order major regressive phase, indicated by the high and nearly constant values in Ti/K. The Juana Lopez Member was mainly fed by the Gallup Deltaic Complex, which was deposited over ~1.2 Ma as a series of tongues showing an overall aggradational to progradational stacking pattern (Lin et al., 2019). A similar geochemical signature was reported from the contemporaneous Bohemian Basin of Eastern Europe by Olde et al. (2015). In their core, the chemostratigraphy of siliciclastic proxies (Si/Al, Ti/Al, and Zr/Al), which was done at 2-m sampling resolution, shows a long term regressive trend through the upper Turonian, which is followed by a marine transgression into the Coniacian. While the Ti/Al and Zr/Al values drop rather quickly at the start of the transgressive phase, the Si/Al trend began a more gradual decrease much earlier (Olde et al., 2015, see Figure 5 in).

The μXRF data show very similar patterns in the Ti/K and Fe/Ca trends, which would correspond to the Ti/Al and Si/Al trends, respectively. The overall decreasing Fe/Ca values indicate a back-stepping of the shoreline due to a higher-order marine transgression, which may be associated with the large shoreline retreat between the lower and upper Gallup Sandstone (Lin et al., 2019). The highest value in Fe/Ca at the very base of the core could be the initial transgressive flooding surface between the lower and upper Gallup but it's possible a higher peak exists stratigraphically lower. Even as the Fe/Ca data show a back-stepping, the high and constant Ti/K values that quickly drop at 72 m indicate a low-order lowstand systems tract during the late-Turonian ending with a marine transgression that carried into the Coniacian; this is also identified in the Bohemian Basin by Olde et al. (2015). The final regression associated with the youngest tongue of the Gallup Sandstone is not preserved in the distal sediments of the Mancos Core as tectonic uplift created a major surface of erosion, which is the end-Turonian Tocito unconformity, although the drop in Ti/K just prior to the Tocito indicates a shift to a transgressive/highstand systems tract.

The overlying upper Mancos represents the low-order highstand systems tract, with an overall aggrading to prograding shoreline trajectory through the Crevasse Canyon and Point Lookout Sandstone, respectively. This low-order trend is represented by the overall gradual increase in Fe/Ca from I4 upwards, with an associated decrease in V/Cr and Cu/Ti indicating higher oxygen and lower preservation of organic matter. Higher-order cycles are identified in the near-shore environments, with the progradation of the Borrego Pass Lentil and Dalton Sandstone, which are separated by the Mulatto Tongue of the Mancos Shale. Based on the alignment of the core with the cross-section, the rapid increase in siliciclastic content near the base of I3 is likely associated with a forced regression during the initial deposition of the Dalton Sandstone, and would therefore represent a correlative conformity of a near-shore sequence boundary.

The core does not appear to cover the three highest fingers of the Dalton Sandstone but the net transgressive Hosta Tongue can be seen in I2 with a relatively rapid decrease in siliciclastic content combined with an increase to some of the highest values in V/Cr, indicating the lowest oxygen conditions in the core and a prolonged period of calcareous mudstone deposition (CF2). Rising sea level during the Hosta transgressed over top of a wave-dominated barrier shoreline with a broad back-barrier platform, which may have been enriched in organic matter due to calmer, lower oxygen conditions that would have been reworked and transported deeper into the basin; this may explain the dysoxic conditions implied by the V/Cr through this phase. Above the Hosta Tongue package, siliciclastic values of I1 gradually increase while V/Cr values decrease through the initial aggradational phase of the Point Lookout Sandstone.

The regularity of the higher-order cycles also increases moving upcore. The prodeltaic sediments of I5 were deposited during the late Turonian when the climate was at its hottest point in the last 115 Ma (Friedrich et al., 2012), major storm frequency was likely at decadal-scale (Bhattacharya and Tye, 2004; Sharma et al., 2017; Lin et al., 2019), and sediment provenance was from a variety of sources (Ferron, 2019), resulting in high siliciclastic input and variability. This may be indicating a mixed influence on local sea-level fluctuations from storage in aquifers and wetlands (Hay et al., 2019, e.g.,), tectonic activity (Mogollon Highlands failed rift; Bilodeau, 1986), and glacio-eustasy (e.g., Bornemann et al., 2008; Zhu et al., 2012; Lin et al., 2019) resulting in a less regular frequency. After the Turonian, the global climate began to cool as increased separation of the American plates from Europe and Africa opened the connection between the north and south Atlantic oceans, increasing the mixing between intermediate and deep oceanic water (Friedrich et al., 2012). The chemostratigraphic trends for all proxies become less variable overall and begin to show more regular cycles operating at Milankovitch-scale frequency (precession), which could be indicating the development of more extensive glaciation on the Antarctic peninsula. Alternatively, the difference in the trends may relate to the differences in depositional environment between the bottom and the top of the core. The prodeltaic sediments of the Juana Lopez Member would have had a much higher sedimentation rate than the mudbelt sediments that comprise most of the upper Mancos and therefore more variability in the sediments is expected. This may also be the reason for the highest order T-R cycles in the Juana Lopez spanning 5-6 metres compared to the 1-1.5 metre span seen in upper Mancos B (I1).

4.6 Conclusion

The lower-resolution sampling of traditional techniques has not allowed for the reliable establishment of 4^{th}-order cycles and above in mudstone units, and therefore correlating them to near-shore sequence stratigraphic frameworks has not been very effective. The 500-μm sampling obtained from a μXRF core scanner clearly showed complete depositional cycles (i.e., no unconformable surfaces) at a variety of scales and were able to provide further information about the behaviour of each cycle (progradation, aggradational, retrogradational), which can be associated with stacking patterns in near-shore facies. The shortest, regularly occurring cycle spanned $\sim$1500 mm, which likely corresponds to a parasequence representing $\sim$20 ka (Milankovitch precessional cycle), and even these cycles could frequently be subdivided into higher orders. Importantly, these cycles were evident in a 29-m succession of visually homogenous, dark mudstone and therefore could not have been reliably detected by any previous study. At each order, the regressive phase was 3-10x longer than the transgressive phase. The continuous record also provided a geochemical signature of two correlative conformities, one associated with transgression and one with forced regression, which occurred over a much shorter interval compared to the typical regressive phase. To the best of our knowledge, this is the first reported instance of the geochemical signature of these correlative conformities.

In addition to the chemostratigraphy, hierarchical clustering of the elements allowed for the establishment of high-resolution chemofacies that described the depositional conditions for each individual interval in terms of its proximity to shoreline, and weathering and redox conditions at the seabed. While the mean values for several proxies were very similar between some environments, the spread of the data could be used in conjunction with the mean to determine the depositional setting.

Elemental analysis using μXRF is ideal for studying mudstone successions, particularly where sedimentary changes lack the visual and physical heterogeneity required to be accurately distinguished by lithologic or well-log analysis. The data appeared to correlate well with near-shore depositional cycles of the San Juan Basin at several orders and also showed similarities to geochemical data collected from the eastern European Bohemian Basin using traditional low-resolution techniques. This shows that collecting μXRF data from other cores, both intra- and inter-basinally, will allow for the correlation of high- and low-frequency shoreline trajectory changes, thus providing more complete sequence-stratigraphic frameworks for palaeoclimatic research and hydrocarbon exploration.

Chapter 5.

Conclusion

This research demonstrated the utility of μXRF core scanning data to palaeoenvironmental reconstructions using marine mudstone deposits from an ancient epicontinental seaway. The high-resolution elemental intensities obtained from μXRF proved to be an effective way to analyse mudstone successions from epicontinental basins in order to: 1) characterise the sediments based on their depositional environment, including proximity to shoreline, weathering intensity, and redox conditions at the sediment-water interface, and 2) reconstruct marine transgressive-regressive cycles at several orders to develop high-resolution sequence-stratigraphic frameworks of fine-grained sediments.

The first phase of this research showed that the elemental intensity data collected from a μXRF core scanner had an exceptional level of reproducibility between multiple scans, with boxplot spreads and median values showing less than 5% variation in all elements with some major elements such as Fe, Ca, Ti, K, Si showing less than 1% variation between four separate scans. Since μXRF core scanning is a non-destructive analysis, this reproducibility means samples could be analysed multiple times and the total data averaged, thus increasing the signal-to-noise ratio. It could also be scanned with different parameters to obtain better detection of certain elements e.g., higher energy and exposure time to detect heavier elements.

This phase also showed that the μXRF data were well-correlated to the values obtained using the traditional ICP-OES/MS method, as well as to the mineralogy observed in petrographic thin sections. Spearman-Rho correlation coefficients showed moderate to strong values ($R^2 > 0.6$) for most major oxides (SiO_2, Al_2O_3, TiO_2, Fe_2O_3, and K_2O) and when the trends were compared using a simple confusion matrix, where the data are compared based on their position relative to their mean (higher or lower) and not their absolute values, they were even more similar. In terms of lithology and mineralogy, the μXRF were well-correlated to variations at lamina-scale and lower using the trends in Si and Ti to identify very-fine quartz sandstone and mudstone laminae, respectively, and that the sandstone laminae were also rich in Ca and Sr, indicating carbonate content which thin section analysis showed to be in the form of intergranular cement. This is an important characteristic of mudstone in the extraction of hydrocarbons as the strength of the rock will determine the geometry and extent of hydraulically-induced fractures. Sharp (i.e., nearly horizontal) transitions in the μXRF data were interpreted to represent rapid lithologic changes resulting from wave- or current-enhanced sediment gravity flows that are characterised by sharp-based, normally-graded laminae.

The main body of this research established detailed chemofacies and chemostratigraphic mapping of the Mancos Shale to gain a better insight into the depositional conditions and environments that control fine-grained sediments in an epicontinental seaway. The volume of elemental data obtained required the use of a hierarchical clustering algorithm, a Self-Organising Map, to group each observation (over 185,000 in total) according to its total elemental signature. The initial clustering is unsupervised, thereby eliminating researcher bias, but those clusters can subsequently be grouped into any number of 'superclusters' to address the specific goals of the study. Fewer superclusters, $k = 4$, grouped the sediments into their overall depositional environments such as the delta front, prodelta, and mudbelt and showed variability over several metres, likely corresponding to 3rd- and 4th-order depositional cycles (~1-3 Ma and 0.4-1 Ma, respectively) but increasing the number of superclusters showed variability over tens of centimetres or less, which would be the result of more localised environmental conditions (i.e., 5th order and higher; <0.1 Ma). The volume of data also allowed for the analysis of elemental variance within each environment, not just the average relationships between environments. For example, Fe had similar average values in the near-shore environments (fluvial, delta front, and prodelta) but significantly different standard deviations, which decreased along a basinward transect. Beyond the prodelta, Fe values decrease significantly through the mudbelt and into the shelf but the standard deviations decrease to the mid-mudbelt but then increase again into the shelf where the lower suspended-sediment concentration is more susceptible to reworking by bottom currents. This shows that the absolute values in elemental concentration obtained from low-resolution techniques (e.g., ICP-OES/MS, WD-XRF) may not be sufficient to accurately characterise fine-grained sediments according to their depositional environment.

The high-resolution chemostratigraphic mapping was very effective at reconstructing marine transgressive-regressive cycles at several orders based mainly on changes in the ratio of Fe/Ca and the total siliciclastic input, which was indicated by the sum of Ti, K, and Si. Regressive phases (i.e., shoreline progradation) were characterised by increasing values of Fe/Ca and siliciclastic input, which peaked at the transgressive flooding surface marking the transition the transgressive phase. Within each regressive phase, inferences could be made about the stacking patterns in terms of progradational-aggradational-retrogradational depending on the trend in the siliciclastic data. Progradational trends were defined by a shallower slope, indicating a more rapid increase of siliciclastic content through time while aggradational trends had steeper slopes indicating more consistent sediment compositions. The transgressive phase was consistently 3-10x shorter than the regressive phase of the same order and was defined by a rapid decline in siliciclastic values to a mimimum, which is where the maximum flooding surface was placed. At the highest order, these transgressive phases were remarkably similar in shape and extent but at lower orders, the transgressive phase was comprised of higher-order cycles as well. The highest-order cycle likely corresponds to the parasequences logged in near-shore environments and therefore is occurring over time scales of $\sim$20 ka meaning that the μXRF data are mapping the environmental changes occurring at sub-Milankovitch scales (i.e., decadal to centennial).

Future research should focus on using the techniques presented in this thesis to develop chemofacies and chemostratigraphy on other cores from within the San Juan Basin to demonstrate the ability to correlate cores across a basin. With several cores correlated, a high-resolution sequence-stratigraphic framework could be constructed for the San Juan Basin, or any basin, that shows eurybatic sea-level changes, which could then be compared with the frameworks constructed in other basins. This would provide the ability to determine the extent of the sea-level changes and whether they represent localised variations or a higher-frequency global signal. With more accurate age control, future research could also perform Fourier transforms or wavelet decompositions to determine exactly what frequencies are present in the data and what time scales they are operating on. This would provide invaluable information regarding climatic cycles in a greenhouse climate, which could be used to determine both high-frequency global fluctuations operating at sub-Milankovitch scales, as well as more localised fluctuations due to topography, tectonics, and climate circulation patterns.

Bibliography

Abdi, H. and Williams, L. J. (2010). Principal component analysis. Wiley Interdisciplinary Reviews: Computational Statistics, 2:433–459.

Ahmed, S., Bhattacharya, J. P., Garza, D. E., and Li, Y. (2014). Facies Architecture and Stratigraphic Evolution of A River-Dominated Delta Front, Turonian Ferron Sandstone, Utah, U.S.A. Journal of Sedimentary Research, 84:97–121.

Akyuz, I., Warny, S., Famubode, O., and Bhattacharya, J. P. (2016). Palynology of the Upper Cretaceous (Turonian) Ferron Sandstone Member, Utah, USA: Identification of marine flooding surfaces and Milankovitch cycles in subtropical, ever-wet, paralic to non-marine palaeoenvironments. Palynology, 40(1):122–136.

Al Ibrahim, M. A., Sarg, R., Hurley, N. F., Cantrell, D. L., and Humphrey, J. D. (2015). Depositional Environments and Sequence Stratigraphy of Carbonate Mudrocks using Sedimentology, Multi-Scale Electrofacies Visualization, and Geochemical Analyses: Tuwaiq Mountain and Hanifa Formations, Saudi Arabia. In AAPG Annual Convention and Exhibition.

Al Maliki, A., Al-lami, A. K., Hussain, H. M., and Al-Ansari, N. (2017). Comparison between inductively coupled plasma and X-ray fluorescence performance for Pb analysis in environmental soil samples. Environmental Earth Sciences, 76(12):1–7.

Algeo, T. J., Lyons, T. W., Blakey, R. C., and Over, D. J. (2007). Hydrographic conditions of the Devono-Carboniferous North American Seaway inferred from sedimentary Mo-TOC relationships. Palaeogeography, Palaeoclimatology, Palaeoecology, 256:204–230.

Algeo, T. J. and Rowe, H. (2012). Paleoceanographic applications of trace-metal concentration data. Chemical Geology, 324-325:6–18.

Algeo, T. J., Schwark, L., and Hower, J. C. (2004). High-resolution geochemistry and sequence stratigraphy of the Hushpuckney Shale (Swope Formation, eastern Kansas): Implications for climato-environmental dynamics of the Late Pennsylvanian Midcontinent Seaway. Chemical Geology, 206:259–288.

Arenas-Islas, D., Huerta-Diaz, M. A., Norzagaray-López, C. O., Mejia-Piña, K. G., Valdivieso-Ojeda, J. A., Otero, X. L., and Arcega-Cabrera, F. (2019). Calibration of portable X-ray fluorescence equipment for the geochemical analysis of carbonate matrices. Sedimentary Geology, 391:105517.

Armstrong, R. L. (1968). Sevier Orogenic Belt in Nevada and Utah. Geological Society of America Bulletin, 79:429–458.

Baioumy, H. and Lehmann, B. (2017). Anomalous enrichment of redox-sensitive trace elements in the marine black shales from the Duwi Formation, Egypt: Evidence for the late Cretaceous Tethys anoxia. Journal of African Earth Sciences, 133:7–14.

Baumgardner, R. W. and Rowe, H. (2017). PS Using Hierarchical Cluster Analysis to Improve Facies Definitions in Permian Mudrocks (Wolfcamp and Lower Leonard), Midland Basin, Texas. Geochemistry, 23:2198–2213.

Beil, S., Kuhnt, W., Holbourn, A. E., Aquit, M., Flögel, S., Chellai, E. H., and Jabour,

H. (2018). New insights into Cenomanian paleoceanography and climate evolution from the Tarfaya Basin, southern Morocco. Cretaceous Research, 84:451–473.

Ben-Awuah, J., Padmanabhan, E., and Sokkalingam, R. (2017). Geochemistry of Miocene sedimentary rocks from offshore West Baram Delta, Sarawak Basin, Malaysia, South China Sea: implications for weathering, provenance, tectonic setting, paleoclimate and paleoenvironment of deposition. Geosciences Journal, 21:167–185.

Bhattacharya, J. (2010). Deltas. In James, N. and Dalrymple, R., editors, Facies Models 4, pages 233–264. Canadian Sedimentology Research Group, St. John's, Newfoundland.

Bhattacharya, J. J. P., Miall, A. D., Ferron, C., Gabriel, J., Randazzo, N., Kynaston, D., Jicha, B. B. R., and Singer, B. B. S. (2019). Time-stratigraphy in point sourced river deltas: Application to sediment budgets, shelf construction, and paleo-storm records. Earth-Science Reviews, 199:102985.

Bhattacharya, J. P. (2006). Deltas. Number SEPM Special Publication No. 84.

Bhattacharya, J. P. (2011). Practical problems in the application of the sequence stratigraphic method and key surfaces: Integrating observations from ancient fluvial-deltaic wedges with Quaternary and modelling studies. Sedimentology, 58(1):120–169.

Bhattacharya, J. P., Howell, C. D., Maceachern, J. A., and Walsh, J. P. (2020). Bioturbation , sedimentation rates , and preservation of flood events in deltas. Palaeogeography, Palaeoclimatology, Palaeoecology, 560(May).

Bhattacharya, J. P. and MacEachern, J. A. (2009). Hyperpycnal rivers and prodeltaic shelves in the cretaceous seaway of North America. Journal of Sedimentary Research, 79(4):184–209.

Bhattacharya, J. P. and Tye, R. S. (2004). Searching for Modern Ferron Analogs and Application to Subsurface Interpretation. In Chidsley Jr, T. C., Adams, R. D., and Morris, T. H., editors, Regional to Wellbore Analog for Fluvial–Deltaic Reservoir Modeling: The Ferron Sandstone of Utah, number AAPG Studies in Geology 50, chapter 2, pages 39–57. American Association of Petroleum Geologists.

Bilodeau, W. L. (1986). The Mesozoic Mogollon Highlands, Arizona: an Early Cretaceous rift shoulder (USA). Journal of Geology, 94(5):724–735.

Birgenheier, L. P., Horton, B., McCauley, A. D., Johnson, C. L., and Kennedy, A. (2017). A depositional model for offshore deposits of the lower Blue Gate Member, Mancos Shale, Uinta Basin, Utah, USA. Sedimentology, 64:1402–1438.

Boggs Jr., S. and Boggs, S. (2009). Petrology of sedimentary rocks. Cambridge University Press.

Bornemann, A., Norris, R. D., Friedrich, O., Beckmann, B., Schouten, S., Damsté, J. S. S., Vogel, J., Hofmann, P., and Wagner, T. (2008). Isotopic Evidence for Glaciation During the Cretaceous Supergreenhouse. Science, 319(5860):189–192.

Boyle, J. F., Chiverrell, R. C., and Schillereff, D. (2015). Approaches to Water Content Correction and Calibration for µXRF Core Scanning: Comparing X-ray Scattering with Simple Regression of Elemental Concentrations. In Croudace, I. W. and Rothwell, R. G., editors, Micro-XRF Studies of Sediment Cores: Applications of a non-destructive tool for the environmental sciences, chapter 14, pages 373–390. Springer Science+Business Media, Dordrecht, developmen edition.

Broadhead, R. F. (2015). The Upper Mancos Shale in the San Juan Basin: three plays, conventional and unconventional. AAPG Search and Discovery, 10791:39.

Broadhead, R. F. (2021). The offshore Mancos play in the San Juan Basin as a component of the Mancos total petroleum system. AAPG Bulletin, 105(9):1765–1777.

Brown, E. T., Johnson, T. C., Scholz, C. A., Cohen, A. S., and King, J. W. (2007). Abrupt change in tropical African climate linked to the bipolar seesaw over the past 55,000 years. Geophysical Research Letters, 34(20):1–5.

Campbell, C. V. (1971). Depositional Model–upper Cretaceous Gallup Beach Shoreline, Ship Rock Area, Northwestern New Mexico. SEPM Journal of Sedimentary Research, 41(2):395–409.

Catuneanu, O. (2019). Scale in sequence stratigraphy. Marine and Petroleum Geology, 106(February):128–159.

Cerdà-Domènech, M., Frigola, J., Sanchez-Vidal, A., and Canals, M. (2020). Calibrating high resolution XRF core scanner data to obtain absolute metal concentrations in highly polluted marine deposits after two case studies off Portmán Bay and Barcelona, Spain. Science of the Total Environment, 717:134778.

Chen, H. F., Yeh, P. Y., Song, S. R., Hsu, S. C., Yang, T. N., Wang, Y., Chi, Z., Lee, T. Q., Chen, M. T., Cheng, C. L., Zou, J., and Chang, Y. P. (2013). The Ti/Al molar ratio as a new proxy for tracing sediment transportation processes and its application in aeolian events and sea level change in East Asia. Journal of Asian Earth Sciences, 73:31–38.

Cole, D. B., Zhang, S., and Planavsky, N. J. (2017). A new estimate of detrital redox-sensitive metal concentrations and variability in fluxes to marine sediments. Geochimica et Cosmochimica Acta, 215:337–353.

Corbin, J. C., Person, A., Iatzoura, A., Ferré, B., and Renard, M. (2000). Manganese in Pelagic carbonates: Indication of major Tectonic events during the geodynamic evolution of a passive continental margin (the Jurassic European Margin of the Tethys-Ligurian Sea). Palaeogeography, Palaeoclimatology, Palaeoecology, 156(1-2):123–138.

Craigie, N. (2018). Principles of Elemental Chemostratigraphy: A Practical User Guide. Springer International Publishing AG.

Croudace, I. W., Rindby, A., and Rothwell, R. G. (2006). ITRAX: Description and evaluation of a new multi-function X-ray core scanner. Geological Society Special Publication, 267(May 2016):51–63.

Croudace, I. W. and Rothwell, R. G., editors (2015). Micro-XRF Studies of Sediment Cores: Applications of a non-destructive tool for the environmental Springer Science+Business Media.

De Rafélis, M., Emmanuel, L., Renard, M., Atrops, F., and Du Chene, R. J. (2001). Geochemical characterization (Mn content) of third order eustatic sequences in Upper Jurassic pelagic carbonates of the Vocontian Trough (SE France). Eclogae Geologicae Helvetiae, 94(2):145–152.

Decelles, P. G. (1994). Late Cretaceous-Paleocene synorogenic sedimentation and kinematic history of the Sevier thrust belt, northeast Utah and southwest Wyoming. Geological Society of America Bulletin, 106(1):32–56.

Dypvik, H. and Harris, N. B. (2001). Geochemical facies analysis of fine-grained siliciclastics using Th/U, Zr/Rb and (Zr + Rb)/Sr ratios. Chemical Geology, 181:131–146.

El-Attar, A. and Pranter, M. J. (2016). Regional stratigraphy, elemental chemostratigraphy, and organic richness of the NiobraraMember of the Mancos Shale, Piceance Basin, Colorado. AAPG Bulletin, 100(3):345–377.

Eldrett, J. S., Ma, C., Bergman, S. C., Lutz, B., Gregory, F. J., Dodsworth, P., Phipps, M., Hardas, P., Minisini, D., Ozkan, A., Ramezani, J., Bowring, S. A., Kamo, S. L., Ferguson, K., Macaulay, C., and Kelly, A. E. (2015). An astronomically calibrated stratigraphy of the Cenomanian, Turonian and earliest Coniacian from the Cretaceous Western Interior Seaway, USA: Implications for global chronostratigraphy. Cretaceous Research, 56:316–344.

Ernst, T., Berman, T., Buscaglia, J., Eckert-Lumsdon, T., Hanlon, C., Olsson, K., Palenik, C., Ryland, S., Trejos, T., Valadez, M., and Almirall, J. R. (2014). Signal-to-noise ratios in forensic glass analysis by micro X-ray fluorescence spectrometry. X-Ray Spectrometry, 43(1):13–21.

Ferron, C. (2019). Detrital Zircon Signal Inversion in the Cretaceous Southwestern U.S. Interior Seawa Msc, McMaster University.

Fielding, C. R. (2010). Planform and facies variability in asymmetric deltas: Facies analysis and depositional architecture of the turonian Ferron Sandstone in the western Henry Mountains, south-central Utah, U.S.A. Journal of Sedimentary Research, 80(5-6):455–479.

Friedrich, O., Norris, R. D., and Erbacher, J. (2012). Evolution of middle to late Cretaceous oceans-A 55 m.y. Record of Earth's temperature and carbon cycle. Geology, 40(2):107–110.

Gabriel, J. J., Reinhardt, E. G., Chang, X., and Bhattacharya, J. P. (2022a). Application of μXRF analysis on the Upper Cretaceous Mancos Shale: A comparison with ICP-OES/MS. Marine and Petroleum Geology, 140:105662.

Gabriel, J. J., Reinhardt, E. G., Turkistani, M. N., Genovese, C., Bhattacharya, J. P., and Kynaston, D. (2022b). Defining chemostratigraphic flooding surfaces in Upper Mancos Shale using high-resolution chemofacies. Sedimentology.

Gregory, B. R., Patterson, R. T., Reinhardt, E. G., Galloway, J. M., and Roe, H. M. (2019). An evaluation of methodologies for calibrating Itrax X-ray fluorescence counts with ICP-MS concentration data for discrete sediment samples. Chemical Geology, 521(February):12–27.

Gregory, B. R., Reinhardt, E. G., Macumber, A. L., Nasser, N. A., Patterson, R. T., Kovacs, S. E., and Galloway, J. M. (2017). Sequential sample reservoirs for Itrax-XRF analysis of discrete samples. Journal of Paleolimnology, 57(3):287–293.

Grigg, J. J. (2016). Macroscopic and Microscopic Controls on Mechanical Properties of Mudstones. Msc, New Mexico Institute of Mining and Technology.

Haq, B. U. (2014). Cretaceous eustasy revisited. Global and Planetary Change, 113:44–58.

Haq, B. U. and Huber, B. T. (2017). Anatomy of a eustatic event during the Turonian (Late Cretaceous) hot greenhouse climate. Science China Earth Sciences, 60(1):20–29.

Hart, B. S. (2016). Marine mudstone source rocks in epicontinental basins: Development of a conceptual facies model and application to Cenomanian/Turonian mudstones of the Cretaceous Western Interior Seaway. Hydrocarbon Source Rocks in Unconventional Plays, Rocky Mountain Region: Rocky Mountain Association of Geologists, Special Publication, pages 364–421.

Haug, G. H., Günther, D., Peterson, L. C., Sigman, D. M., Hughen, K. A., and Aeschlimann, B. (2003). Climate and the Collapse of Maya Civilization. Science, 299(1):1731–1735.

Hawkins, S. J., Charpentier, R. R., Schenk, C. J., Leathers-Miller, H. M., Klett, T. R., Brownfield, M. E., Finn, T. M., Gaswirth, S. B., Marra, K. R., Le, P. A., Mercier,

T. J., Pitman, J. K., and Tennyson, M. E. (2016). Assessment of Continuous (Unconventional) Oil and Gas Resources in the Late Cretaceous Mancos Shale of the Piceance Basin, Uinta-Piceance Province, Colorado and Utah, 2016. Technical Report June, USGS.

Hay, W. W., DeConto, R. M., de Boer, P., Flögel, S., Song, Y., and Stepashko, A. (2019). Possible solutions to several enigmas of Cretaceous climate, volume 108. Springer Berlin Heidelberg.

Hsiung, K. H., Kanamatsu, T., Ikehara, K., Usami, K., Horng, C. S., Ohkouchi, N., Ogawa, N. O., Saito, S., and Murayama, M. (2021). X-ray fluorescence core scanning, magnetic signatures, and organic geochemistry analyses of Ryukyu Trench sediments: turbidites and hemipelagites. Progress in Earth and Planetary Science, 8(1).

Hu, Y. G. and Plint, A. G. (2009). An allostratigraphic correlation of a mudstone-dominated, syn-tectonic wedge: the Puskwaskau Formation (Santonian-Campanian) in outcrop and subsurface, Western Canada Foreland Basin. Bulletin of Canadian Petroleum Geology, 57(1):1–33.

Hubert, J. F., Butera, J. G., and Rice, R. F. (1972). Sedimentology of Upper Cretaceous Cody-Parkman Delta, Southwestern Powder River Basin, Wyoming. Geological Society of America Bulletin, 83:1649–1670.

Jarvis, I., Murphy, A. M., and Gale, A. S. (2001). Geochemistry of pelagic and hemipelagic sediments: criteria for identifying systems tracts and sea-level change. Journal of the Geological Society, 158:685–696.

Joo, Y. J. and Sageman, B. B. (2014). Cenomanian to campanian carbon isotope chemostratigraphy from the Western Interior Basin, U.S.A. Journal of Sedimentary Research, 84(7):529–542.

Kelloway, S. J., Ward, C. R., Marjo, C. E., Wainwright, I. E., and Cohen, D. R. (2014). Quantitative chemical profiling of coal using core-scanning X-ray fluorescence techniques. International Journal of Coal Geology, 128-129:55–67.

Kohonen, T. (2013). Essentials of the self-organizing map. Neural Networks, 37:52–65.

Krapez, B. (1996). Sequence stratigraphic concepts applied to the identification of basin-filling rhythms in Precambrian successions. Australian Journal of Earth Sciences, 43(4):355–380.

LaGrange, M. T., Konhauser, K. O., Catuneanu, O., Harris, B. S., Playter, T. L., and Gingras, M. K. (2020). Sequence stratigraphy in organic-rich marine mudstone successions using chemostratigraphic datasets. Earth-Science Reviews, 203(July 2019).

Lash, G. G. and Blood, D. R. (2014). Organic matter accumulation, redox, and diagenetic history of the Marcellus Formation, southwestern Pennsylvania, Appalachian basin. Marine and Petroleum Geology, 57:244–263.

Lazar, O. R., Bohacs, K. M., Macquaker, J. H. S., Schieber, J., and Demko, T. M. (2015). Capturing Key Attributes of Fine-Grained Sedimentary Rocks In Outcrops, Cores, and Thin Sections: Nomenclature and Description Guidelines. Journal of Sedimentary Research, 85:230–246.

Leclezio, L., Jansen, A., Whittemore, V. H., and De Vries, P. J. (2015). Pilot validation of the tuberous sclerosis-associated neuropsychiatric disorders (TAND) checklist. Pediatric Neurology, 52(1):16–24.

Li, M., Huang, C., Ogg, J., Zhang, Y., Hinnov, L., Wu, H., Chen, Z. Q., and Zou, Z. (2019). Paleoclimate proxies for cyclostratigraphy: Comparative analysis using a Lower Triassic marine section in South China. Earth-Science Reviews, 189(January):125–146.

Li, W., Bhattacharya, J. P., and Campbell, C. (2010). Temporal Evolution of Fluvial Style in a Compound Incised-Valley Fill, Ferron "Notom Delta", Henry Mountains Region, Utah (U.S.A.). Journal of Sedimentary Research, 80:529–549.

Li, Y. and Bhattacharya, J. P. (2013). Facies-Architecture Study of A Stepped, Forced Regressvie Compound Incised Valley In the Ferron Notom Delta, Southern Central Utah, U.S.A. Journal of Sedimentary Research, 83:206–225.

Li, Z. and Schieber, J. (2018). Detailed facies analysis of the Upper Cretaceous Tununk Shale Member, Henry Mountains Region, Utah: Implications for mudstone depositional models in epicontinental seas. Sedimentary Geology, 364:141–159.

Lin, W., Bhattacharya, J. P., and Stockford, A. (2019). High-resolution Sequence Stratigraphy and Implications For Cretaceous Glacioeustasy of the Late Cretaceous Gallup System, New Mexico, U.S.A. Journal of Sedimentary Research, 89(6):552–575.

Lisitzin, A. P. (1996). Oceanic Sedimentation: Lithology and Geochemistry. American Geophysical Union, english ed edition.

Little, S. H., Vance, D., Lyons, T. W., and McManus, J. (2015). Controls on trace metal authigenic enrichment in reducing sediments: Insights from modern oxygen-deficient settings. American Journal of Science, 315(2):77–119.

Löwemark, L., Bloemsma, M., Croudace, I., Daly, J. S., Edwards, R. J., Francus, P., Galloway, J. M., Gregory, B. R., Huang, J.-J. S., Jones, A. F., Kylander, M., Luo, Y., Maclachlan, S., Ohlendorf, C., Patterson, R. T., Pearce, C., Profe, J., Reinhardt, E. G., Stranne, C., Tjallingii, R., Turner, J. N., Steven Huang, J. J., Jones, A. F., Kylander, M., Luo, Y., Maclachlan, S., Ohlendorf, C., Patterson, R. T., Pearce, C., Profe, J., Reinhardt, E. G., Stranne, C., Tjallingii, R., and Turner, J. N. (2019).

Practical guidelines and recent advances in the Itrax XRF core-scanning procedure. Quaternary International, 514(February 2018):16–29.

Lowery, C. M., Leckie, R. M., Bryant, R., Elderbak, K., Parker, A., Polyak, D. E., Schmidt, M., Snoeyenbos-West, O., and Sterzinar, E. (2018). The Late Cretaceous Western Interior Seaway as a model for oxygenation change in epicontinental restricted basins. Earth-Science Reviews, 177(November 2017):545–564.

Ma, C. and Li, M. (2020). Astronomical time scale of the Turonian constrained by multiple paleoclimate proxies. Geoscience Frontiers, 11(4):1345–1352.

Ma, C., Meyers, S. R., Sageman, B. B., Singer, B. S., and Jicha, B. R. (2014). Testing the astronomical time scale for oceanic anoxic event 2, and its extension into Cenomanian strata of the Western Interior Basin (USA). Bulletin of the Geological Society of America, 126(7-8):974–989.

MacEachern, J. A. and Bann, K. L. (2020). The Phycosiphon ichnofacies and the Rosselia ichnofacies: Two new ichnofacies for marine deltaic environments. Journal of Sedimentary Research, 90(8):855–886.

MacEachern, J. A., Pemberton, S. G., Gingras, M. K., and Bann, K. L. (2010). Ichnology and Facies Models. In James, N. P. and Dalrymple, R. W., editors, Facies Models 4, chapter 3, pages 19–58. Geological Association of Canada.

Macquaker, J. H. S., Bentley, S. J., and Bohacs, K. M. (2010). Wave-enhanced sediment-gravity flows and mud dispersal across continental shelves: Reappraising sediment transport processes operating in ancient mudstone successions. Geology, 38(10):947–950.

McDonough, K. J. and Cross, T. A. (1991). Late Cretaceous Sea Level From a Paleoshoreline. Journal of Geophysical Research, 96(B4):6591–6607.

McLennan, S. M. (2001). Relationships between the trace element composition of sedimentary rocks and upper continental crust. Geochemistry, Geophysics, Geosystems, 2(4).

Miall, A. D., Catuneanu, O., Vakarelov, B. K., and Post, R. (2008). The Western Interior Basin. In Miall, A. D., editor, The Sedimentary Basins of the United States and Canada, chapter Chapter 9, pages 330–362. Elsevier.

Miller, K. G., Sugarman, P. J., Browning, J. V., Kominz, M. A., Hernández, J. C., Olsson, R. K., Wright, J. D., Feigenson, M. D., and Van Sickel, W. (2003). Late Cretaceous chronology of large, rapid sea-level changes: Glacioeustasy during the greenhouse world. Geology, 31(7):585–588.

Molenaar, C. M. and Cobban, W. A. (1991). Middle Cretaceous stratigraphy on the south and east sides of the Uinta Basin, northeastern Utah and northwestern Colorado. Technical report, U.S. Geological Survey.

Molenaar, C. M., Cobban, W. A., Merewether, E. A., Pillmore, C. L., Wolfe, D. G., and Holbrook, J. M. (2001). Section D-D', east-central Arizona to Pagosa Springs, Colorado. In Regional stratigraphic cross sections of Cretaceous rocks from east-central Arizona to the Oklahoma panhandle. Citeseer.

Mulder, T., Syvitski, J. P., Migeon, S., Faugères, J. C., and Savoye, B. (2003). Marine hyperpycnal flows: Initiation, behaviorand related deposits. A review. Marine and Petroleum Geology, 20(6-8):861–882.

North, C. P., Hole, M. J., and Jones, D. G. (2005). Geochemical correlation in deltaic successions: A reality check. Bulletin of the Geological Society of America, 117(5-6):620–632.

Nummedal, D. and Molenaar, C. M. (1995). Sequence stratigraphy of ramp-setting strand plain successions: the Gallup Sandstone, New Mexico. In van Wagoner, J. C. and Bertram, G. T., editors, Sequence Stratigraphy of Foreland Basin Deposits: AAPG Memoir 64, chapter 9, pages 277–310. American Association of Petroleum Geologists.

Olde, K., Jarvis, I., Uličný, D., Pearce, M. A., Trabucho-Alexandre, J., Stanislav, Č., Gröcke, D. R., Laurin, J., Švábenická, L., and Tocher, B. A. (2015). Geochemical and palynological sea-level proxies in hemipelagic sediments : A critical assessment from the Upper Cretaceous of the Czech Republic. Palaeogeography, Palaeoclimatology, Palaeoecology, 435:222–243.

Pearce, T. J., Besly, B. M., Wray, D. S., and Wright, D. K. (1999). Chemostratigraphy: a method to improve interwell correlation in barren sequences – a case study using onshore Duckmantian/Stephanian sequences (West Midlands, U.K.). Sedimentary Geology, 124:197–220.

Peti, L., Augustinus, P. C., Gadd, P. S., and Davies, S. J. (2019). Towards characterising rhyolitic tephra layers from New Zealand with rapid, non-destructive μ-XRF core scanning. Quaternary International, 514(June 2018):161–172.

Petty, D. (2022). Shallow-Water versus Deep-Water: Stratigraphic Geometries in the Organic-Rich Shale/Mudstone Debate. GSA Today, 32(7):4–10.

Pietras, J. T. and Spiegel, E. B. (2018). Xrf-based Chemostratigraphy Between and Across Two Disconformities in the Ordovician Trenton Group and Utica Shale of Central New York, U.s.a. Journal of Sedimentary Research, 88(3):365–384.

Plint, A. G. (2014). Mud dispersal across a Cretaceous prodelta: Storm-generated, wave-enhanced sediment gravity flows inferred from mudstone microtexture and microfacies. Sedimentology, 61(3):609–647.

Plint, A. G., Macquaker, J. H. S., and Varban, B. L. (2012). Bedload Transport of Mud Across A Wide, Storm-Influenced Ramp: Cenomanian-Turonian Kaskapau Formation, Western Canada Foreland Basin. Journal of Sedimentary Research, 82(11):801–822.

Profe, J., Wacha, L., Frechen, M., Ohlendorf, C., and Zolitschka, B. (2018). XRF scanning of discrete samples – A chemostratigraphic approach exemplified for loess-paleosol sequences from the Island of Susak, Croatia. Quaternary International, 494(April):34–51.

R Core Team (2021). R: A Language and Environment for Statistical Computing. R Foundation for Statistical Computing, Vienna, Austria.

Ridgley, J. L., Condon, S. M., and Hatch, J. R. (2013). Geology and Oil and Gas Assessment of the Mancos-Menefee Composite Total Petroleum System, San Juan Basin, New Mexico and Colorado. In Total Petroleum systems and geologic assessment of undiscovered oil and gas resources in the San Juan Basin Province, exclusive of Paleozoic rocks, New Mexico and Colorado, number USGS DDS-69-F, chapter 4, page 97.

Rothwell, R. G., editor (2006). New Techniques in Sediment Core Analysis. Geological Society of London.

Rothwell, R. G. and Croudace, I. W. (2015a). Micro-XRF Studies of Sediment Cores: A perspective on Capability and Application in the Environmental Sciences. In Croudace, I. W. and Rothwell, R. G., editors, Micro-XRF Studies of Sediment Cores:

Applications of a non-destructive tool for the environmental sciences, chapter 1, pages 1–22. Springer Science+Business Media, developmen edition.

Rothwell, R. G. and Croudace, I. W. (2015b). Twenty Years of XRF Core Scanning Marine Sediments: What Do Geochemical Proxies Tell Us? In Croudace, I. W. and Rothwell, R. G., editors, Micro-XRF Studies of Sediment Cores: Applications of a non-destructive tool for the environmental sciences, chapter 2, pages 25–102. Springer Science+Business Media, Dordrecht, developmen edition.

Rothwell, R. G., Hoogakker, B., Thomson, J., Croudace, I. W., and Frenz, M. (2006). Turbidite emplacement on the southern Balearic Abyssal Plain (western Mediterranean Sea) during Maine Isotope Stages 1-3: an application of ITRAX XRF scanning of sediment cores to lithostratigraphic analysis. In Rothwell, R., editor, New Techniques in Sediment Core Analysis, pages 79–98. Geological Society of London.

Rothwell, R. G. and Rack, F. R. (2006). New techniques in sediment core analysis: an introduction. In Rothwell, R., editor, New Techniques in Sediment Core Analysis, volume Special Pu, chapter 1, pages 1–29. Geological Society of London.

Rowe, H., Hughes, N., and Robinson, K. (2012). The quantification and application of handheld energy-dispersive x-ray fluorescence (ED-XRF) in mudrock chemostratigraphy and geochemistry. Chemical Geology, 324-325:122–131.

Sageman, B. B., Rich, J., Arthur, M. A., Birchfield, G. E., and Dean, W. E. (1997). Evidence for Milankovitch Periodicities in Cenomanian-Turonian Lithologic and Geochemical Cycles, Western Interior U.S.A. Journal of Sedimentary Research, 67(2):286–302.

Schieber, J. (2016). Mud re-distribution in epicontinental basins - Exploring likely processes. Marine and Petroleum Geology, 71:119–133.

Schieber, J., Southard, J., and Thaisen, K. (2007). Accretion of Mudstone Beds from Migrating Floccule Ripples. Science, 318:1760–1763.

Schieber, J., Southard, J. B., Kissling, P., Rossman, B., and Ginsburg, R. (2013). Experimental Deposition of Carbonate Mud From Moving Suspensions: Importance of Flocculation and Implications For Modern and Ancient Carbonate Mud Deposition. Journal of Sedimentary Research, 83(11):1025–1031.

Scroxton, N., Burns, S., Dawson, P., Rhodes, J. M., Brent, K., McGee, D., Heijnis, H., Gadd, P., Hantoro, W., and Gagan, M. (2018). Rapid measurement of strontium in speleothems using core-scanning micro X-ray fluorescence. Chemical Geology, 487:12–22.

Selala, M. S., Senzanje, A., and Dhavu, K. (2019). Requirements for sustainable operation and maintenance of rural small-scale water infrastructure in Limpopo Province, South Africa. Water SA, 45(2):291–304.

Sharma, S., Bhattacharya, J. P., and Richards, B. (2017). Source-to-sink sediment budget analysis of the Cretaceous Ferron Sandstone, Utah, U.S.A, using the fulcrum approach. Journal of Sedimentary Research, 87(6):594–608.

Sixsmith, P. J., Hampson, G. J., Gupta, S., Johnson, H. D., and Fofana, J. F. (2008). Facies architecture of a net transgressive sandstone reservoir analog: The Cretaceous Hosta Tongue volume 92.

Slingerland, R., Kump, L. R., Arthur, M. A., Fawcett, P. J., Sageman, B. B., and Barron, E. J. (1996). Estuarine circulation in the Turonian Western interior seaway of North America. Geological Society of America Bulletin, 108(7):941–952.

Sloss, L. L. (1963). Sequences in the cratonic interior of north America. Geological Society of America Bulletin, 74:93–114.

Sloss, L. L. (1988). Forty years of sequence stratigraphy. Geological Society of America Bulletin, 100:1661–1665.

Taylor, K. G. and Macquaker, J. . H. S. (2014). Diagenetic alterations in a silt- and clay-rich mudstone succession: an example from the Upper Cretaceous Mancos Shale of Utah, USA. Clay Minerals, 49(2):213–227.

Templ, M., Filzmoser, P., and Reimann, C. (2008). Cluster analysis applied to regional geochemical data: Problems and possibilities. Applied Geochemistry, 23(8):2198–2213.

Thomson, J., Croudace, I. W., and Rothwell, R. G. (2006). A geochemical application of the ITRAX scanner to a sediment core containing eastern Mediterranean sapropel units. In Geological Society Special Publication, volume 267, pages 65–77. Geological Society of London.

Tjallingii, R., Röhl, U., Kölling, M., and Bickert, T. (2007). Influence of the water content on X-ray fluorescence corescanning measurements in soft marine sediments. Geochemistry, Geophysics, Geosystems, 8(2):1–12.

Tribovillard, N., Algeo, T. J., Lyons, T., and Riboulleau, A. (2006). Trace metals as paleoredox and paleoproductivity proxies: An update. Chemical Geology, 232(1-2):12–32.

Turkistani, M. N., Reinhardt, E. G., Kynaston, D., and Bhattacharya, J. P. (2022). Foraminifera and thecamoebians morphogroup analysis of the Upper Cretaceous (Turonian) Ferron-Notom Delta, Central Utah, USA. Journal of Foraminiferal Research, 601(September 2021):111146.

Turner, B. W., Tréanton, J. A., and Slatt, R. M. (2016). The use of chemostratigraphy to refine ambiguous sequence stratigraphic correlations in marine mudrocks. An example from the Woodford Shale, Oklahoma, USA. Journal of the Geological Society, 173(5):854–868.

Vail, P. R., Mitchum Jr, R., and Thompson III, S. (1977). Seismic stratigraphy and global changes of sea level: Part 3. Relative changes of sea level from Coastal Onlap: section 2. Application of seismic reflection Configuration to Stratigraphic Interpretation. AAPG Special Volumes.

van Wagoner, J. C., Mitchum, R. M., Campion, K. M., and Rahmanian, V. D. (1990). Siliciclastic Sequence Stratigraphy in Well Logs, Cores, and Outcrops: Concepts for High-Resolution Correlation of Time and Facies. AAPG Methods in Exploration Series 7, (7).

Vialaneix, N., Maigne, E., Mariette, J., Olteanu, M., Rossi, F., Bendhaiba, L., and Bolaert, J. (2020). SOMbrero: SOM Bound to Realize Euclidean and Relational Outputs. R package version 1.3-1.

Walsh, J. P. and Nittrouer, C. A. (2009). Understanding fine-grained river-sediment dispersal on continental margins. Marine Geology, 263(1-4):34–45.

Wang, M. J., Zheng, H. B., Xie, X., Fan, D. D., Yang, S. Y., Zhao, Q. H., and Wang, K. (2011). A 600-year flood history in the Yangtze River drainage: Comparison between a subaqueous delta and historical records. Chinese Science Bulletin, 56(2):188–195.

Ward, C. R., Kelloway, S. J., French, D., Wainwright, I. E., Marjo, C., and Cohen, D. R. (2018). Profiling of inorganic elements in coal seams using laboratory-based core scanning X-ray fluorescence techniques. International Journal of Coal Geology, 191:158–171.

Weltje, G. J., Bloemsma, M. R., Tjallingii, R., Heslop, D., Röhl, U., and Croudace, I. W. (2015). Prediction of Geochemical Composition from XRF Core Scanner Data:

A New Multivariate Approach Including Automatic Selection of Calibration Samples and Quantification of Uncertainties. In Croudace, I. W. and Rothwell, R. G., editors, Micro-XRF Studies of Sediment Cores: Applications of a non-destructive tool for the environmental sciences, chapter 21, pages 507–534. Springer Science+Business Media.

Weltje, G. J. and Tjallingii, R. (2008). Calibration of XRF core scanners for quantitative geochemical logging of sediment cores: Theory and application. Earth and Planetary Science Letters, 274(3-4):423–438.

Wheeler, H. E. and Mallory, V. S. (1953). Designation of Stratigraphic Units. AAPG Bulletin, 37(10):2407–2421.

Wheeler, H. E. and Mallory, V. S. (1956). Factors in Lithostratigraphy. AAPG Bulletin, 40(11):2711–2723.

White, T., González, L., Ludvigson, G., and Poulsen, C. (2001). Middle Cretaceous greenhouse hydrologic cycle of North America. Geology, 29(4):363–366.

Wilson, R. D. and Schieber, J. (2014). Muddy Prodeltaic Hyperpycnites in the Lower Genesee Group of Central New York, USA: Implications For Mud Transport In Epicontinental Seas. Journal of Sedimentary Research, 84:866–874.

Wold, S., Esbensen, K., and Geladi, P. (1987). Principal Component Analysis. Chemometrics and Intelligent Laboratory Systems, 2:37–52.

Wu, C., Bhattacharya, J. P., and Ullah, M. S. (2015). Paleohydrology and 3D Facies Architecture of Ancient Point Bars, Ferron Sandstone, Notom Delta, South-Central Utah, U.S.A. Journal of Sedimentary Research, 85(4):399–418.

Yoon, H., Ingraham, M. D., Grigg, J., Rosandick, B., Mozley, P., Rinehart, A., Mook, W. M., and Dewers, T. (2019). Impact of Depositional and Diagenetic Heterogeneity on Multiscale Mechanical Behavior of Mancos Shale, New Mexico and Utah, USA. In Camp, W., Milliken, K., Taylor, K., Fishman, N., Hackley, P., and Macquaker, J., editors, Mudstone diagenesis: Research perspectives for shale hydrocarbon reservoirs, seals, and source rocks: AAPG Memoir 120, chapter 8, pages 121–148. American Association of Petroleum Geologists.

Zarriess, M., Johnstone, H., Prange, M., Steph, S., Groeneveld, J., Mulitza, S., and MacKensen, A. (2011). Bipolar seesaw in the northeastern tropical Atlantic during Heinrich stadials. Geophysical Research Letters, 38(4):3–8.

Zarriess, M. and Mackensen, A. (2010). The tropical rainbelt and productivity changes off northwest Africa: A 31,000-year high-resolution record. Marine Micropaleontology, 76(3-4):76–91.

Zhu, Y., Bhattacharya, J. P., Li, W., Lapen, T. J., Jicha, B. R., and Singer, B. S. (2012). Milankovitch-Scale Sequence Stratigraphy and Stepped Forced Regressions of the Turonian Ferron Notom Deltaic Complex, South-Central Utah, U.S.A. Journal of Sedimentary Research, 82:723–746.